UNIVERSIDADE
BEIRA INTERIOR

Piezoresistive Sensing for Structural Health Monitoring of Multifunctional MWCNT-Reinforced Composites under Low-Velocity Impacts

(versão final após defesa)

Sérgio Daniel Fernandes Brito

Dissertação para obtenção do Grau de Mestre em
Engenharia Aeronáutica
(Mestrado Integrado)

Orientador: Prof. Doutor João Pedro Nunes Pereira
Co-orientador: Prof. Doutor Abílio Manuel Pereira da Silva
Co-orientador: Mestre João Miguel Nunes Parente

Covilhã, março de 2024

Declaração de Integridade

Eu, Sérgio Daniel Fernandes Brito, que abaixo assino, estudante com o número de inscrição 41731 do Mestrado Integrado em Engenharia Aeronáutica da Faculdade de Engenharia, declaro ter desenvolvido o presente trabalho e elaborado o presente texto em total consonância com o **Código de Integridades da Universidade da Beira Interior**.

Mais concretamente afirmo não ter incorrido em qualquer das variedades de Fraude Académica, e que aqui declaro conhecer, que em particular atendi à exigida referenciação de frases, extratos, imagens e outras formas de trabalho intelectual, e assumindo assim na íntegra as responsabilidades da autoria.

Universidade da Beira Interior, Covilhã 06/03/2024

Dedication

To my grandparents
António da Costa Fernandes and Domingos Ferreira de Brito

May their love, protection, and kindness continue to light the path through the journeys of my life.
Thank you. You will always be in my heart.

Acknowledgements

First and foremost, I would like to express my gratitude to my supervisor, Prof. João Nunes Pereira, without whom I could not have undertaken this journey, for his tireless support, availability, intellectual solidarity, and unwavering guidance. More than a mentor, he was a friend, always happy to share good moments of fun, laughter, and random conversation that helped make this endeavor a little easier every day. My deepest thank you for teaching me so much and being a source of motivation and encouragement to carry the work through to the end.

This endeavor would also not have been possible without Prof. Abílio Silva. His passion for materials science has driven my curiosity in this research field, inspiring me to pursue this work. My deepest gratitude for the guidance, mentorship, and mainly for the enthusiasm shown during the project, always willing to give precious points of view and discuss new ideas for improvement.

I would also like to convey my sincere gratitude to João Parente and Prof. Paulo Santos for their support, availability, knowledge, and expertise generously shared during this research. Their profound insights into the field of fiber-reinforced composites manufacturing and impact testing played a paramount role in the successful culmination of this project.

To the engineer Carlos Coelho, from the Polytechnic Institute of Tomar, for all the help and availability in carrying out the impact tests.

I want to express my heartfelt gratitude to the Center for Mechanical and Aerospace Science and Technologies (C–MAST) for their generous provision of laboratory resources, equipment, materials, and invaluable support throughout this endeavor.

To all of my closest friends, with whom I had the pleasure to share these past five years, I want to thank them for pushing forward with me in the ups and downs of this academic journey, and especially for all the unforgettable memories we have built together.

To my girlfriend, Luísa, who stood by my side in every moment. It would take more than a simple thanks to cover the infinite support, patience, and encouragement she has provided me all these years. I want to thank her for always believing in me and helping me become the best version of myself.

Lastly and most importantly, I want to thank my family. To my parents, Rosa and Sérgio, for the unconditional love, support, confidence, and sacrifices they made throughout all these years to provide me the possibility to achieve personal and professional success. They have been the pillars of my life, to whom I owe everything I am today. And to my brother, Marco, I am deeply grateful for being my lifelong companion and for all the joy he has brought into my life.

Resumo

Os materiais compósitos reforçados com fibras estabeleceram-se firmemente como a escolha de eleição para o projeto e fabrico de estruturas de alto desempenho, nomeadamente na engenharia aeronáutica e aeroespacial. Apesar das excelentes propriedades mecânicas destes materiais, a sua vulnerabilidade a danos em serviço, principalmente devido a impactos de baixa velocidade, desencadeou a necessidade de desenvolver sistemas de monitorização da saúde estrutural com capacidade de fornecer indicações precoces da ocorrência de danos, garantindo a segurança e longevidade das estruturas compósitas nas indústrias aeronáutica e aeroespacial. Neste contexto, o objetivo central deste trabalho é criar um compósito polimérico auto-sensível, reforçado com fibras de vidro, com capacidades de deteção em tempo real de danos causados por impactos de baixa velocidade. Para o efeito, 0.5 wt% de nanotubos de carbono de parede múltipla foram adicionados à matriz epóxi de modo a atuarem como sensores piezoresistivos. Inicialmente, foram analisadas as propriedades mecânicas dos compósitos antes e depois dos impactos com energias de 3 J e 6 J, revelando uma melhoria significativa no desempenho mecânico devido à incorporação dos nanotubos de carbono. Posteriormente, a análise incidiu na resposta ao impacto e a caraterização dos danos nos provetes, revelando diferenças consideráveis no grau de danos sofridos sob os dois níveis distintos de energia de impacto. Seguidamente, os provetes nano-reforçados foram submetidos a condições controladas de cargas de flexão, simulando esforços mecânicos reais. Os resultados obtidos a partir de testes de carregamento monotónico e cíclico demonstraram uma correlação notável entre a tensão mecânica e a correspondente alteração na resistência eléctrica (fator de variação de -0.40 para os provetes não impactados), realçando o comportamento piezoresistivo caraterístico do material. Finalmente, a resposta piezoresistiva dos provetes durante os impactos de 3 J e 6 J validou as suas capacidades de auto-sensorização na deteção em tempo real de impactos de baixa velocidade. Em suma, ao adicionar 0.5 wt% de nanotubos de carbono de parede múltipla à matriz epóxi, foi possível obter um material compósito de fibra de vidro que pode atuar simultaneamente como componente estrutural e sensor de deformação, oferecendo uma solução eficaz e multifuncional para aplicações de monitorização da saúde estrutural.

Palavras-chave

Monitorização da Saúde Estrutural, Sensorização Piezoresistiva, Impacto de Baixa Velocidade, Nanotubos de Carbono de Paredes Múltiplas, Compósito Polimérico Reforçado com Fibra de Vidro, Deformação à Flexão

Abstract

Fiber-reinforced composites have firmly established themselves as the preferred choice for designing and manufacturing high-performance structures, particularly in aeronautical and aerospace engineering. Despite the outstanding mechanical properties of these materials, their vulnerability to in-service damages, mainly due to low-velocity impacts, has driven the need for reliable structural health monitoring systems that can provide early indications of damage, ensuring the safety and longevity of composite structures in the aeronautical and aerospace industries. In this context, the core objective of this study is to develop a self-sensing glass fiber-reinforced composite with real-time damage detection capabilities tailored for low-velocity impact events. To achieve this, 0.5 wt% of multi-walled carbon nanotubes were added to the epoxy matrix to serve as piezoresistive sensors. Initially, the mechanical properties of the composites were assessed both before and after experiencing impacts of 3 J and 6 J energies, revealing a tangible enhancement in mechanical performance due to the incorporation of multi-walled carbon nanotubes. Subsequently, the investigation extended to the impact response and damage characterization of the specimens, uncovering notable distinctions in the degree of damage incurred under the two distinct impact energy levels. Afterward, the nano-enhanced specimens underwent controlled flexural loading conditions, simulating real-world mechanical stresses. The changes in electrical resistance of the specimens were monitored as a function of applied strain. The results obtained from monotonic and cyclic loading tests demonstrated a remarkable correlation between the mechanical strain and the corresponding change in electrical resistance (gauge factor of -0.40 for the non-impacted specimens), highlighting the inherent piezoresistive behavior of the material. Finally, the piezoresistive response of the specimens under 3 J and 6 J impact events validated its self-sensing capabilities for the real-time detection of low-velocity impacts. In summary, by adding 0.5 wt% of multi-walled carbon nanotubes to the epoxy matrix, it was possible to obtain a glass-fiber composite material that could act as a structural component and a strain sensor simultaneously, offering an effective and multifunctional solution for structural health monitoring applications.

Keywords

Structural Health Monitoring, Piezoresistive Sensing, Low-Velocity Impact, Multi-Walled Carbon Nanotubes, Glass Fiber Reinforced Polymer Composite, Flexural Strain

Contents

List of Figures

List of Tables

Acronyms and Abbreviations

AC	Alternating Current
A.D.	Anno Domini
AE	Acoustic Emission
ASTM	American Society for Testing and Materials
B.C.	Before Christ
BMI	Bismaleimide
BVID	Barely Visible Impact Damage
CCC	Carbon-Carbon Composite
CF	Carbon Fiber
CFRP	Carbon Fiber Reinforced Polymer
CMC	Ceramic-Matrix Composite
CNC	Ceramic Nanocomposite
CNT	Carbon Nanotube
CTE	Coefficient of Thermal Expansion
CVID	Clearly Visible Impact Damage
DC	Direct Current
DETA	Diethylenetriamine
DGEBA	Diglycidyl Ether of Bisphenol-A
DWCNT	Double-Walled Carbon Nanotube
ERC	Electrical Resistance Change
FRC	Fiber Reinforced Composite
FRP	Fiber Reinforced Polymer
GF	Glass Fiber
GFRP	Glass Fiber Reinforced Polymer
GN	Graphene
GNP	Graphene Nanoplatelets

GO	Graphite Oxide
HM	High Modulus
HS	High Strength
IM	Intermediate Modulus
LRC	Lamina Reinforced Composite
LVI	Low-Velocity Impact
MMC	Metal-Matrix Composite
MNC	Metal Nanocomposite
MWCNT	Multi-Walled Carbon Nanotube
NDT	Non-Destructive Testing
OMC	Organic-Matrix Composite
PAN	Polyacrylonitrile
PEEK	Polyether Ether Ketone
PMC	Polymer-Matrix Composite
PNC	Polymer Nanocomposite
PPS	Polyphenylene Sulfide
PRC	Particulate Reinforced Composite
rGO	Reduced Graphite Oxide
SHM	Structural Health Monitoring
SWCNT	Single-Walled Carbon Nanotube
UHM	Ultra High Modulus
UP	Unsaturated Polyester
USD	United States Dollar
UV	Ultraviolet

Symbols

Latin Symbols

A	Electrode Area	cm²
b	Specimen Thickness	mm
D	Displacement	mm
E_f	Flexural Modulus	GPa
GF	Gauge Factor	–
H	Impact Height	m
i	Phase Element	–
l	Specimen Length	mm
L	Support Span Length	mm
n	Number (of)	–
P	Load	N
R	Electrical Resistance	Ω
R_0	Initial Electrical Resistance	Ω
SD	Standard Deviation	–
t	Time	s
T_g	Glass Transition Temperature	°C
v_0	Impact Velocity	m/s
w	Specimen Width	mm
W	Impact Weight	N
x	Coordinate System	–
X	Value of Single Test	–

Greek Symbols

Δ	Variation	–
ε	Strain	%
ε_f	Flexural Strain	%
θ	Chiral Angle	º
ρ	Density	g/cm^3
ρ_v	Volumetric Resistivity	Ω.cm
σ	Stress	MPa
σ_f	Flexural Stress	MPa
σ_v	Volumetric Conductivity	S/cm

Chapter 1

Introduction

This chapter aims to present an overview of the significance of composite materials in the aeronautical and aerospace sectors, as well as the role of structural health monitoring in enhancing composite materials' safety and service life. The motivation behind this work, its objectives, and the organization of the documentation will also be discussed and described.

1.1 Motivation

Over the last decades, composite materials have revolutionized the way that we design and manufacture products, becoming increasingly important in a wide range of industries where performance and efficiency are critical, such as aerospace, automotive, military, construction, marine, and sports [1].

Generally, a composite material can be described as the combination of two or more materials with the intent of creating a new material that has superior properties than the individual materials alone. The different materials are generally differentiated as matrix phase and dispersed phase (reinforcement). The reinforcement is the load-bearing member whereas the matrix bonds the reinforcing material together and distributes the load among them, as well as protecting against exterior elements. This combination brings major advantages over other existing materials, such as metal or plastics, which are high strength and stiffness combined with the low density of the resultant composite material, allowing for high specific strength and weight reduction in the finished part [2–4].

Regarding the aeronautical and aerospace sector, the most widely used type of composites are fiber-reinforced polymers (FRPs). These types of composites are made up of a polymer matrix, such as epoxy, reinforced with high-strength fibers, e.g., carbon fiber, glass fiber, or aramid fiber [2]. The high strength-to-weight ratio and durability of these composites make them an ideal choice for a vast range of aerospace applications, including aircraft structures, interiors, and engine components. Therefore, driven by the need for lightweight, fuel-efficient, and environmentally friendly aircraft, commercial airplane manufacturers have been gradually replacing several mainstream materials, such as aluminum and titanium alloys, with composite materials. This trend is depicted in Figure 1.1, showing aircrafts such as the Boeing 787 Dreamliner and the Airbus A350 XWB, which are two of the most advanced commercial aircrafts currently in operation, being composed of over 50% composite materials by weight [5]. A clear example of composite materials'

influence in the Boeing 787 construction is seen in Figure 1.2. Being the first commercial airplane to use FRP composites as the primary material for the airframe, with all fuselage sections, wings, as well as horizontal and vertical stabilizers, it stands as a breakthrough of composites in aircraft manufacturing. With a global market value of 29.7 billion USD reached in 2022, it is expected that aerospace composites, mainly FRP, will only continue to grow in the coming years, with an expected revenue of 51.6 billion USD by 2027 [6], assuming an even more prominent role in the aerospace industry.

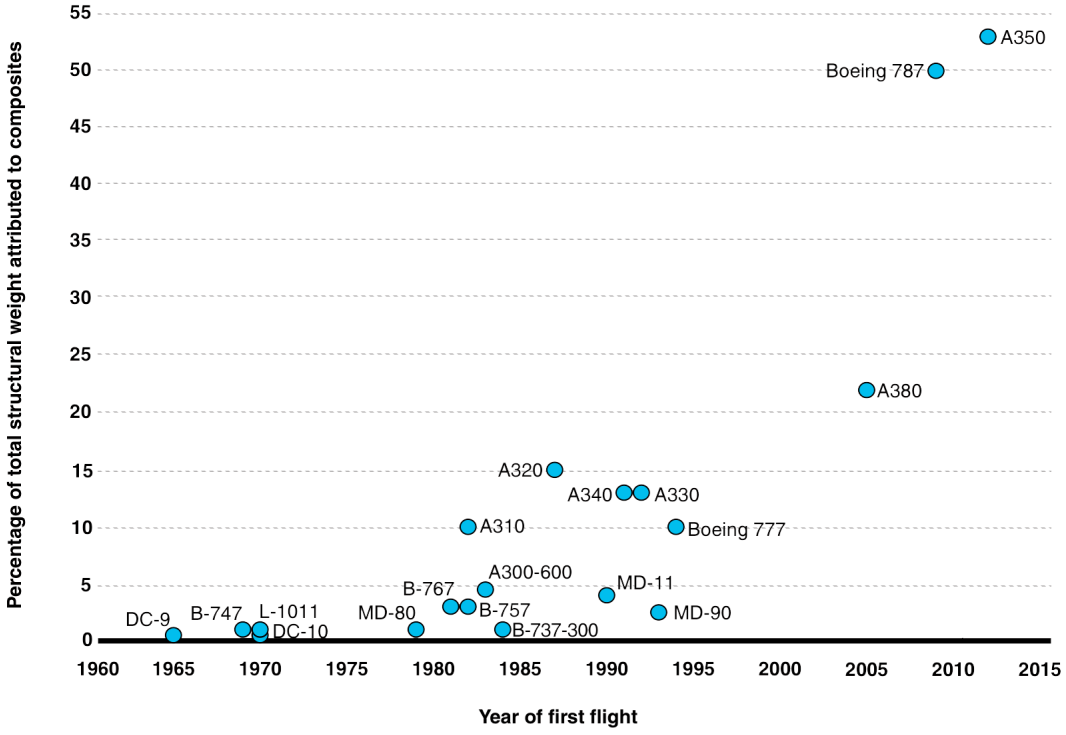

Figure 1.1: Commercial airplane models by percentage of total structural weight due to composite materials, adapted from [5].

Despite the significant advantages offered by FRP composites, they can be vulnerable to defects that weaken the material and compromise its performance. These defects can arise during the manufacturing and assembly processes, such as delamination, fiber misalignment, voids, broken fibers, porosity, inclusions, resin cracks, incorrect cure, etc. [7]. Besides manufacturing and assembly defects, the main factor that affects the in-service life of a FRP composite is the impact of objects. In fact, around 80% of in-service damage to composite aircraft structures is caused by impact strikes, which are often caused by small debris striking the component during aircraft take-off and landing, or by tools accidentally dropped on the surface during maintenance practices.

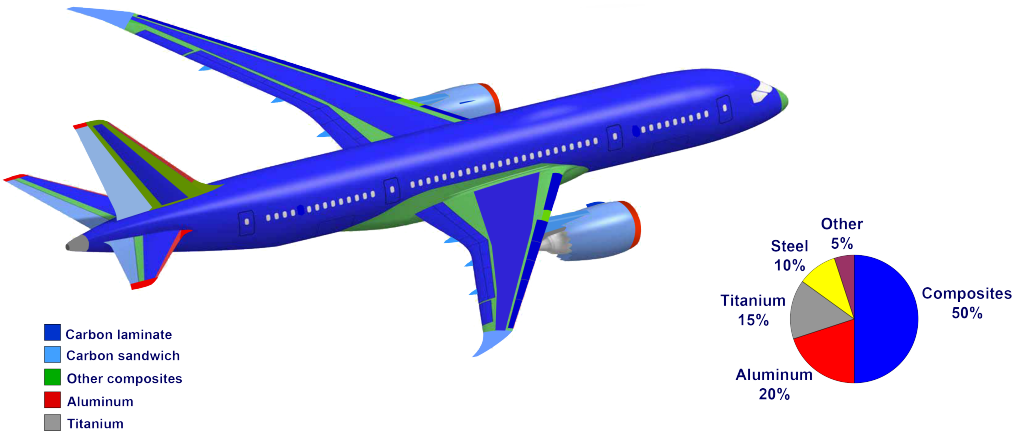

Figure 1.2: Layout and application of various materials in the Boeing 787 Dreamliner, adapted from [8].

As FRP composite structures are particularly sensitive to impact, sub-surface damage in the form of delaminations and cracks may arise, which tend to be barely noticeable on the surface of the material except for a minor indentation [9, 10]. However, such damages have the potential to develop and ultimately result in failure of the composite structural integrity. A schematic cross-sectional view of an impact-damaged laminate is shown in Figure 1.3, revealing substantial subsurface delamination and cracking whose full extent can not be depicted by the surface flaw, which is often invisible or considered of minor importance during visual inspection.

Therefore, early detection, identification, and location of damages in FRP composite materials have become increasingly important in aerospace applications, especially for civil aviation, where safety and reliability standards are very stringent. Because of the possibility of unseen internal failures, composite components and structures are frequently over-designed, which contradicts the benefit of adopting composite materials for weight reduction in the first place. As a result, to attain the full potential of FRPs, it is crucial to monitor and detect composites' internal damage state accurately. To fulfill this requirement, the concept of structural health monitoring (SHM) has been introduced, which allows the detection of composite failure modes during their usage and continuously monitor their health throughout their service life [11].

Non-destructive testing (NDT) methods, such as visual inspection, acoustic emission, ultrasonic inspection, eddy-current, thermography, radiography, etc. [12], can be used during routine inspection and maintenance to identify damage that has occurred during the aircraft's operation. However, NDT methods follow a set timetable, thus they are unable to offer specific details on the beginning or progression of damage in between inspection intervals. Additionally, NDT procedures require pulling the aircraft out of service, meaning they can not be easily applied without seriously disrupting the aircraft's regular operations [7, 13].

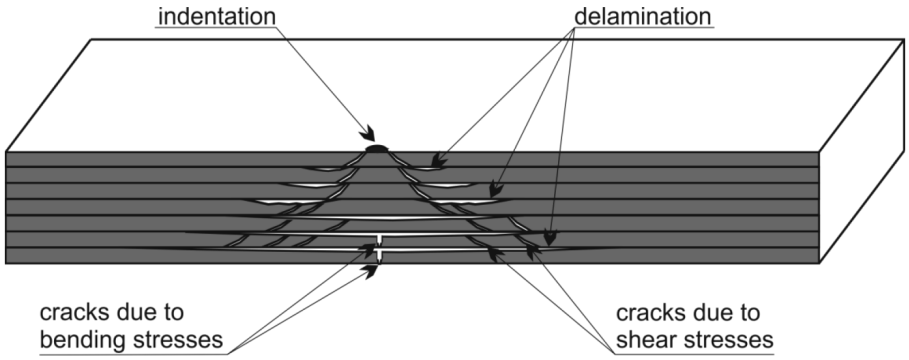

Figure 1.3: Scheme of a barely visible impact damage in a composite structure, from [10].

Alternatively, emerging approaches to SHM capable of continuous detection and monitoring of in-service damage have been proposed, including self-sensing material systems and embedded sensors. Among these, the self-sensing materials stand out as the most prominent, as they are less intrusive to the laminate structure than embedded sensors, which tend to create fiber orientation distortions and mechanical stress peaks with the potential to cause internal damages such as delaminations [14,15]. Hence, with the development of nanotechnology, the integration of nanoparticles such as graphene and carbon nanotubes (CNTs) in FRPs has shown promising results for SHM systems. Besides the extraordinary sensing capabilities, nanocomposites also exhibit excellent mechanical properties, namely enhanced shear strength, fracture toughness, and impact damage resistance [16]. The main benefit of nanoparticles for SHM is the potential for in-service health monitoring, which eliminates the need for expensive equipment, prolonged downtime, and demanding work. This approach can significantly extend an aircraft's operational time by increasing efficiency and lowering costs with the added benefit of obtaining a final composite with enhanced properties. In other words, the ultimate goal of a SHM system is to mimic the functions of the human nervous system, establishing a completely integrated health monitoring network for the future generation of airplanes [11].

Particularly in aerospace structures, continuous SHM may improve safety by early detection of structural damages (e.g. matrix cracks, delaminations, fiber breakage) and enhanced cost-efficiency by minimizing on-demand service needs. As a result, the optimum way to achieve structural health monitoring is to use the composite material as the sensor. Based on this premise, this work aims to develop a self-sensing composite through the incorporation of CNTs in an epoxy matrix, which, using the electrical resistance change (ERC) method, could serve as a means to monitor damage initiation and propagation within the FRP structure, particularly under a low-velocity impact event.

1.2 Objectives

This work has, at its core, the development of a self-sensing composite able to detect damage within its structure when subjected to low-velocity impact events. As such, a woven glass fiber composite will be reinforced with an epoxy resin enhanced with multi-walled carbon nanotubes. By doing so, a multifunctional composite is expected to be attained, with improved mechanical performance and semi-conductive electrical properties, enabling the detection of damages within the composite by measuring the changes in electrical resistance.

In order to accomplish the stated objectives, the following tasks need to be fulfilled:

- Investigate the state-of-the-art applications and distinguishing properties of fiber-reinforced composites in aeronautics and aerospace fields.
- Explore the demand for novel impact damage detection methods in FRP composites.
- Manufacturing of glass fiber reinforced composites using CNT-enhanced epoxy resin.
- Determine the ideal amount of carbon nanotubes required in the epoxy matrix to create an electrically semi-conductive composite.
- Perform the necessary adjustments to the manufacturing process to ensure an even distribution of carbon nanotubes within the epoxy matrix.
- Before and post-impact mechanical characterization of the composites via Young's modulus, flexural strength, and failure strain properties.
- Analysis of the impact response and damage characterization of the composites subjected to low-velocity impacts.
- Electromechanical characterization of the self-sensing composite piezoresistive effect.
- Real-time detection of low-velocity impact damages through the electrical resistance change method.
- Comparison and validation of the experimental results obtained with the reported in the literature.

1.3 Dissertation Outline

This dissertation is comprised of five chapters, organized as follows:

- The current chapter, **Introduction**, starts with the motivation behind this dissertation, where a general contextualization about the importance of FRP composites in the aeronautical and aerospace industries is presented, emphasizing the continuous growth of CNTs as a disrupting solution for most advanced and effective SHM applications. Furthermore, the main objectives of this research are highlighted.
- Chapter 2, **State-of-the-Art**, provides an in-depth introduction and contextualization of the main topics developed within the research context. As such, an extensive literature review was carried out, covering the fundamentals associated with composite materials within the aerospace industry, followed by a comprehensive analysis of low-velocity impact events in composite structures, finally delving into the domain of structural health monitoring in FRP composites.
- Chapter 3, **Experimental Procedure**, outlines the materials used, the experimental process for sampling manufacturing, and the flexural, low-velocity impact, and piezoresistive testing procedures. Additionally, explanations of the working principles and refinements to the procedure techniques are included as needed to provide further support.
- Chapter 4, **Results and Discussion**, which is divided into three sections covers the experimentally obtained results. Firstly, the pre and post-impact flexural properties will be presented, followed by the low-velocity impact response and characterization, ending with the electrical resistance and piezoresistive measurements for damage sensing.
- Chapter 5, **Conclusion and Future Work**, provides a comprehensive overview of the research conducted within this dissertation, summarizing the key findings and highlighting any potential avenues for further investigation.

Chapter 2

State-of-the-Art

This chapter presents a comprehensive theoretical review of the main concepts associated with the SHM of CNT-enhanced composite materials. Section 2.1 will consist of an introduction to composite materials in a framed historical evolution, moving subsequently to coverage of the types of reinforcements and matrices predominantly used in the aerospace industry, as well as a brief overview of nanocomposites. After that, Section 2.2 will address impact damage in laminated composite materials, starting by presenting the different classifications of impact phenomenons, with particular emphasis on low-velocity impact. Further descriptions of the test methods, failure modes, impact response, and parameters affecting impact damage are presented in this regard. Lastly, Section 2.3 will cover the domain of structural health monitoring in FRP composites, particularly when incorporating CNTs into the polymer matrix, especially epoxy. A general overview of the fundamental principles related to the electrical behavior of CNT-filled polymers, accompanied by an extensive review of prominent works within this field, will also be provided.

2.1 Composite Materials

2.1.1 Introduction to Composite Materials

The definition of composite materials varies widely in the literature, lacking universal agreement. Nevertheless, a fundamental understanding recognizes that composite materials consist of at least two distinct phases with a finite and distinct interface between them [17]. As previously mentioned, a composite material can be described as the combination of two or more materials whose final properties and performance are superior to those of each individual material. However, such a definition can be very general, as it can be applied to any type of material. As an example, materials such as wood and animal bones are natural composites, which have been used since primitive times for hunting, fishing, and agriculture [2, 18]. As such, a more precise definition states that a composite material combines two or more materials that maintain separate phases, retaining their unique properties, i.e., the components of a composite do not disappear or lose their unique properties. Composites comprise a matrix responsible for protecting and binding the other phase material, called reinforcement. Because the matrix is softer and weaker, it distributes the applied loads and increases the composite's ductility and formability. The reinforcement has high strength and stiffness, bearing the loads applied on the structure and contributing to the overall mechanical properties of the composite [1].

The first records of composite materials' use date as early as 3400 B.C., approximately 5000 years ago, when the first man-made fibrous composite was created in the ancient Mesopotamian civilization, consisting of several wood pieces stuck together in various directions to form the first form of plywood. Roughly around the same period, the Egyptians used a similar technique by adhering two layers of fibrous papyrus plant strips perpendicular to one another, creating the first kind of paper, the so-called "papyrus". Around 1500 B.C., the Mesopotamian and Egyptian civilizations developed the first composite bricks using a mixture of mud reinforced with straw, obtaining strong composite bricks to create more durable buildings. Later, in 1200 A.D., the Mongols invented the first composite archery bow, made from layers of bamboo, horns, and animal sinew. These bows were pressed and wrapped with silk or birch bark and finally sealed entirely using pine resin. It was smaller and more compact than earlier composite bows but was incredibly powerful and allowed Mongol archers to shoot accurately from horseback at distances as great as the length of five football fields. These bows remained the most powerful and feared weapons until the invention of firearms later in the 14th century [1, 19].

The development of composites entered a new phase around the 1870s and 1890s when a chemical revolution introduced the first man-made polymer resins. These synthetic resins could be solidified from a liquid state through polymerization, replacing natural resins from plants and animals that were previously the only available source of binders and glues [1]. During the 1940s, the composite materials field saw major breakthroughs due to World War II, booming the demand for lighter, stronger, and weather-resistant materials for military aircraft and equipment, taking FRP composites from the laboratory into actual production. By 1945, more than 3 thousand tonnes of glass fiber had been used for a variety of products, mostly for military uses [20]. Composite materials development received new momentum from the drive for aerospace dominance that started during the Cold War in the 1950s and accelerated in the 1960s and 1970s. Numerous composites-based products became widespread, including sports cars, trucks, boats, ducts, pipes, and storage tanks. The invention of the first carbon fiber, used in numerous rocket engines and airplanes, was patented in 1961. Around this time, other significant fibers were also made commercially available, such as boron fibers in 1965 and aramid fibers (DuPont's Kevlar®) in 1971 [21]. In the early 2000s, many commercial items started using nanotechnology, and composites were no exception. By introducing bulk carbon nanotubes as reinforcement in polymer composites, enhanced mechanical, thermal, and electrical properties are obtained [20]. In Figure 2.1, the evolution of composite materials throughout history and the most relevant milestones in each period can be visualized.

Nowadays, composite materials are still in constant development, with most of their use focused on the transport, automotive, renewable energies, and aerospace sectors. Particularly in aerospace, the strength-to-weight ratio of modern composites makes it a key factor in achieving better performance and weight reduction to meet ever-increasing fuel costs and environmental regulations of commercial aviation.

Considering the development of composites from ancient to modern times, as well as their potential use in the future, it is clear that continuous research and development will be conducted, and the advent of new fiber and matrix types, as well as new manufacturing and recycling techniques, will undoubtedly accelerate and expand the use of composite materials [22].

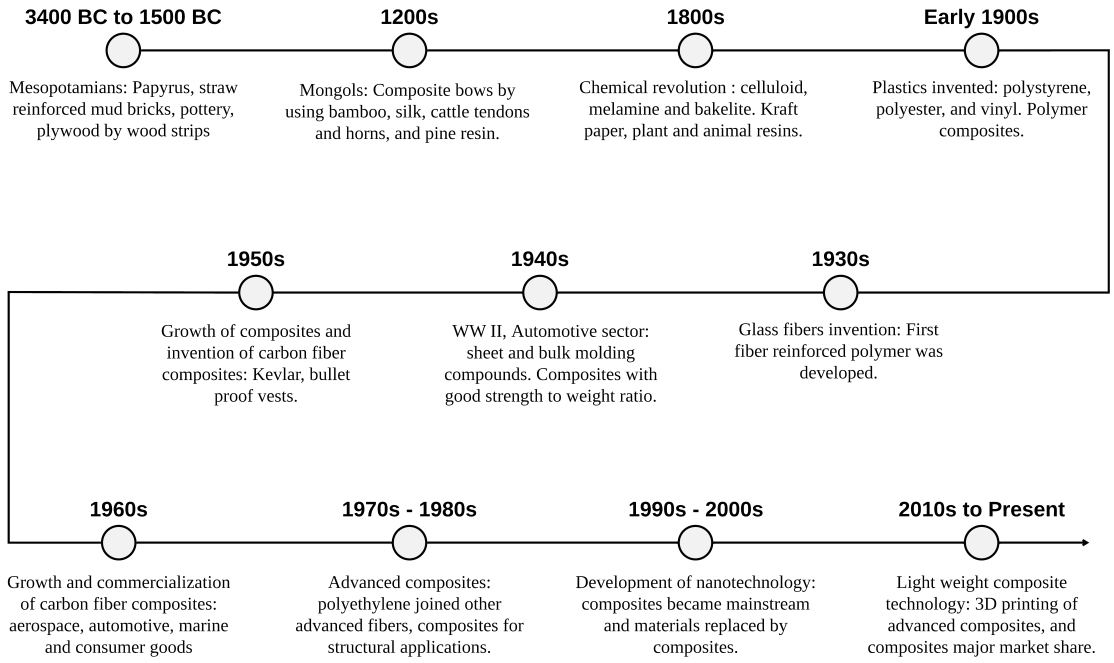

Figure 2.1: Historical evolution of composite materials, adapted from [1].

2.1.2 Types of Composite Materials

According to the literature, composite materials are typically divided into two major categories [23]. The first category is based on the type of matrix used in the composite material, and its main classes include:

- Polymer Matrix Composites (PMCs);
- Metal Matrix Composites (MMCs);
- Ceramic Matrix Composites (CMCs);
- Carbon-Carbon Composites (CCCs).[1]

[1]Frequently PMCs and CCCs are called organic matrix composites (OMCs)

The second category is based on the type of reinforcement, and it can be divided into:

- Fiber-reinforced composites (FRCs);
- Particulate-reinforced composites (PRCs);
- Lamina-reinforced composites (LRCs).

Besides that, composites can also be categorized according to their size and scale. This means that a composite with reinforcements in the size range of 1 to 100 nanometers is termed a nanocomposite. This includes nanoparticles, microfibers, nanotubes, and other nanostructured materials. The exact size range can vary depending on the specific type of nanocomposite and its intended application. To achieve the desired properties, several materials are artificially synthesized to create the aforementioned composites. Yet, there is another type of composites known as ”natural composites,” which are easily accessible in nature.

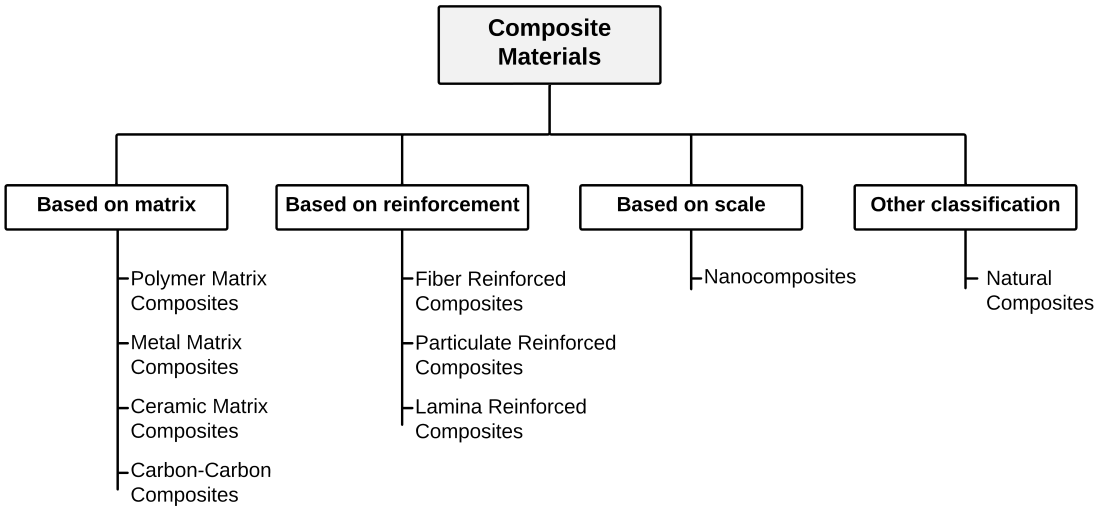

Figure 2.2: Broad classification of composite materials, adapted from [1].

As it can be concluded, composite materials are subdivided into numerous categories, which branch out into even more specific classes, making the understanding of all these concepts a very time-consuming task, requiring extensive research and analysis, which is beyond the scope of this work. Therefore, the present work will be focused on the main concepts behind the core of its implementation, which relies on the manufacturing of a composite material made from fibers reinforced with a polymeric matrix. Hence, the following sections are intended to cover the main types of fibers used as reinforcement, as well as the different existing polymeric matrices used to manufacture FRP composites.

2.1.3 Fiber Reinforcements

Reinforcements can appear in the form of particles, flakes, whiskers, short fibers, continuous fibers, or sheets. Since materials are stronger and stiffer in their fibrous form than in any other, most reinforcements used in composites have a fibrous structure [24]. As previously discussed, the fibers, as a reinforcement element, are responsible for the mechanical properties of composite materials. Various fibers can be used as reinforcement for a wide range of composite applications, which comprise mainly synthetic and natural fibers, as seen in the diagram shown in Figure 2.3.

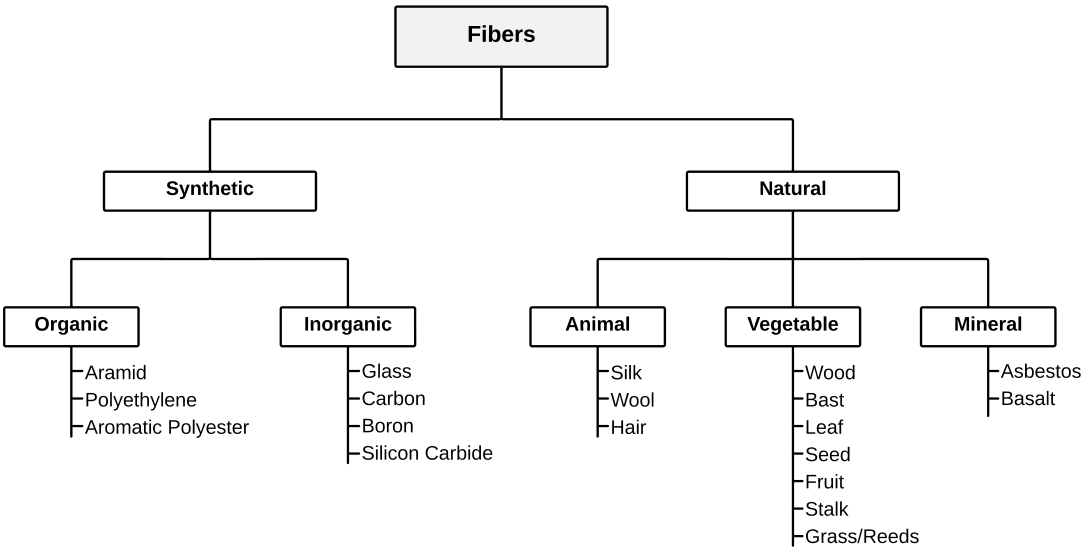

Figure 2.3: Classification of synthetic and natural fibers, adapted from [25].

Synthetic fibers are more attractive because of their exceptionally high stiffness, strength, low density, and ability to achieve specific properties. On the other hand, natural fibers are suitable for less demanding applications, offering a significant advantage regarding their affordable price. However, the characteristics of natural fibers depend on their place of origin, thus, it might be impossible to create a natural fiber-reinforced composite with specific desired characteristics. Additionally, natural fibers suffer from higher degradation under normal environmental conditions, whereas synthetic fibers are far more resistant to environmental effects [24, 25].

With that in mind, the following sections will cover the most popular and commonly used synthetic and natural fibers currently used, providing some details about their manufacturing, properties, and overall applications for composite structures.

2.1.3.1 Synthetic Fibers

Glass Fibers

Glass fibers are, by far, the most widely used synthetic reinforcement in the manufacturing of composite materials. These fibers are composed essentially of silica, which is associated with various types of oxides, including aluminum, calcium, and boron. Currently, there are two main industrial processes to produce glass fibers: the direct melt procedure and the indirect marble melting procedure. The most common technique is the direct melt procedure, which consists of straining molten glass through a platinum-rhodium alloy spinner with very precisely sized holes, varying from 2 to 20 μm in diameter [25, 26].

There are several types of glass fibers, which vary depending on their alkali content, resulting in fibers tailored for different desired applications. The main grades of glass fibers are [20]:

- Grade A: high alkali grade glass, originally made from window glass.
- Grade C: chemical-resistant grade glass for acid environments or corrosion.
- Grade D: low dielectric grade glass, good transparency to radar (quartz glass).
- Grade E: electrical insulation grade (most common reinforcement grade);
- Grade M: high modulus grade glass;
- Grade R: reinforcement grade glass (European equivalent of S-glass);
- Grade S: high-strength grade glass, of which S2-glass is a popular variant. Compared to E-glass, this fiber has a higher Young's modulus and temperature resistance, despite being more expensive.

Type A fiber, highly alkaline, was gradually replaced by type E fiber, a borosilicate glass with a low content of alkaline chemicals and good electrical, physical, and chemical properties. Types C, D, E, R, and S are currently the most common fibers produced for usage in composite materials. Both S and R fibers are produced from high strength glass and are widely applied in the aeronautical industry.

The key benefits of glass fibers include their great tensile strength, low cost, excellent insulating qualities, and strong chemical resistance. Glass fiber shortcomings include their relatively high density, low tensile modulus, sensitivity to handling abrasion (which frequently lowers their tensile strength), high hardness, and relatively low fatigue resistance [25]. In Table 2.1, the mechanical properties of the main glass fiber grades can be found.

Table 2.1: Mechanical properties of the main glass fiber grades [20].

Fiber	Density [g/cm^3]	Young's Modulus [GPa]	Tensile Strength [GPa]	Failure Strain [%]
A (alkali)	2.46	73	3.1	3.6
C (chemical)	2.46	74	3.1	-
D (dielectric)	2.14	55	2.5	-
E (electrical)	2.55	71	3.4	3.37
R (reinforcement)	2.55	86	4.4	5.2
S (strength)	2.5	85	4.58	4.6
S_2	2.46	90	3.62	-

Carbon Fibers

The demand for reinforcement fibers with higher strength and stiffness than those of glass fibers' has led to the development of carbon fibers. These were first discovered in 1958 by Roger Bacon, which culminated in his innovative research in 1960 [27]. The first CFs were created by heating strands of rayon (cellulose) until they were carbonized. Early carbon fibers were not very strong, and their potential for use in advanced applications was not yet recognized. It wasn't until the 1960s and 1970s that the high-strength carbon fiber development didn't truly take off when researchers in the United Kingdom and Japan worked to enhance both the materials' characteristics and the methods used to manufacture them [28].

The most widely used technique in the production of these fibers consists of the thermal decomposition of various precursors, such as polyacrylonitrile (PAN), pitch, rayon, and some other potential precursors such as lignin and polyethylene [20]. Nowadays, PAN is used as the main precursor which accounts for 90% of the market material for carbon fiber production [29]. Although the specific treatment for each precursor is different, it follows the following sequence: spinning, stabilization, carbonization, and the application of a coating to improve its handling. The modulus of carbon fibers depends on the degree of perfection of the alignment, which varies considerably with the manufacturing route and conditions. Regarding its modulus, CFs can be divided in [25]:

- Ultra High Modulus (UHM): fibers with modulus higher than 700 GPa and tensile strength of approximately 3 GPa;
- High Modulus (HM): fibers with modulus between 350 and 450 GPa and strength-to-modulus ratio $\leq$ 0.01;

- Intermediate Modulus (IM): fibers with modulus between 350 and 450 GPa and strength-to-modulus ratio > 0.01;
- High Strength (HS): fibers with tensile strengths between 3 and 5 GPa and strength-to-modulus ratio between 0.015 and 0.02.

Carbon fibers have several advantages, including high stiffness, high tensile strength, low weight, high chemical resistance, high thermal conductivity, and negative/null coefficient of thermal expansion (CTE). Nevertheless, CFs have some drawbacks. They are brittle, have poor impact resistance, limited elongation, and have relatively low compressive strength. Additionally, although the cost has been progressively dropping, they are still quite expensive [21].

In general, carbon fibers present many unique properties that make them a top choice for high performance and extremely demanding applications, which go from aerospace to automotive, marine, military, and sports. Table 2.2 gathers the mechanical properties of several commercially available carbon fibers from different manufacturers.

Table 2.2: Mechanical properties of commercially available carbon fibers [25].

Manufacturer	**Product (Precursor)**		**Density [g/cm^3]**	**Young's Modulus [GPa]**	**Tensile Strength [GPa]**	**Failure Strain [%]**
Amoco	T300	(PAN)	1.75	228	3.31	1.4
	P75	(Pitch)	2	517	2.07	0.4
	P100	(Pitch)	2.15	724	2.24	0.31
HEXEL	IM-6	(PAN)	1.74	296	4.88	1.73
	IM-7	(PAN)	1.77	276	5.3	1.81
	UHMS	(PAN)	1.87	441	3.45	0.81
Toray	T1000	(PAN)	1.82	294	7.06	2.4
	M40	(PAN)	1.81	392	2.74	0.6
	M60J	(PAN)	1.94	588	3.92	0.7
Nippon Graphite Fiber Corp.	CN60	(Pitch)	2.12	620	3.43	0.6
	CN90	(Pitch)	2.19	860	3.43	0.4
	XN145	(Pitch)	1.85	155	2.4	1.5

Aramid Fibers

Aramid fibers are the most well-known organic fibers used as reinforcement in the composites industry. These aromatic polyamides, which are members of the nylon family, are typically produced through a process called wet spinning, which involves dissolving the polymer in a solvent and then extruding the solution through a spinneret to create fibers. The fibers are then stretched and heat-treated to orient the polymer chains and increase their strength and stiffness. Well-known commercial names of aramid fibers include Kevlar® and Nomex® manufactured by DuPont, and Twaron® from Teijin [24,25]. Regarding its classification, aramid fibers can be divided into two main types:

- Meta-aramid: such as Nomex®, are known for their flame resistance and thermal stability. Are commonly used in applications such as protective clothing for firefighters, military personnel, and race car drivers.
- Para-aramid: such as Kevlar® and Twaron®, are known for their exceptional strength and low weight. They are commonly used in body armor, helmets, ropes, and cables.

Aramid fibers' main advantages are their excellent stiffness-to-weight ratio, exceptional ballistic impact and fatigue resistance, good vibration damping ability, and high resistance to organic solvents, fuels, lubricants, and acids. Their coefficient of expansion behaves similarly to carbon fibers. The main disadvantages are low compressive and flexural strength, as well as high sensitivity to interlaminar shear [26]. Regarding Kevlar® fibers, the three well-known varieties are the K 29, K 49, and K 149. Kevlar® 29 has half the modulus but twice the strain before failure compared to Kevlar® 49. Strain-to-failure value, for instance, is crucial for ballistic vests, making K 29 an excellent choice. On the other hand, stiffness is the primary consideration for automotive and aerospace applications. As a result, K 49 or K 149 fibers are preferred for this purpose.

Table 2.3: Mechanical properties of commercially available aramid fiber yarns [24,30,31].

Manufacturer	Product	Density [g/cm³]	Young's Modulus [GPa]	Tensile Strength [GPa]	Failure Strain [%]
DuPont	K 29	1.44	65	2.8	3.5 - 4
	K 49	1.45	125	2.8	2.8
	K 149	1.47	147	2.5	1.5 - 1.9
	Nomex®	1.38	17	0.552	35
Teijin Aramid	Twaron®	1.44 - 1.45	60 - 120	2.4 - 3.6	2.2 - 4.4
	Technora®	1.39	74	3.4	4.5

2.1.3.2 Natural Fibers

In general, the term natural fibers refers to fibers that are derived from plants, minerals, or animals and are neither synthetic nor man-made. Current environmental concerns have an impact on material science and technology, and the rising demand for a clean environment leads to the development of green materials and the use of natural products. As a result, there is an increasing need for high-performance engineered components made from renewable natural resources, and researchers are constantly investigating the potential of natural fiber as the reinforcing phase of polymer composites. Natural fiber-reinforced composites are used in applications with less significant load-bearing since it is difficult to dispose of synthetic fiber-reinforced composites when they reach the end of their useful life. Consequently, natural fibers have become one of the most appealing study subjects in the composites industry recently because of their advantages of reasonable mechanical qualities, low density, environmental advantages, renewability, and economic viability [20, 25]. In this section, some of the most commonly used natural fibers will be generally presented, with an overall comparison of their respective properties given in Table 2.4.

Bast Fibers

A wood core surrounded by a stem constitutes a plant's bast. The stem is composed of bundles of fiber, and each bundle contains a large number of individual filaments. Lignin or pectin is what keeps the fiber bundles together. During the retting procedure, the pectin is taken out, which makes it possible to separate individual fiber bundles. Flax, hemp, jute, kenaf, and ramie are the most commonly used plants to obtain fiber bundles from its bast [32].

Leaf Fibers

Leaf fibers are typically coarser than bast fibers, amongst which sisal and palm fibers are mostly used. Sisal is the most significant leaf fiber because is relatively stiff and has high tensile strength, making it ideal for use in products that require strength and durability. It is widely used in the production of various products such as ropes, twine, and carpets, and is obtained from the leaves of the agave plant [32].

Seed Fibers

The most popular seed fibers currently in use are cotton, coir, and kapok. Cotton fiber is the most widely used seed fiber in the world and is mainly employed in the textile industry. Coir fiber is derived from the husk of the coconut. It is strong, flexible, and highly resistant to moisture, therefore ideal for use in products that are exposed to water or other liquids. Kapok fiber is a short fiber with a smooth, silky surface. It is lightweight, buoyant, and highly water-resistant. However, kapok fiber is not very strong and can break easily [32].

Plant fibers from the leaf and bast classes are the most sought-after characteristics for composite purposes, according to the composites industry. However, some factors such as the age of the plant, growing conditions, harvesting, humidity, soil quality, temperature, and processing processes, have a considerable impact on the quality of natural fiber, driving the need for limiting the on-field processing in order to increase consistency and lower costs [20, 25].

Table 2.4: Mechanical properties of commonly used natural fibers [20, 25].

Fiber	**Density [g/cm³]**	**Young's Modulus [GPa]**	**Tensile Strength [MPa]**	**Failure Strain [%]**
Jute	1.46	10 -30	400 - 800	1.5 - 1.8
Flax	1.4	27	344	2.7 - 3.2
Kenaf	1.2	35 - 53	389 - 930	2.7 - 6.9
Hemp	1.48	70	550 - 900	1.6
Ramie	1.5	90	400 - 938	3.6 - 3.8
Sisal	1.33	38	600 - 700	2 - 3
Coir	1.25	4 -6	220	15 - 25
Cotton	1.5 - 1.6	5.5 - 12.6	287 - 597	3 - 10
Kapok	0.4	41	93.3	-
Pineapple	1.3 - 1.4	61.4 - 128	170 - 1627	1 - 3
Banana	1.3 - 1.4	3.4 - 32	54 - 789	2 - 7

2.1.4 Polymer Matrix

The matrix phase used in a composite can be made of any material. Yet, as it was previously mentioned, matrix materials are fundamentally made of metals, ceramics, and polymers. In fact, polymers comprise the majority of matrix materials in the composites market. Many different polymer matrices can be used to create composite materials, which are divided into three major categories, as seen in Figure 2.4.

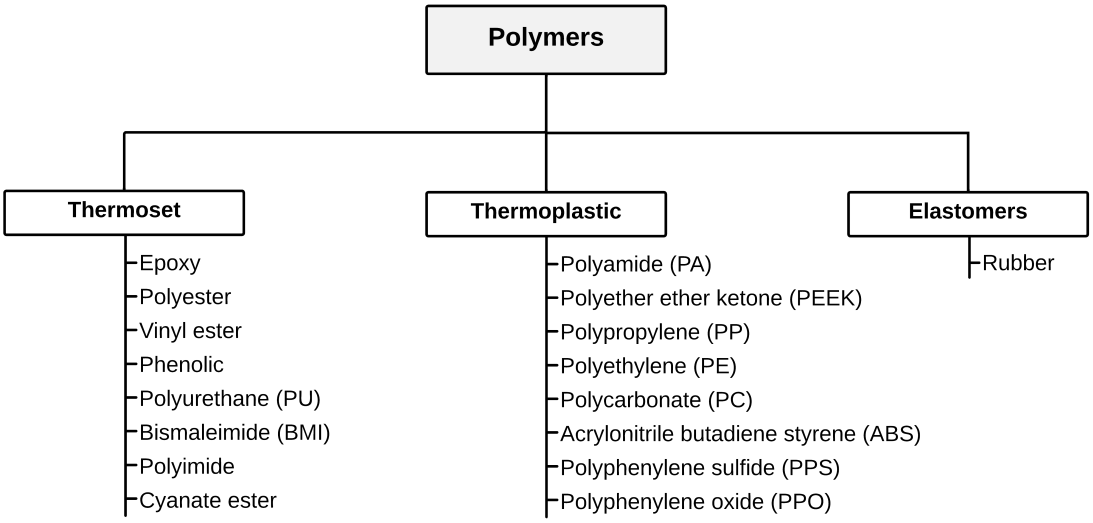

Figure 2.4: Classification of polymers, adapted from [25].

Thermoset and thermoplastics are the class of polymers most commonly used for composite matrices. Both have many desirable properties as a matrix for composite applications, however, thermosets have been favored in this regard. High performance thermoplastics typically have high melting points, which means that processing must occur at high temperatures, whereas thermoset resins can be processed at room temperature or at lower temperatures. Achieving proper wetting of fibers when using thermoplastics is also challenging without applying pressure, which limits the use of continuous fibers. As a result, continuous or long fiber-reinforced thermoplastics are not commonly used. Additionally, thermoplastics undergo more complex stages and require expensive equipment, as their properties are highly affected by the manufacturing process [33].

In sum, thermoplastics dominate the plastics industry as a whole, particularly in applications that do not require any type of reinforcement. However, regarding the composite materials industry, thermoset polymers are clearly the dominant choice for composite matrices [33]. As such, the following section will be focused on the thermoset class of polymers, covering some of the most used as the matrix for composite materials.

2.1.4.1 Thermoset Polymers

Thermosets are materials that, typically, change from a liquid to a solid as a result of a chemical reaction or curing. The substance has tiny, unconnected molecules known as monomers in its uncured state. The chemical reaction or curing process that results in the material solidification is started by the addition of a second substance acting as a cross-linker, curing agent, catalyst, and/or the presence of heat or other activating factors. The transition of the thermoset state is permanent and irreversible. Hence, after solidifying, exposure to high heat will result in the material degrading rather than melting. This is due to the fact that these materials often degrade at temperatures below their melting point, known as glass transition temperature (T_g). For a thermosetting polymer, the T_g increases with increasing cross-link density [20, 33].

The present sub-section will provide a description of the most relevant thermoset polymers used as composite matrices. In Table 2.5, mechanical and physical properties from the described, and other thermoset polymers can be visualized.

Epoxy

Epoxy resins are one of the major thermoset matrix materials actually in use and the most predominant in high performance applications such as aerospace. Epoxy resins come in a wide variety of chemical formulations, most of them based on diglycidyl ether of bisphenol-A (DGEBA). One of the most desirable features of epoxy resins is their versatility. Various additives can be used to modify its characteristics, such as diluents to reduce viscosity, flexibilizing agents to increase flexibility, accelerators to speed up the curing process, and agents for protection against ultraviolet (UV) radiation. Curing agents, such as diethylenetriamine (DETA), crosslink the epoxy structure, giving it superior mechanical properties such as stiffness, strength, and glass transition temperature, but decreases toughness [34].

The main advantages of epoxy resin are high mechanical strength, abrasion and chemical resistance, low viscosity, good adhesion properties to a wide variety of fibers, curing process without releasing volatile gases, great dimensional stability as a result of its low cure shrinkage, low moisture absorption, and prolonged operating temperatures typically between 100 and 220°C. However, epoxy resins also have some limitations, as they have poor resistance to UV light and can degrade when exposed to sunlight, which can lead to yellowing and reduced mechanical properties. They can also be brittle at low temperatures, which limits their use in some applications [26].

Unsaturated Polyester

The most often used thermosetting resins for composites are unsaturated polyesters, sometimes known as thermoset polyesters. Unsaturated polyester (UP) resin is produced when an unsaturated dibasic acid (maleic or fumaric) and a glycol (ethylene, propylene, or diethylene glycol) condense. The term unsaturated refers to a molecule that has reactive sites. There are various reasons for the extensive use of unsaturated polyester, not the least of which is its low cost. Unsaturated polyesters are typically 25% less expensive than vinyl esters and 35% to 50% less expensive than epoxies [21, 34].

In addition to being more affordable, polyester thermosets also benefit from being simple to cure, simple to mold, and having adequate resistance to water, a variety of chemicals, weathering, and aging. It easily mixes with glass fibers and can resist temperatures as high as 80 °C. Polyester resins experience a 4 – 8% shrinkage after curing. However, polyester thermosets have a number of shortcomings or limitations in terms of characteristics and production, such as relatively poor durability, brittleness, and concerns with air pollution. Yet, overall it seems that the benefits outweigh the drawbacks, and polyesters are still widely used for many composite products, such as glass fiber reinforced boats, pipes, shower stalls, etc. [20, 34].

Vinyl Ester

Vinyl esters are a class of thermosetting resins that resemble both unsaturated polyesters and epoxies and appear to fit somewhere in between. It is produced by the reaction of an unsaturated carboxylic acid with an epoxy resin. Although they are not as expensive as epoxy resins, vinyl ester resins are slightly more expensive than unsaturated polyesters. Vinyl esters outperform polyesters in terms of toughness and corrosion resistance (to organic solvents and water), but they typically fall short of epoxies in these areas [21].

These resins feature excellent chemical resistance, high tensile strength, low viscosity, fast curing process, and affordable price. Vinyl esters are then utilized in applications where cost is a crucial consideration but where the chemical resistance and/or toughness of unsaturated polyesters are insufficient. Therefore, vinyl ester resin applications for composites manufacturing are focused in corrosive environments, and frequently used in the production of pipes and tanks for the chemical industry. The main disadvantage is the high volume shrinkage, which can be as high as 10% [21, 26].

Phenolic

The first thermoset materials synthesized were phenolic resins, under the name of Bakelite® by Leo Bakeland in 1907. Phenolic resins (phenol formaldehyde) are produced by the reaction of phenol with formaldehyde. The main benefits of phenolic resins are superior fire resistance, outstanding high-temperature performance, long-term durability, and higher resistance to hydrocarbons and chlorinated solvents. The primary limitation is high volatile emissions during curing. The finished product will have numerous pores if strong pressure is not applied throughout the curing process. Due to high cross link densities, phenolic resins have high shrinkage and are quite brittle. Besides, they are 10 to 15% more expensive than polyester thermosets [21, 33].

Although having appealing costs and properties, phenolics are far less frequently used in fiber-reinforced composites than polyesters, epoxies, or vinyl esters, having a much larger market for non-reinforced products, like electrical switches, automotive molded components, plywood adhesives, and even billiard balls. Nonetheless, some of phenolics' main benefits, particularly their low flammability, are so compelling that their use as a matrix for composites made of fiberglass and carbon fiber is considerably growing [21].

Table 2.5: Properties of commonly used thermoset polymer resins [21, 33].

Matrix	**Density** **[g/cm³]**	**Young's Modulus [GPa]**	**Tensile Strength [MPa]**	**Failure Strain [%]**	**Cure Shrinkage [%]**	T_g **[°C]**
Epoxy	1.2 - 1.3	2.7 - 4.1	55 - 130	2 - 6	1 - 5	180
UP	1.2	34 - 105	2.1 - 3.5	2.5	5 - 12	80
Vinyl Ester	1.2	35 - 53	389 - 930	2.7 - 6.9	5.4 - 10.3	80
Phenolic	1.3	70	550 - 900	1.6	-	-
BMI	1.4	90	400 - 938	3.6 - 3.8	-	230 - 290

2.1.5 Nanocomposites

Nanocomposites are materials that comprise two or more constituents with different physical and chemical properties that are segregated at the microscopic level, containing a material having at least one dimension below 100 nm [23]. Similar to composites, nanocomposites can be divided into four categories based on the kind of matrix, which include polymer nanocomposites (PNCs), metal nanocomposites (MNCs), ceramic nanocomposites (CNCs), and carbon nanocomposites [1].

Regarding the use of composite materials in the aerospace industry, polymeric nanocomposites are of particular importance due to the high prevalence of polymeric matrices for manufacturing of composite structures, namely FRP composites. Polymer nanocomposites offer several advantages that enable them to compete with conventional materials, including [35]:

- Stiffness and strength improvement with minimal loss of ductility and impact resistance;
- Superior thermal stability;
- Less residual stress and shrinking;
- Customized optical, electronic, and electrical properties;
- Relatively low-reinforcement content.

Due to these advantages, several nano-reinforcements have been identified as potential candidates for structural PNCs. These include carbon nanomaterials, clay layers, and clusters of metal oxides, nitrides, and carbides. Additionally, PNCs are also commonly associated with hybrid composites, which combine two or more types of reinforcements within a single matrix [4]. As such, in the context of FRPs, hybrid composites refer to the incorporation of both traditional macro-scale fibers (e.g., glass or carbon fibers) and nanoscale particles (e.g., CNTs) in the polymer matrix. The combination of macro-scale fibers and nanoparticles has the potential to create multi-functional fiber-reinforced composite structure's with enhanced physical, mechanical, thermal, and electrical properties, which are very appealing to applications in engineering fields, such as structures, transportation, defense and bio-medicine.

Currently, carbon nanomaterials have been receiving the attention of many researchers in the field of polymer nanocomposites due to their unique properties capable of improving the properties of the polymeric matrix. In this sub-section, special attention will be given to commonly used carbon nanomaterials in PNCs, with emphasis in carbon nanotubes.

2.1.5.1 Carbon Nanomaterials

Carbon nanomaterials have garnered significant attention in recent years due to their exceptional properties and wide-ranging applications. These materials, characterized by their unique nanostructure, exhibit remarkable electrical, thermal, and mechanical properties. Carbon nanomaterials encompass a diverse family of materials, including carbon nanotubes, graphene, and nanofibers, each with distinct structures and properties. Their exceptional properties arise from their high surface-to-volume ratio, allowing for strong surface interactions and enhanced performance [35].

Carbon nanomaterials hold immense potential for various fields, including electronics, energy storage, composites, and biomedical applications. This chapter gives an overview of carbon nanomaterials, highlighting their properties, synthesis methods, and applications. A schematic representation of some of these materials is depicted in Figure 2.5

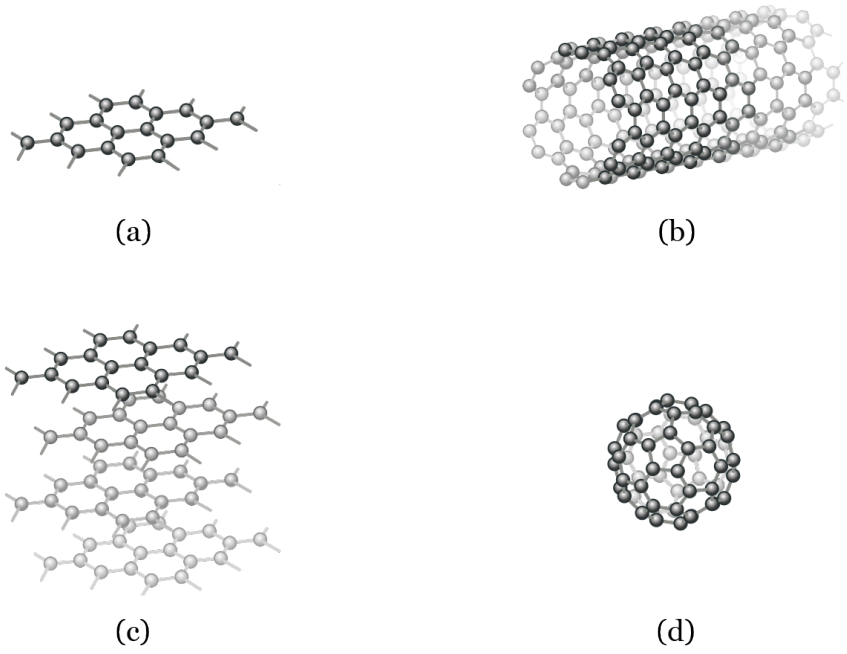

Figure 2.5: Carbon nanomaterials: (a) graphene; (b) carbon nanotube; (c) graphene nanoplatelet; (d) bucky ball, adapted from [36].

Graphene (GN)

Graphene is a two-dimensional carbon allotrope composed of a single layer of carbon atoms arranged in a hexagonal lattice. Graphene is considered the fundamental building block of other graphite-related substances such CNTs, graphite oxide, and fullerene [37]. GN sheets have drawn significant interest in the fields of chemistry, physics and materials science due to their exceptional surface area (2630 m^2/g), electrical conductivity (6000 - 7200 S/m), mechanical properties (Young's modulus: $\sim$ 1 TPa; tensile strength: 130 GPa), and thermal conductivity (3000 - 5000 W/m K) [38]. The zero band-gap semiconductor properties of graphene is particularly significant in the field of electronics and optoelectronics. The absence of a band gap allows electrons in GN to move freely, exhibiting high electrical conductivity and exceptional electron mobility. This makes GN suitable for applications such as conductive coatings, sensors, and high-speed electronic devices. Despite its advantages, high surface area graphene sheets have a tendency to aggregate or stack together through π-π stacking and van der Waals interactions[2]. This aggregation is undesirable once the unique properties of graphene arise from its individual sheets. Moreover, it hinders the homogeneous dispersion of graphene within the polymer matrix when used as a nanofiller, leading to negative effects on the electrical and mechanical properties of the resulting polymer composite [37, 38].

Graphene Nanoplatelets (GNPs)

Graphene nanoplatelets are a type of graphene characterized by their platelet-like morphology. Each individual layer is only one atom thick, arranged in a hexagonal lattice structure. This nanomaterial is formed when a few layers of graphene (2 to 5 layers with thickness $\sim$ 5 nm) are grouped together during processing (often graphite intercalation). Just like graphene, GNPs have exceptional mechanical, electrical, and thermal properties. They have a high Young's modulus, typically ranging between 208 - 650 GPa, and a tensile strength of 130 GPa. The electrical conductivity of graphene nanoplatelets is on the order of 10^3 S/m [38]. Graphene nanoplatelets are frequently incorporated into polymer matrices to enhance their overall properties. The platelet structure of GNPs imparts several advantages compared to other carbon nanomaterials. These advantages include a relatively lower production cost, flexibility, and low sheet resistance, making GNPs suitable for applications in flexible electronics and strain sensors. Additionally, good potential for enhancing the thermal conductivity of polymer matrices, making them suitable as thermal interface materials [39]. However, the processing method might introduce waviness and wrinkles in the GNPs structure, which would eventually degrade the mechanical qualities of their polymer composites [38].

[2]The term "π-π" refers to the π bonds formed by the overlapping p-orbitals of the carbon atoms in adjacent layers. These π bonds interact with each other through a phenomenon called van der Waals forces.

Graphite Oxide (GO)

Graphite oxide is an oxidized form of graphite containing oxygenated functional groups such as hydroxyl, carboxyl, and epoxide. It is obtained by oxidizing graphite crystals by subjecting them to powerful acids and other oxidizing agents. The presence of functional groups containing oxygen facilitates the homogeneous dispersion of GO in both aqueous and organic solutions. This attribute proves advantageous during the preparation of polymer nanocomposites, as GO can be uniformly dispersed within the polymer matrix. Additionally, GO offers a cost-effective solution due to the affordability of graphite as a raw material. Another interesting characteristic of GO is that the presence of oxygen functional groups disrupts the sp^2 bonds, making it an electrical insulator. This characteristic makes GO an ideal nanofiller for enhancing some polymers' already good electrical insulation performance in applications such as cable and wiring insulation [37]. To restore and enhance its electrical conductivity, GO can undergo a reduction process, enabling the extraction of oxygen functional groups to synthesize reduced graphene oxide (rGO). Depending on the degree of reduction, different conductivity levels can be attained [40].

Carbon Nanotubes (CNTs)

The discovery in 1985 by Kroto *et al.* [41] of the third ordered allotrope of carbon, commonly referred to as buckyballs (C_{60} or fullerene), marked the beginning of a new era in the world of nanotechnology. This breakthrough opened the doors to the discovery of multi-walled carbon nanotubes in 1991 by the Japanese scientist Iijima [42] and, subsequently, the single-walled variant two years later by Iijima and Ichihashi [43] and Bethune *et al.* [44]. Since then, CNTs have been the subject of extensive research due to their unique properties. As the own name suggests, carbon nanotubes are lattice-like tubular structures composed of bounded carbon atoms arranged in a hexagonal network, closed with fullerene caps at the end of the tube. CNTs are considered one-dimensional nanomaterials with dimensions ranging from less than 1 to 50 nanometers radially and several micrometers axially. Based on both theoretical and experimental investigations, CNTs exhibit an intrinsic electrical conductivity that can reach up to 10^6 S/m, a high aspect ratio, i.e., the ratio of the length to the diameter, of 10^2 to 10^6, and a low density ranging from 1.3 to 2 g/cm^3. CNTs are also incredibly strong, reaching up to 150 GPa of tensile strength, roughly 200 times that of most aeronautical steel and aluminum grade alloys. Additionally, the Young's modulus of CNTs can be higher than 1 TPa, which is equivalent to the elastic modulus of diamond [45–48]. Due to their remarkable characteristics, CNTs have gained widespread use in high-performance engineering, notably in aerospace. For instance, they have been incorporated into thermoset polymeric matrices like epoxy, producing composites with outstanding heat resistance and improved specific strength. These epoxy/CNT nanocomposites have been applied in components like the wing-tip fairings of the Lockheed Martin F-35 and have played a crucial role in enhancing the performance of diverse aerospace systems, including Tomahawk missiles [37].

Carbon nanotubes are divided into three fundamental groups, separated based on the number of inner walls within the nanotube structure. The first of these are the single-walled carbon nanotubes (SWCNTs), which comprise a sheet of hexagonal lattice-shaped graphene rolled into a cylinder. Producing high-quality SWCNTs with precise structures is challenging and expensive. However, methods such as chemical vapor deposition (CVD) offer a more cost-effective, high-yield synthesis method for SWCNT while maintaining product purity. SWCNTs are prized for their flexibility and exceptional electrical conductivity, being typically used in electronic devices, sensors, and field transmitters. On the other hand, MWCNTs consist of a concentric arrangement of SWCNTs, i.e., multiple layers of graphene seamlessly rolled into a concentric tubular structure. Notably, the inter-layer spacing in MWCNTs is similar to the distance between layers in graphene, approximately 0.34 nm. Due to their larger diameter and multiple walls, MWCNTs are often used in applications requiring mechanical reinforcement and as additives in polymers, composites, and conductive materials. Additionally, they are easier and cheaper to produce in larger quantities through methods like chemical vapor deposition and arc discharge. Finally, the double-walled carbon nanotubes (DWCNTs), are a type of nanotube formed by two SWCNTs, where a smaller one is enclosed within a larger one. Much like MWCNTs, the two layers have an approximate 0.34 nm separation. Although DWCNTs share structural similarities with SWCNTs, they exhibit improved resistance against aggressive chemical exposure due to the protective outer wall [37, 38, 49].

The main properties of the three types of carbon nanotubes mentioned above are outlined in Table 2.6. It is important to note that these values can vary depending on factors like the synthesis process, testing method, and specific types of CNTs within each category. As such, these ranges intend to provide a general overview of their properties. Additionally, a schematic representation of SWCNTs, DWCNTs, and MWCNTs geometry can also be seen in Figure 2.6.

Table 2.6: Physical, mechanical, thermal, and electrical properties of the three types of carbon nanotubes [38, 49–51].

Properties	**Unit**	**SWCNT**	**DWCNT**	**MWCNT**
Typical Diameter	nm	0.5 - 2.5	1.5 - 3	10 - 100
Aspect Ratio	–	10^3 - 10^6	10^3 - 10^6	10^2 - 10^4
Density	g/cm^3	1.3 - 1.5	1.4 - 1.5	1.3 - 2
Surface area	m^2/g	500 - 1000	300 - 600	50 - 500
Tensile Strength	GPa	50 - 150	20 - 60	10 - 60
Young's Modulus	TPa	1 - 3	0.7 - 1.5	0.3 - 1
Thermal Conductivity	W/mK	3000 - 6000	2000 - 4000	2000 - 3000
Electrical Conductivity	S/m	10^6 - 10^7	10^6 - 10^7	10^5 - 10^6

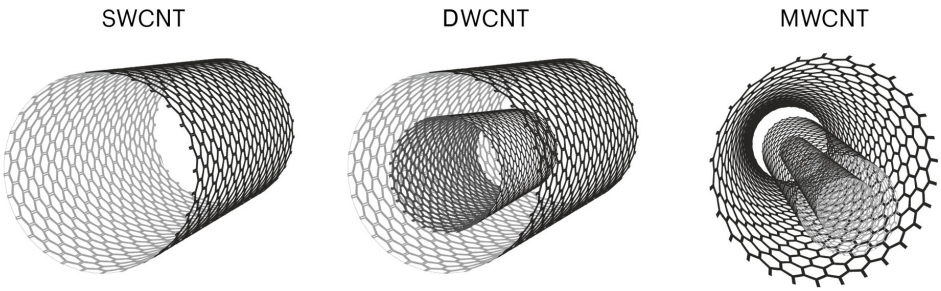

Figure 2.6: Schematic representation of a single-walled (left), double-walled (center), and a multi-walled (right) carbon nanotube, adapted from [52].

CNTs also have different microstructures, which refer to the arrangement of the carbon atoms in the lattice-like structure (chirality). The atomic structure of nanotubes can be described in terms of chiral vector: $\vec{C}_h = n\vec{a}_1 + m\vec{a}_2$, where the integers (n, m) are the number of steps along the zigzag carbon bonds of the hexagonal lattice and $\vec{a}_1$ and $\vec{a}_2$ are the lattice vectors. Another related parameter is the chiral angle, θ, given by the angle between $\vec{C}_h$ and $\vec{a}_1$. Varying the chiral indices (n, m), different microstructures are obtained. When $n = m$, the chiral angle is 30°, and an armchair nanotube is obtained. Nanotubes with $m = 0$ are known as zigzag tubes (θ = 0°), and for any other values of n and m the nanotubes are known as chiral. A schematic representation of the different CNTs chirality is depicted in Figure 2.7. Depending on chirality, carbon nanotubes can either be conducting or semiconducting. Armchair CNTs exhibit electrical characteristics similar to metals (conductors), whereas chiral and zigzag CNTs can be described as quasi-metallic or semiconductors. In the case of chiral and zigzag CNTs, they display quasi-metallic behavior with a finite band gap when the difference between n and m ($n - m$) is divisible by three and $n \neq m$. Otherwise, they act as moderate semiconductors under all other circumstances [46, 53].

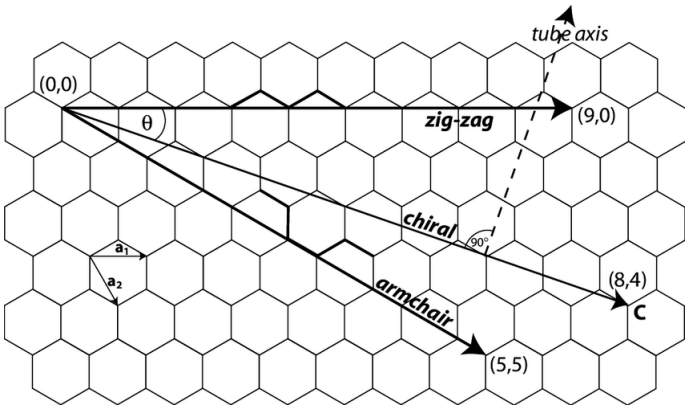

Figure 2.7: Schematic diagram of a bi-dimensional graphene sheet illustrating the chiral and lattice vectors as well as the chiral angle and respective microstructures, from [54].

2.2 Impact Damage in Laminated Composites

2.2.1 Introduction to Impact Damage

Aerospace composite structures are prone to in-service damage, which comprises normal wear and tear of the components (i.e., fatigue and degradation) and accidental damage (i.e., impact damage, lightning burns). The in-service damages are caused mainly by sudden impact damages that can severely reduce the composite mechanical performance [7].

Over the past few years, there has been a significant worry surrounding impact damage in laminated composites used for primary load-bearing structures. The reason for this heightened level of concern is that composite materials are highly vulnerable to impact, which has become a serious threat to composite structures because it causes significant internal damage like delamination, matrix cracking, and fiber breakage, while only leaving a slight indentation on the impacted surface. Such internal defects, which are not visible on a composite's surface, weaken the material's characteristics and decrease the composite structure's ability to support loads by more than 50% [55]. It is, therefore, necessary to have an in-depth knowledge of this domain to understand how a laminated composite structure behaves under an impact situation and how it affects its behavior and performance in service.

2.2.2 Classification of Impact

Composite materials are particularly sensitive to impacts because most of these events will occur in the transverse direction of the composite structure, which is susceptible to damage due to the absence of through-thickness reinforcement. As a result, composites will absorb the energy from the impact through fracture mechanics rather than elasticity and plasticity [56]. Generally, impact events are divided into three major categories: low-velocity, high-velocity, and hypervelocity impact. However, there is no apparent transition between them, and authors diverge on how to define each category [57].

According to Zukas *et al.* [58], low-velocity impact occurs for velocities below 250 m/s. In the range from 500 to 2000 m/s, the impact is considered high-velocity, and the structure's response becomes secondary in studying the material behavior in the impact area. Hypervelocity impact occurs for velocities greater than 2000 m/s, where the local pressures exceed the strength of the material, and the colliding solids can be treated as fluids in the initial impact phase. For velocities surpassing 12 km/s, the energy propagation occurs at such a high rate that vaporization of the materials occurs at the instant of collision.

Liu and Malvern [59] proposed a damage-based classification system for impacts. They noted that the impact can be determined by the type of damage incurred on the composite laminates, with a particular focus on the severity of the damage. High-velocity impacts are characterized by penetration-induced fiber breakage, while low-velocity impacts are characterized by delamination and matrix cracking. Sjöblom *et al.* [60] and Shivakumar *et al.* [61], reported that low-velocity impacts are defined as quasi-static events because the impact duration is significantly longer than the amount of time needed for the waves to propagate from the impact point to the supports or free edges. High-velocity impact response is dominated by stress wave propagation through the material. The structure does not have time to respond, which results in localized damage because the impact event ends before the stress waves have reached the structure's edge.

Abrate [62], in his review of impact on laminated composites, stated that low-velocity impacts occur for impactor speeds less than 100 m/s, and for hypervelocity impacts, speeds are greater than 1000 m/s. On the other hand, by considering the test methodologies commonly used in modeling the impact event (falling weight impact testing, Charpy, Izod, etc.), Cantwell and Morton [63] neatly categorized low velocity as up to 10 m/s. Robinson and Davies [64] stated that a low-velocity impact is one whose stress wave traverses the thickness of the material and does not play a significant role in the stress distribution, i.e., only causes small plastic deformations.

Hogg and Bibo [65] define low-velocity impact when it is in the range of 1 to 10 m/s. Impacts exceeding 100 m/s are classified as ballistic events, while those exceeding 1000 m/s are called hyper-velocity impacts. Davies and Olsson [66] classify low-velocity events, as the ones caused by dropped tools during manufacture or in-service repairs, in the range of 4 to 8 m/s with energies up to 50 J. Runway debris' impacts with velocities up to 70 m/s can be classified as intermediate-velocity impact, with again energies of approximately 50 J. The ballistic impact caused by weapons or missile fragments is categorized as high-velocity, ranging between 300 and 2500 m/s. The projectiles may only weigh a few grams, but their kinetic energy is in the range of 10 to 20 kJ. Ultimately, hypervelocity refers to satellites and spacecraft that could be hit by micrometeorites or space debris traveling at speeds between 30 to 70 km/s. In this case, as the impact lasts only a few nanoseconds, conventional heat transfer is impossible, and the impactor and the affected structure will vaporize.

2.2.3 Low-Velocity Impact (LVI)

From all the types of impact, low-velocity impacts are by far the most critical for aerospace laminated composite structures, as they are the most common and result in significant losses in the structure's strength and stability. Low-velocity impacts result from events such as bird strikes, ground maneuvers, and collisions during docking or tool drops, which inflict severe internal damages that are difficult to detect visually, commonly known as barely visible impact damage (BVID). As a result, impact damage to the composite structure may go unnoticed for extended periods before a catastrophic failure is reported [56]. In this regard, the present sub-section intends to address LVI in its various dimensions, giving more detailed information on aspects related to this topic.

2.2.3.1 Experimental Impact Test Methods

There are several different techniques for testing composites under low-velocity impact events. For LVI events, the usage of pendulums like the ones present in the Charpy and Izod test, as well as the drop weight impact test, have become standard. Herein, a description of these methods is presented to better understand how they work and what their advantages and limitations are for impact testing composite materials.

Charpy and Izod

The initial testing methods explored for impact testing of composites were derived from techniques already proven successful for other materials, such as metals and plastics. These methods involved the Izod and Charpy impact tests, in which a pendulum hammer is released from a standard height to hit a beam-shaped specimen (either notched or unnotched) with a specified kinetic energy. The Izod test (Figure 2.8a) consists of a beam clamped and hit as a cantilever, whereas in the Charpy test (Figure 2.8b) the beam is supported and loaded in bending by the pendulum striker. These tests aim to measure the energy required to break the specimen, thereby allowing a record of the material's strength under impact conditions [56, 65].

These two types of tests are beneficial for testing the isotropic materials for which they were initially developed. However, when it comes to composite materials, these methods have many shortcomings. Izod and Charpy methods do not consider the anisotropy and heterogeneity of composite materials and the complex failure mechanisms that can occur in composite structures under impact loading. The specimens used in these tests typically do not represent the complex geometries and stacking sequences found in actual composite structures, which can lead to inaccurate results. Though beam-based impact testing is useful for testing new materials in a laboratory environment, there are more reliable methods for predicting how thin composite structures will behave [65].

(a) (b)

Figure 2.8: Schematic arrangements for impact tests: (a) Izod; (b) Charpy, adapted from [67].

Drop-weight

Another type of LVI testing is drop-weight impact testing, which is the most common test for composite materials. In drop-weight impact testing, an impactor with a given mass, typically hemispherical, is raised to a known height and released, hitting the specimen (usually a plate) in a horizontal plane. The sample can be either simply supported or fixed. The choice can be made between either an instrumented or non-instrumented test machine, which usually has an anti-bounce system that prevents the impactor from impacting the specimen more than once. The impactor's velocity is measured using optical sensors placed just above the specimen. Figure 2.9 displays how an instrumented impact machine works, where $x(t)$ is the coordinate system, H is the drop height, W is the impactor weight, and v_0 is the impact velocity [68].

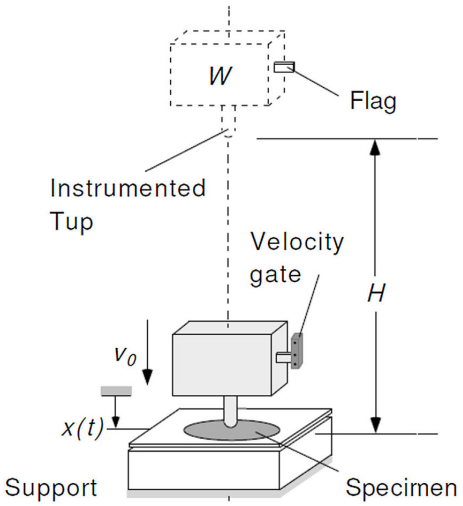

Figure 2.9: Illustration of a drop-weight impact test machine, from [68].

Drop-weight impact test in composite plates has many advantages, especially compared to the pendulum test methods. Drop-weight impact tests can simulate the LVI damage that occurs during real-life operations with better accuracy. It can also test a wide range of specimen geometries and vary the impactor's mass and geometry. This test is also quick, easy to perform, and versatile, allowing the study of clearly visible impact damage (CVID) and barely visible impact damage [68].

2.2.3.2 Failure Modes

The heterogeneous and anisotropic nature of laminated composites, along with multiple interactions between composite parts and the emergence of various forms of stresses and their redistribution, results in very complex failures within the composite structure. As such, LVI-related failures in laminates often occur in three main forms:

- Matrix cracking;
- Delamination;
- Fiber breakage.

These various damage modes generally occur combined upon the impact loading, as shown in Figure 2.10. Another type of failure, known as indentation, is also attributed to BVID as a result of a low-velocity impact. However, this form of damage has negligible influence on the stiffness and integrity of the structure and is frequently the sole indication of an impact [10, 56].

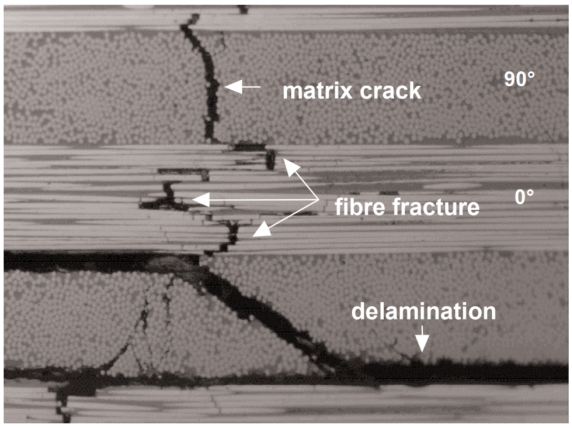

Figure 2.10: Types of damages in impacted fiber reinforced laminates, from [66].

Matrix Cracking

The first type of failure caused by low-velocity impact is matrix cracking, which results from the different properties that the constituents (fibers and matrix) exhibit and is typically oriented parallel to the direction of the fiber. Shear and bending (or transverse) cracks are the two primary forms of matrix cracks that appear in a composite structure due to LVI. Shear cracks are caused by high transverse shear loads and compressive bending strains, which incline roughly 45° relative to the impacted surface. On the other hand, bending cracks are induced by high bending stresses and are formed essentially along the vertical plane. For short thick laminates, stronger due to higher peak contact forces, transverse cracks appear under the impactor in the upper plies. In contrast, long thin laminates display bending cracks in the lower layers due to excessive transverse deflection, which once more causes matrix delaminations and cracks [10, 57].

Takeda *et al.* [69] led pioneering research on impacted glass/epoxy laminates using scanning electron micrography, being one of the first to study and report the interaction between matrix cracking and delamination. They observed that transverse cracks are perpendicular to the interfaces when there are no delaminations and tend to propagate in regions of high fiber concentration. In the presence of delaminations, cracks develop obliquely, which led the authors to conclude the relationship between cracking and delaminations. Sjöblom *et al.* [60] stated that cracks in the matrix alone do not dramatically affect the laminate's stiffness. Still, it does potentiate delaminations and fiber breakage, significantly affecting the composite structure's stiffness and impact response.

Delamination

The most hazardous type of structural damage happening at LVI is delamination. Delaminations form between the layers in the laminate and are primarily induced by interlaminar shear stresses, which are enhanced by matrix cracks and ply stiffness mismatch. As matrix cracks (shear and transverse) approach the matrix/reinforcement interface, they are affected by shear loads that cause delamination due to the stress concentration at their crack tips. Due to composite materials' low translaminar fracture propagation resistance, delamination may affect larger areas than the initial indentation. Delamination, as opposed to matrix cracks, can drastically lower a composite structure's compressive strength, which can have detrimental effects on the composite structure's ability to support loads [10, 66]. Liu [70] studied the damage characteristics of many laminated composites and found that delamination results from a mismatch in the bending stiffness of adjacent layers, i.e., from different fiber orientations between the layers. He discovered that when a laminate is impacted on its top surface, the delaminated area exhibits an oblong or "peanut" shape, with its primary axis oriented toward the lower ply's fibers at that interface. According to both experiments and analysis, the plate tends to bend concavely along the fiber orientation but bends convexly in the transverse direction, supporting his

claim that bending-induced stresses are the primary source of delamination. The greater the ply's mismatch (0/90 is the worst-case fiber orientation), the greater the delamination area.

Moreover, factors such as material properties, stacking sequence, and laminate thickness were also found to influence delamination propagation and initiation, as will be discussed later. According to Choi *et al.* [71], delamination only happens if there is a crack in the matrix and after a threshold energy has been reached, below which the energy is absorbed in the elastic regime of the laminate. On the other hand, Davies and Robinson [72] concluded that an initial flaw or crack size is not required for delamination growth. They formulated an equation to determine the critical load at which delamination propagation starts, which is proportional to $b^{3/2}$, where b is the laminate thickness and is independent of the delamination radius. This equation's predictions for the initiation of delamination proved to be in good agreement with the experimental findings.

Fiber Breakage

Fiber breakage usually occurs much later in the fracture process than matrix cracking and delamination. Under the impactor, fiber breakage happens due to local compressive and shear forces. In contrast, local fiber tensile breakage can be observed on the opposing face and in the proximity of significant matrix cracks [57, 59]. The center of the delaminated region typically has more extensive fiber failure, which is distributed fairly consistently across the thickness. Additionally, fiber failure in thin laminates typically impacts more plies and is more extensive than in thick laminates, demonstrating the significance of membrane stresses in the genesis of fiber breakage [73]. In composite materials, membrane stresses refer to the stresses that act within the plane of the composite material and are perpendicular to the normal direction of the plane. The studies by Siow and Shim [74] show that fiber breakage happens more frequently for woven fiber laminates than for cross-ply laminates. This is due to the interlacing of the fibers in woven fiber laminates, which causes kinks at the cross-over locations that produce stress concentrations. As a result, fibers in woven laminates fail more easily than those without kinks in cross-ply laminates. According to Wang *et al.* [75], the response of braided textile-reinforced composites to repeated low-velocity impacts varies according to the level of normalized impact energy. Initial micro-cracks occur in the yarns at low-impact energy, leading to delamination with a low-damage accumulation. At higher impact energy, matrix cracking is the first mode of damage, followed by rapid delamination propagation, resulting in the accumulation of damage, macro cracks, and fiber breakage.

2.2.3.3 Impact Response

An impact event is a complex process that initiates several wave phenomena over different time scales, as depicted in Figure 2.11. Upon impact, these waves can manifest in various forms such as [73]:

a) Fast tensile/compressive waves in the laminate's plane;

b) Fast surface waves along the surface of the laminate;

c) Slightly slower tensile/compressive waves through the laminate's thickness;

d) Transient shear and flexural waves that occur relatively slowly within the laminate;

e) A global quasi-static deflection mode in a slow oscillation.

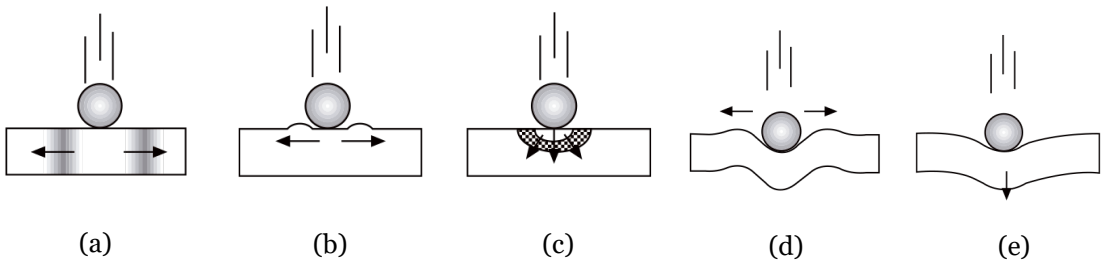

Figure 2.11: Impact wave phenomena and response types, from [73].

The wave phenomena observed during impact undergo reflection at boundaries and gradually dissipate due to scattering, elastic damping, and damage formation. The waves propagating through the laminate's thickness (as shown in Figure 2.11c) can cause significant damage due to their high amplitude and low strength direction. However, their impact is mostly localized to a specific area. Upon impact, the compressive waves in a laminate are reflected as tensile waves when they reach the free back surface of the material. This phenomenon can lead to local delamination due to composites' low transverse tensile strength. Nevertheless, the laminate can still bear the load until the compressive strength in the thickness direction is surpassed [73]. It can be demonstrated that the mass ratio of the impactor and the plate dictates the response type and impact duration. When the impactor has a small mass, the response is dominated by transient waves (types (a) to (d) in Figure 2.11). In contrast, the quasi-static response in Figure 2.11e is observed when the impactor has a large mass. For a square quasi-isotropic plate subjected to a central impact, impactors with a mass less than a quarter of the plate mass lead to a small mass impact response, while impactors with a mass greater than twice the plate mass result in a quasi-static impact response [73]. Further discussion and detailed information on mass criteria and the effect of plate geometry and orthotropy is given by Olsson [76].

The difference between small and large mass LVI is demonstrated in Figure 2.12, where the response and damage caused by a 10 J impact are compared for a large mass (1.5 kg) and a small mass (10 g) impactor. It is observed that the load, deflection, and strains have a similar phase relationship for the large mass impactor, whereas they are out of phase for the small mass impactor. Additionally, the small mass impactor leads to a higher peak load and greater delaminations, as depicted in Figure 2.12b and 2.12d, respectively. Consequently, these impacts usually result in more severe damage, as the plate exhibits a stiffer response and reaches the damage threshold load earlier, limiting its ability to absorb energy through elastic deformation. When a low-velocity large-mass impact occurs, the laminate deformation happens in an essentially static mode, as the impact duration is much larger than the time needed for the stress wave to reach the boundary. The load and deflection curves resulting from impacts by large masses show a bell-shaped trend and lead to a smaller area of delamination, as illustrated in Figure 2.12a and 2.12c, respectively [66, 73].

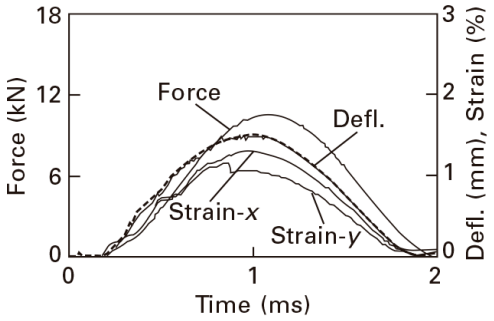

(a) Large mass impact response.

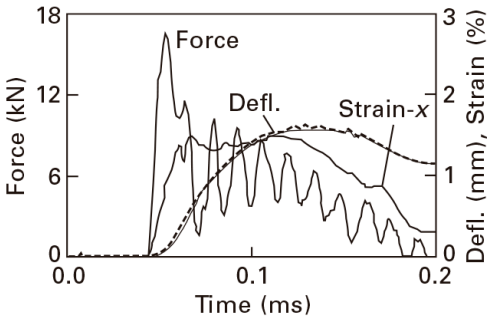

(b) Small mass impact response

(c) Large mass impact delamination area.

(d) Small mass impact delamination area.

Figure 2.12: Response and delaminations due to 10 J impact by a large and small mass impactor, from [66].

2.2.3.4 Parameters Affecting Impact Damage

Knowing the impact energy is not enough to predict the effect of an LVI on a laminated composite, once the extent and severity of the impact damage are influenced by various factors, such as the material properties, laminate thickness, stacking sequence, and impactor characteristics. In this section, the main factors that influence impact damage in laminated composites will be discussed, focusing on research findings and their implications for designing and optimizing composite structures.

Impactor Characteristics

Impact damage is significantly influenced by the shape and weight of the impactor. Generally, the most used impactor shape is hemispherical. However, in a real-life scenario, such as a dropped tool during maintenance, the shape of the tool hitting a composite panel may not be necessarily blunt, like a hemisphere. In this regard, some researchers have also studied other impactor shapes under LVI conditions. Mitrevski *et al.* [77] conducted a study to determine the effect of different shapes of impactors, namely hemispherical, ogival, and conical, shown in Figure 2.13. A drop weight test rig impacted samples of thin woven carbon/epoxy laminates at initial impact energies of 4 J and 6 J. The results showed that the conical impactor caused the specimens to absorb the most energy and resulted in the largest penetration depth. Only the hemispherical impactor produced BVID on the specimens impacted at an initial impact energy of 4 J, whereas the other impactor shapes produced permanent indentation and penetration. On the other hand, the hemispherical impactor produced the highest peak force but had the shortest contact duration. The damage threshold load was found to be the highest for the hemispherical impactor, followed by the ogival and conical impactors, respectively. Siow and Shim [74] showed that, aside from impactor mass or impact velocity, the delamination area is also dependent on the radius of curvature of the impactor tip. An impactor with a small nose radius (sharp) causes more impact-induced delamination than one with a large nose radius (blunt), as well as more fiber breakage.

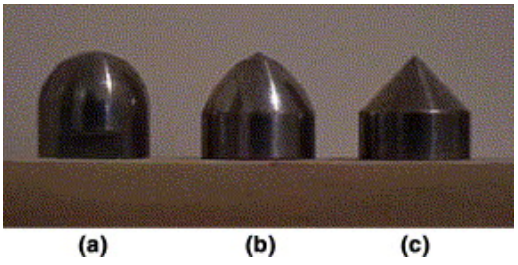

Figure 2.13: Impactor shapes: (a) hemispherical; (b) ogival; (c) conical, all 12 mm in diameter, from [77].

Material Properties

The fiber and matrix materials in a laminated composite have distinct properties, and these properties can also differ between individual layers within the laminated structure due to varying fiber orientations. As a result, the composite laminate may experience nonuniform stress distribution under load. Consequently, the strength of a composite is influenced not only by the strengths of its constituents but also by the extent of material property mismatch. Liu [70] studied the damage characteristics of epoxy-based laminated composites using glass, Kevlar®, and carbon fibers, subjected to LVI using a drop weight test machine. His investigation stated that a higher mismatch coefficient is found in composites with a higher difference between Young's modulus in fiber and matrix directions. In this regard, carbon/epoxy has the highest mismatching coefficient, followed by Kevlar®/epoxy, and lastly, glass/epoxy. Thus, carbon/epoxy is expected to have the highest delamination area among these three materials, whereas glass/epoxy is expected to have the smallest delamination area if the impacting energy and bonding strength are similar. However, according to the experimental results, Kevlar®/epoxy showed higher delamination areas than carbon/epoxy, while glass/epoxy had the smallest area. This fact is considered to be caused by the low inter-laminar strength at the Kevlar®/epoxy plate interface, i.e., the delamination resistance is drastically reduced by the weak connection between Kevlar and epoxy. In the work carried out by Naglis and d'Almeida [78], the absorbed energy under Charpy impact of epoxy matrix composites reinforced by unidirectional glass, carbon, and aramid fibers is analyzed. The total absorbed energy showed an inversely proportional correlation to the elastic modulus of the fibers used as reinforcement. Fiber breakage is found in carbon/epoxy composites, as they fail in a brittle manner since they have a very limited plastic deformation capacity. As for the aramid/epoxy and glass/epoxy composites, delamination was the primary failure mode, explaining the higher absorbed energy by these composites.

Vieille *et al.* [79] studied the effect of using thermoset and thermoplastic polymeric matrices on the response of a laminate subjected to LVI. In this study, epoxy, PPS (Polyphenylene Sulfide), and PEEK (Polyether Ether Ketone) based carbon woven-ply laminates were compared, showing that epoxy-based laminates experienced larger delamination than the thermoplastic-based laminates. Carbon/thermoplastic laminates are characterized by reduced damages, especially carbon/PPS laminates, supporting the idea that a stronger matrix may be associated with enhanced impact performances. Additionally, the reinforcement weave structure also prevents substantial growth of delamination, but fiber breakages are more frequent and manifest at lower impact energy due to fiber crimps. When subjected to low-velocity impacts, carbon/epoxy is more prone to delamination due to the brittle nature of the epoxy resin. On the other hand, PPS-based laminates exhibit limited delamination, while PEEK-based specimens exhibit an increasing tendency to delaminate at increasing impact energy. Overall, the thermoplastic matrices increased the laminate impact strength, although they lower thermal stability, decrease chemical resistance, and promote worse fiber/matrix adhesion.

An additional way to reduce the impact damage area in advanced composite laminates is the introduction of CNTs. Kostoupolus *et al.* [80] investigated the influence of MWCNTs on the behavior of carbon fiber-reinforced polymer laminates during and after low-energy impact. After adding 0.5 wt% of MWCNTs to an epoxy resin, they compared the modified CFRPs to unmodified ones using a drop weight tower. The experimental results showed that, up to a specific energy level, there was no significant difference between the neat and modified specimens when directly comparing the delamination area or the absorbed energy per unit delamination area. The MWCNTs appear to have a more substantial reinforcing effect at impact energies above 16 J. Additionally, all MWCNT-doped specimens exhibited improved strength and effective compressive modulus after impact compared to the neat resin. Wang et al. [81] investigated the impact properties of pre-stretched GFRP composites enhanced different MWCNTs concentrations (0, 0.4, and 0.75 wt%). Compared to the control GFRP samples, those modified with MWCNTs exhibited improved impact resistance under impact energies of 9, 16, and 22 J. This enhancement was evident in the reduced damage factor and an increased perforation threshold. Microscopic fractographic analysis revealed that including MWCNTs in the epoxy matrix introduced additional mechanisms involving carbon nanotubes' breakage, bridging, and pull-out. These mechanisms contributed to improved load transfer, prevented crack propagation, and thereby dissipated more energy. In another study led by Ashrafi *et al.* [82], it was discovered that adding 0.1 wt% of SWCNTs led to a 5% decrease in the impact damage area, indicating that the impact was more confined to a specific location. This finding suggests that SWCNTs are more effective than MWCNTs, possibly because of their superior mechanical properties compared to multi-walled ones, even though SWCNTs revealed to be more difficult to disperse in the polymer matrix.

Laminate Thickness and Stacking Sequence

The stiffness of a laminated composite is greatly influenced by its thickness. The stiffness in the thickness direction significantly affects the maximum contact force, which in turn affects the amount of damage induced. Caprino *et al.* [83], using an instrumented drop-weight test machine, carried low-velocity impact tests on woven carbon/epoxy laminates of various thicknesses. The influence of material thickness on the main factors involved in the impact phenomenon was assessed from the force-displacement curves obtained during impact. The maximum force and related energy, the penetration energy, and the force and absorbed energy required for delamination initiation were all assessed. According to the experimental findings, all of these values increased to a power of about 1.5 with increasing plate thickness, except for the energy absorbed at the point of delamination initiation. If the displacement remains constant and the contact force is scaled by a power law of 1.5, the dynamic force/displacement curves of specimens with varying thicknesses converge to a single curve. This demonstrates why the maximum contact force, the correlated energy, and the penetration energy follow the same power law.

Zhou *et al.* [84] also focused on the thickness effect when numerically studying composite laminates' dynamic mechanical response and damage mechanism subjected to single and repeated low-velocity impacts. The impact-response parameters varied linearly with thickness, and under the same impact condition, thinner laminates mostly exhibit intralaminar damage mode, whereas the thicker plates absorb energy mainly through delamination.

The stacking sequence also plays a significant role in the impact resistance of laminates. For two plates with the same thickness but with different stacking sequences, the one with the higher differences in the angle between two adjacent plies will experience higher delamination areas. Amaro *et al.* [85] studied the influence of laminate stacking sequence on the residual strength of carbon/epoxy laminates after low-velocity impact. Using a drop weight testing machine, experimental tests were conducted on symmetric $[0,90,0,90]_{2s}$ and anti-symmetric $[0,90]_8$ laminates under 1.5, 2, 2.5, and 3 J impact energies. The $[0,90]_8$ laminates have smaller defects than $[0,90,0,90]_{2s}$ laminates for impact energies up to 2.5 J. However, for impact energies greater than 2.5 J, the $[0,90]_8$ laminates suffer from larger damages. As the impact energy increases, the residual strength decreases, and for samples impacted with 3 J, the reduction compared to non-impacted samples is about 34% for symmetric laminates and 78% for anti-symmetric laminates. The lower flexural stiffness of the anti-symmetric lay-up compared to the symmetric one is the reason for these significant differences between the two laminates regarding residual flexural strength.

Sevkat *et al.* [86] studied the effects of hybridization and staking sequence on the repeated drop-weight impact responses of hybrid plain-woven composites. Hybridization was found to be able to slow down damage accumulations. Additionally, it was observed that the stacking sequence of a hybrid composite significantly impacted the rate at which damage accumulated. Although the amount of glass and carbon fibers used to reinforce both hybrid composites was the same, the hybrid glass/carbon/glass composite withstood twice as many impacts as the hybrid carbon/glass/carbon composite. It can be concluded that damage evolution can be delayed by employing tougher material for the skin layers.

2.3 Structural Health Monitoring of CNT-FRPs

2.3.1 Introduction to SHM

As seen in the previous section, low-velocity impact represents a serious threat to laminated composites, not only due to the various types of damages it inflicts to the composite structure but also because the assessment of LVI damage is quite challenging, as it results in mostly ”invisible” or barely visible impact damages (BVID). Various NDT methods currently serve to assess damage evaluation in a composite structure. However, these are not able to detail the beginning or development of damage between inspection periods and are often very slow and require pulling the aircraft out of service, resulting in a time and resource-consuming task [7]. As a result, new methods, such as film sensors (e.g., bucky paper) and fiber optic sensors, have been employed to detect in-service damage in FRP composites. However, most of these embedded sensors are fragile and have poor adhesion bonding to the host structure, with the aggravation of having no structural contribution to the composite, which, in some situations, may even reduce the composite mechanical performance by creating pre-cracks in the matrix. Other suggested solutions involved using the composite's fiber as the sensor itself. However, this is limited to conductive fiber composites (e.g., CFRP), and damage detection is confined to the fibers that usually fail much later in the damage process, letting important damages, such as delaminations and matrix cracks, go unnoticed [13, 14]. Thereafter, the development of a novel, non-destructive SHM technique is of paramount importance to sense and diagnose damage in FRP composites at the point of impact or failure. Consequently, the SHM paradigm has been shifting towards the nanotechnology field, which seats at the forefront of this matter, as it allows the possibility of creating self-sensing composites by adding conductive nanoparticles as multifunctional sensors to the composite structure, capable of continuously monitoring the structural health of the composite

With the increasing application of CNTs in polymer composite materials, combined with their unique set of electrical and physical properties, it was only a matter of time before CNTs arose as a lead candidate to modify FRPs into multifunctional materials with structural and self-sensing properties. The idea of incorporating CNTs into FRPs for SHM purposes was first introduced by Fiedler *et al.* in 2004 [87]. Since then, numerous investigations and approaches have been suggested to examine the potential of using CNTs as piezoresistive sensors for structural health monitoring of FRPs. Hence, the following section will be dedicated to covering the fundamentals behind the electrical behavior and piezoresistive response of CNT-filled polymers, followed by the presentation of prominent studies that demonstrate the applications of CNTs for structural health monitoring in FRPs.

2.3.2 Piezoresistive Behavior of CNT-Filled Polymer Composites

2.3.2.1 Theory of Static Percolation

Piezoresistivity is an electro-mechanical phenomenon defined by the correlation between a mechanical stimulus, such as strain or stress, and a corresponding change in electrical resistance. Unlike piezoelectricity, which operates bidirectionally, converting a mechanical stimulus into electrical potential and vice versa, piezoresistivity exclusively results in a change in electrical resistance and functions solely in the mechanical-to-electrical direction [88]. As previously mentioned, electrical conductivity in nanocomposites is achieved by introducing conductive fillers within the matrix. In these materials, given that the matrix is electrically insulating, the mechanism enabling the flow of electrical current is the creation of a network comprising conductive fillers. No conductive pathways are formed at low filler concentrations, leading to an electrical insulating response. When the first conductive pathway forms throughout the material, there is a sudden decrease in resistivity, as depicted in Figure 2.14, and an insulator-to-conductor transition occurs. This significant transition is known as the percolation threshold [89]. There is significant variation in the percolation threshold among different CNT/polymer composite systems. In the literature, percolation thresholds ranging from as low as 0.0025 wt% [90] to as high as 15 wt% [91] have been reported. This variability is attributed to various chemical, physical, and geometrical factors, including the type of CNT, synthesis method, surface treatment, polymer type, and dispersion procedure.

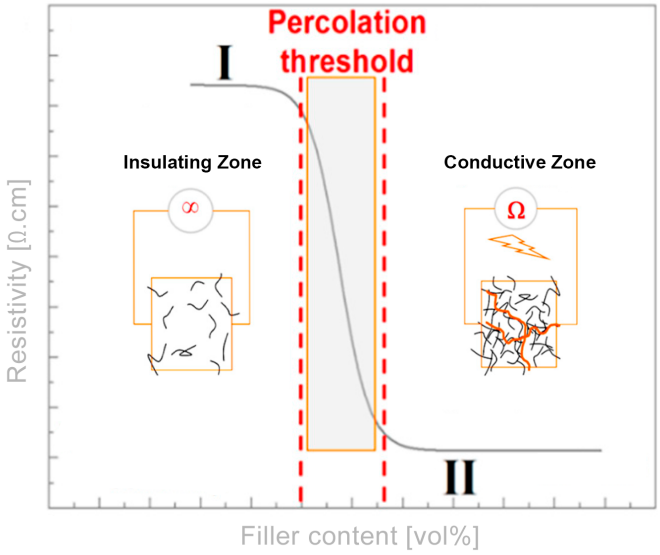

Figure 2.14: Resistivity of CNT-reinforced composites as a function of filler content and a schematic of the percolation threshold. Region I: fillers are dispersed without any conductive pathway (almost infinite resistivity). Central zone: insulator-to-conductor transition (first conductive paths are formed). Region II: dispersion of fillers in a matrix with an electrically conductive network (low electrical resistance), adapted from [89].

Regarding the use of CNTs for piezoresistive applications in polymer composites, the vast majority is dedicated to thermosetting matrices. Epoxy is by far the thermosetting matrix that has captured more attention of the scientific community, especially when compared to other thermosetting polymers such as vinyl ester or polyester [25]. One of the key advantages of epoxy resins is their low processing viscosity, which allows for better dispersion of CNTs in the epoxy matrix, resulting in improved composite properties. Additionally, epoxy resins can achieve electrical percolation at significantly lower CNT contents than thermoplastics or elastomers, making them particularly attractive for further developments of self-sensing composite materials [88].

Bauhofer and Kovacs [92] investigated the electrical behavior of epoxy CNT-composites and concluded that the processing parameters strongly influence the percolation threshold. For example, regarding the effect of the stirring rate, they concluded that after 5 min of stirring at 50 and 2000 rpm, a percolation threshold value of 0.01 and 0.1 wt% of CNT, respectively, was achieved. According to the authors, increasing the stirring rate improved CNT dispersion in the matrix, which reduced the number of accessible conductive paths. An identical electrically conductive behavior was also observed above the percolation threshold, regardless of the processing parameters.

Gojny *et al.* [93] compared the electrical behavior of epoxy-based CNT composites for CNTs with varying numbers of layers (SWCNTs, DWCNTs, MWCNTs). The study revealed that the number of walls in the CNTs did not significantly impact the composite's electrical properties when considering an equivalent mass of nanotubes. However, an increase in the number of walls resulted in higher CNT density, and as a result, MWCNTs exhibited the lowest percolation threshold value, approximately 0.05 vol.%. The researchers also noted that the lower specific surface area of MWCNTs, compared to SWCNTs and DWCNTs, reduced their attraction and agglomeration, leading to a better dispersion state, especially for MWCNTs without functionalization. With respect to this last parameter, it was observed that although functionalization can aid in the dispersion of CNTs within the matrix, it can also modify their structure, potentially decreasing their length and inherent conductivity, thereby increasing the percolation threshold.

Another parameter affecting the percolation threshold in epoxy-based composites is the CNT length. Bai and Allaoui [94] investigated this parameter while keeping the CNT diameter constant and observed a reduction in the percolation threshold from 2 to 0.5 wt% as the length of the CNTs increased from 10 μm to 50 μm. They concluded that a higher aspect ratio of the CNTs improved the occurrence of contact between nanotubes, resulting in increased conductivity of the composite. In this particular case, an increase from 10^{-11} to 10^{-5} S/cm at 1 wt% for 10 and 50 μm, respectively.

2.3.2.2 Piezoresistive Sensitivity

A fundamental parameter to evaluate the piezoresistive capabilities of a self-sensing composite material is the gauge factor (GF). Essentially, the GF quantifies the accuracy or sensitivity of a piezoresistive material to the change of resistance upon deformation. The higher the GF value, the more sensitive to resistance changes will the material be [89]. This parameter represents the slope of the linear correlation between the normalized change in electrical resistance and the applied strain, which can be calculated using Equation 2.1:

$$GF = \frac{R - R_0}{R_0}\frac{1}{\varepsilon} = \frac{\Delta R/R_0}{\varepsilon} \quad (2.1)$$

where $\Delta R/R_0$ is the normalized electrical resistance change, R_0 is the initial electrical resistance at rest ($\varepsilon = 0$), and R is the electrical resistance for the respective strain (ε).

In conventional metallic strain gauges used for materials testing, gauge factors typically fall within the range of 2.1 to 2.3. In contrast, carbon nanostructures exhibit inherently high piezoresistivity. For instance, individual SWCNTs have been reported to exhibit an extraordinarily high GF of up to 2900 [95]. This value is at least two orders of magnitude greater than the sensitivity observed when such nanotubes are incorporated into polymer composites. This discrepancy suggests that the complete piezoresistive properties of carbon nanotubes are not effectively transferred to their polymer nanocomposites. One reason for this is that the applied strain does not fully transmit to the filler material. Consequently, in such nanocomposites, the inherent piezoresistivity of the CNTs and the alterations in their dimensions under load only make a minor contribution to the overall measured piezoresistivity [96].

Figure 2.15 provides an overview of gauge factor values reported in various studies involving polymer composites filled with both SWCNTs and MWCNTs[3]. Buckypaper (BP) data is additionally incorporated for comprehensiveness. As depicted in Figure 2.15, the majority of gauge factors for CNT polymer composites fall within the range of 1 to 7, without a notably distinct trend between SWCNTs and MWCNTs. Worth noting that composites with MWCNTs appear to be more frequently reported, likely due to their ease of synthesis on a large scale, making them a more economical choice [50,88]. It's also evident that the majority of piezoresistive research focuses on tensile loading, while compression and flexural loading receive significantly less attention. In this context, tensile tests are not only more extensively studied but also yield higher values of GF [97–99], whereas bending tests typically result in lower GF values [100].

[3]The detailed data underlying this plot can be consulted in the Appendix A of Avilés *et al.* [88].

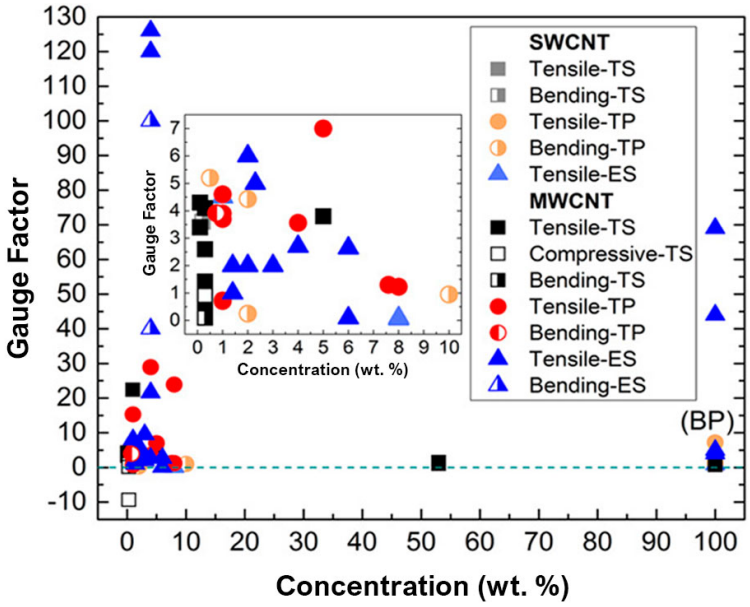

Figure 2.15: Overview of reported gauge factors for polymer composites containing SWCNTs and MWCNTs, adapted from [88].

It is worth noting that, for CNT-filled polymer composites, the piezoresistive sensitivity is higher just above the electrical percolation threshold. In contrast, composites with high filler content exhibit high conductivity and tend to be less sensitive to electrical resistance changes. This distinction arises because composites with a high filler content, characterized by many conductive pathways, experience minimal change in effective electrical resistance when their conductive paths are disrupted upon loading. On the other hand, working very close to the electrical percolation threshold, while maximizing sensitivity, can introduce a noisy electrical signal and pose practical challenges in instrumentation. As such, to overcome this practical constraint, most piezoresistive research on polymer composites opts for filler concentrations well above the percolation threshold, where electrical resistances within the range of kΩ to MΩ are typically achieved and more easily handled [88].

Regarding piezoresistivity, CNT thermosetting composites with low ultimate tensile strains typically exhibit linear piezoresistivity during loading. However, in some cases with relatively high ultimate strains, non-linear and non-monotonic piezoresistivity can occur. This can involve a shift from positive to negative piezoresistive behavior for specific CNT weight concentrations under significant deformations. This phenomenon is likely due to the inelastic behavior of the polymer matrix, resulting in a reduced effective distance between CNTs as the polymer undergoes axial stretching. Various factors, including matrix plasticity, lateral CNT motion due to the Poisson's effect, and three-dimensional rearrangement of the CNT network, may contribute to this negative piezoresistive effect under large strains [98].

2.3.2.3 Contact and Tunneling Resistance

In polymer composites with relatively low filler contents, the piezoresistive effect depends on the changes to the way the filler particles are arranged when the composite is mechanically loaded. It becomes evident that any deformation or strain in the conductive network influences the electrical resistance of the composite. The main mechanisms that affect electrical resistance under load are depicted in Figure 2.16, and can be divided into three main groups:

i. Reconstruction of the conductive network: involves the creation and destruction of conductive pathways between CNTs.

ii. Changes in the contact resistance between conductive fillers: related to CNTs moving closer together or further apart.

iii. Changes in the filler-to-filler interparticle distance: associated with tunneling resistance which also affects the electrical resistance of the composite.

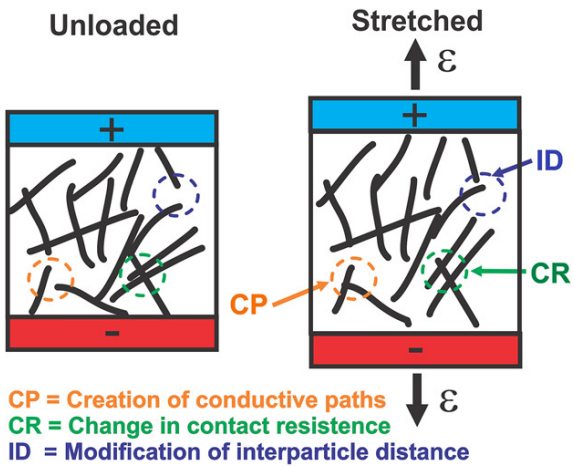

Figure 2.16: Piezoresistive mechanisms in polymer composites filled with carbon nanotubes, from [88].

Besides the significant influence associated with direct contacts between CNTs to the overall electrical resistance of the material, a phenomenon introduced earlier is also crucial for the flow of electric charge in polymer nanocomposites, which is known as tunneling effect, schematically represented in Figure 2.17. Compared to the contact mechanism, where the nanofillers make direct interactions and create a conducting network, the tunneling phenomenon allows electrons to cross the thin insulating layer between adjacent CNTs. Typically, in nanocomposites with very low filler contents, electron tunneling is a significant conducting phenomenon. However, it should be noted that an adequate amount of conducting fillers is necessary to guarantee that the gaps between adjacent particles are sufficiently small to support electron tunneling [101, 102].

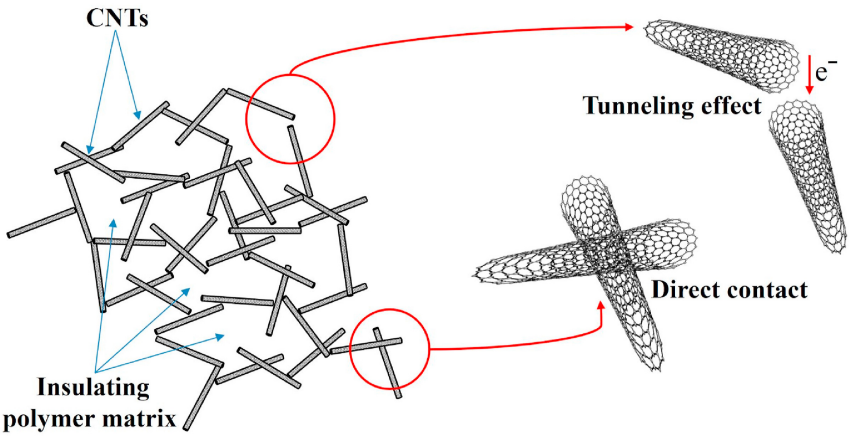

Figure 2.17: Schematic representation of the direct contact and tunneling effect in a CNT-filled polymer nanocomposite, from [89].

The extent to which the mechanisms showed in Figure 2.16 influence the effective piezoresistivity of the composite material depends on several factors, including mechanical and rheological characteristics of the polymer matrix, interactions between CNTs, morphology and waviness of CNTs, state of dispersion, tendencies for agglomeration, CNTs intrinsic piezoresistivity, matrix electrical permittivity, filler-matrix interaction, and loading conditions [88].

Finally, it is paramount to emphasize that not all changes in a composite's electrical resistance should be classified as piezoresistivity. The core criterion for piezoresistivity is that shifts in electrical resistance are initiated by changes in strain or stress within the material. While numerous other phenomena may lead to variations in the effective electrical resistance of CNT-filled polymer composites, such as matrix cracking, delamination, or even fluctuations in moisture or temperature, these occurrences, while noteworthy, should not be labeled as piezoresistivity. This distinction arises because, in these cases, the electrical resistance changes are not directly triggered by changes in strain or stress but rather by another physical parameter [88].

2.3.3 CNTs as Damage Sensors in FRPs

It has been proven that matrix-dominated damages, such as matrix cracking and delamination, are the starting point of several FRP failure modes, which tend to occur before the end of the laminate's lifetime when most severe failure modes like fiber breakage tend to occur. Researches show that the incorporation of a small fraction of CNTs into an insulating matrix results in the creation of a sensory network within the FRP structure. This network can detect the emergence and spread of microcracks by electrical resistance change (ERC), making it a promising piezoresistive sensor for the structural health monitoring of composite structures subjected to various types of mechanical loads.

Thostenson and Chou [103], studied electrically conductive networks composed of 0.5 wt% of MWCNTs dispersed in an epoxy matrix as *in situ* sensors for damage detection and accumulation during cyclic tensile loading of GFRPs. The nanotubes were initially hand-mixed to incorporate into the resin, and the mixture was then fed into a three-roll mill. After calendering, the epoxy with MWCNTs was mixed with a curing agent and placed in a vacuum oven for degassing. Cross-ply laminates $[0/90]_s$ were manufactured by stacking four layers of unidirectional GF mats. A conventional VARTM (vacuum-assisted resin transfer molding) technique was implemented to produce the MWCNT-enhanced GFRP composites. Figure 2.18 shows the resistance response of a specimen undergoing tensile cyclic loading before failing after the sixth load cycle. According to the authors, the relatively large difference in deformation between each cycle highlights the accumulation of damage and gives insight into the mechanism of resistance change. In the first two loading cycles, the applied strain was below the level at which micro-cracking initiates in the 90° plies. Consequently, a change in resistance that closely tracks the applied strain is seen. In the following cycles, as the strain increased, cracks began to appear, and the resistance visibly began to vary from the strain response, leaving a residual resistance change after unloading, as seen in Figure 2.18a. Three types of sensing signals were obtained for each incremental strain applied, as depicted in the magnified view of the fifth loading/unloading cycle shown in Figure 2.18b. When cracks appear in the transverse plies, the longitudinal plies remain elastic, and the cracks close when the load is removed. In the fourth cycle, some electrical contacts break irreversibly, but others reform when the crack closes. During the initial loading stages of the fifth cycle, the previously formed cracks re-open with increased strain. This results in a steeper slope of the resistance curve. However, as all previously formed cracks open, the slope of the curve decreases, corresponding to the piezoresistive elastic deformation. From here, damage accumulation is highlighted by sharp leaps in resistance beyond the linear region of increased slope. Overall, the results show that understanding the development and damage accumulation can be achieved by integrating real-time load and strain measurements with the CNT network's electrical resistance measurements.

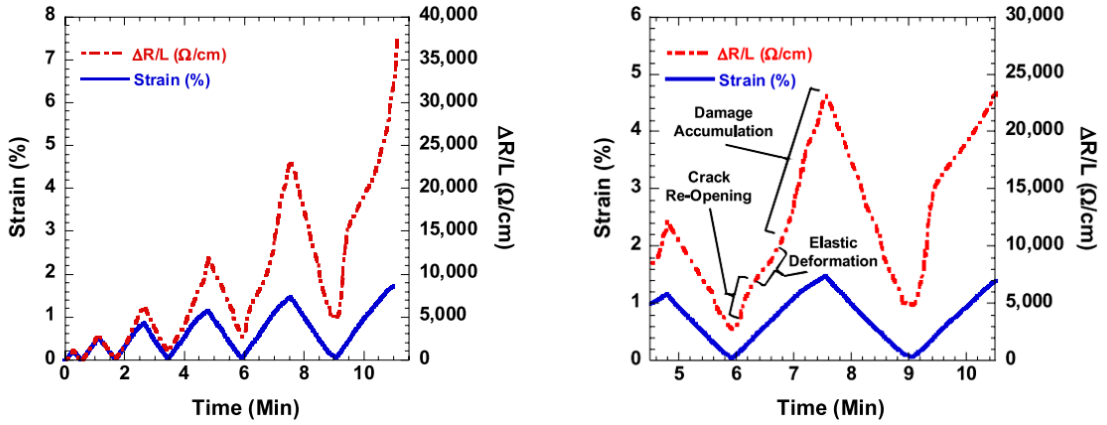

Figure 2.18: Resistance response of a cross-ply laminated composite undergoing cyclic tensile loading: (a) transient strain and resistance response under increasing cyclic loading up to failure; (b) magnified view of the fifth loading cycle resistance response, from [103]

Kostopoulos *et al.* [104] studied the influence of adding MWCNTs to the epoxy matrix of carbon fiber reinforced composites to enhance the real-time damage monitoring via the ERC method under monotonic and cyclic tensile tests. Three different contents of nanotubes were added to the matrix (0.1, 0.5, 1.0 wt%) using a torus-mill device, and sixteen plies of unidirectional CF were used as reinforcement. Electrical resistance measurements were performed through the four-probe method, based on a two-electrode/four-wire configuration. A direct comparison of the electromechanical behavior of the CNT doped CFRP laminates with the control laminates showed that higher resistance changes ($\Delta R/R_0$) were recorded for the doped CFRP laminates and increased with increasing MWCNT content. At low strains, ranging from 0 to approximately 0.2 %, resistance changes are nearly insignificant for laminates containing MWCNTs contents up to 0.5 wt%, and are slightly evident for those with 1 wt%. When strains surpass 0.2% and up until ultimate fracture, significant resistance changes are recorded in the MWCNT-doped laminates, whereas the undoped ones display a non-uniform pattern. During the cyclic tensile tests, a residual resistance change was detected upon unloading, increasing at each consecutive cycle's end. This residual change was linked to matrix-related irreversible damage events, which became more pronounced with higher MWCNT content. The results showed that the presence of the carbon nanotubes within the polymer matrix substantially increased the composites' electrical conductivity in the transverse and through-thickness directions and increased the sensitivity to damage by making resistance variations more obvious. On the other hand, electrical resistance changes for the control CFRP laminates reflected only damages associated with the reinforcing phase, i.e., the carbon fibers, lacking detection of matrix-related damages. The authors concluded that the embedded MWCNTs create a more sensitive neuron-like percolated network between the CF layers, improving the CFRP composite's overall sensing capabilities.

Monti *et al.* [105] employed various MWCNTs contents (0.1 to 0.5 wt%) in the epoxy matrix of a GFRP composite and studied the relationship between impact damage and resistance change of the material. The laminates were manufactured via vacuum infusion technique and had a symmetric stacking sequence of eight layers, comprising six woven rovings and two mats plies. The nanotubes were disaggregated using a high-speed mechanical stirrer, and then the mixture was subjected to an ultrasound bath to degas and enhance dispersion homogeneity. An impact energy of 11.7 J was used throughout the experiment, and the impact tests were carried out using a self-made pendulum. Furthermore, a two-probe technique was chosen to measure the trough thickness electrical resistance, consisting of four electrodes located on the top and rear surface of the sample and diametrically opposed in couples. Electrical characterization of the nanocomposites demonstrated the electrical resistivity variation with MWCNT concentration. Figure 2.19 shows the results of this procedure, where a sharp drop in the resistivity is visible even at a CNT content of 0.1 wt%, passing from 10^{16} to 10^{8} Ω.cm, demonstrating the key role that carbon nanotubes play in enhancing the electrical properties of polymers. It was further observed that the 0.5 wt% content of MWCNTs created an extremely high viscosity mixture, making it completely impractical to manufacture. Therefore, the 0.25 wt% concentration was chosen to manufacture the nano-enhanced GFRP composites. Experimental results have shown that the electrical resistance after the low-velocity impact had increased by about 7.7 % comparatively with the non-impacted sample, showing that it is possible to associate the increase in electrical resistance of the composite with the formation of damages caused by impact. Additionally, post-impact tensile tests showed significant drops in the mechanical properties, particularly tensile strength, with a 50 % decrease. Moreover, cross-section cuts of the impacted composites showed several fracture modes, including fiber pull-out at the bottom surface, as well as intra-laminar cracks and delaminations.

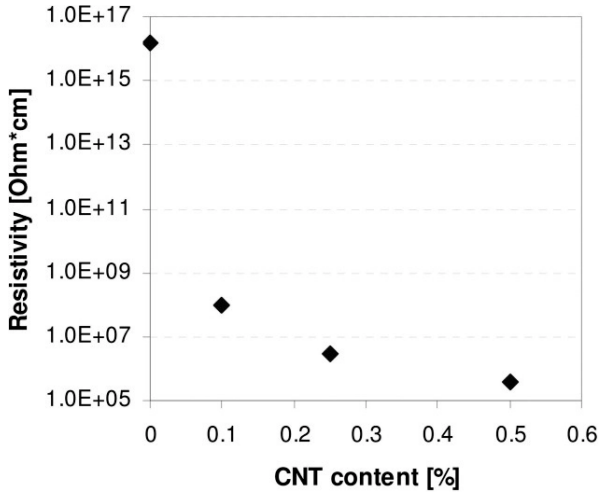

Figure 2.19: Nanocomposites electrical resistivity as a function of CNT content, from [105].

Gao *et al.* [106] monitored how CNT-reinforced GFRP composites were affected by impact damage by measuring the electrical resistance of the conductive network. The researchers used the VARTM technique to infuse the epoxy and a liquid sizing agent containing CNTs in six layers of plain woven glass fiber. Impact tests were performed on a drop-weight impact testing machine with a spherical loading nose, and the impact energy was approximately 70 J for each impact. During the impact, trough-thickness electrical measurements were performed using a two-point technique, applying extended electrodes at opposing edges of the specimen. A comparative analysis of the two and four-probe techniques showed that, given the inherent characteristics of specimens, the electrical contact resistance is minimal when compared to the overall specimen resistance, generally falling below 1 % in relation to the total resistance of the composite. According to the experimental findings, the resistance change consistently increases with repeated impact loadings, resulting in a permanent resistance shift after each impact due to the deterioration of the conducting pathway. After 11 impacts, the total resistance change exceeds 120 %, as seen in Figure 2.20a. Simultaneously, cumulative AE (acoustic emission) counts during these repeated impacts show a corresponding increase in acoustic hits. However, some of those acoustic events, while associated with the impact, are not linked to damage and include factors like vibrations from the impact tower. Additionally, Figure 2.20b shows that for a specific impact event, the increase in normalized resistance can be attributed to both elastic deformation and the initiation of new damage. During unloading, as certain cracks close and carbon nanotube contacts are re-established, there is a recovery in resistance decrease due to elastic deformation. Overall, the study proves that *in situ* electrical resistance measurement is a potential technique for detecting impact damage propagation and keeping track of the health of FRP structures.

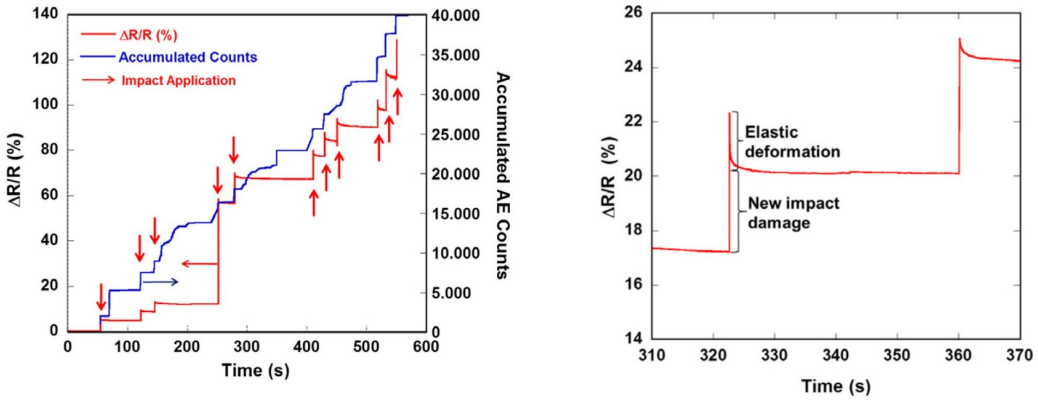

(a) (b)

Figure 2.20: Dynamic response of electrical resistance change and acoustic emission in repeated impact tests: (a) correlation between normalized resistance change variations and accumulated AE counts; (b) increment in normalized resistance change during impact test illustrating elastic deformation and creation of impact-induced permanent damage, from [106].

Grammatikos and Paipetis [107] explored the efficiency of the ERC technique for monitoring structural damages in CFRP composites. A content of 0.5 wt% of MWCNTs was dispersed in the epoxy matrix using an ultrasonic probe, and the laminates were manufactured using unidirectional carbon fiber through the infusion method. Electrical resistance was measured using the two-point probe method, which proved to be a reliable measuring technique. Tensile tests involving loading and unloading were carried out on both the control and MWCNT-enhanced CFRP samples to examine their electrical resistance behavior. Analysis of the electrical resistance in the control samples revealed a dependency on Poisson's ratio effect. This dependency resulted in a short-circuiting effect, causing an overall reduction in electrical resistance during the first five cycles, as depicted in Figure 2.21a. Contrarily, the addition of CNTs significantly reduced the Poisson's ratio effect and made it possible to use electrical resistance measurements to detect strain without producing errors from additional mechanisms (Figure 2.21b). According to the results, adding carbon nanotubes enhanced substantially the sensitivity of electrical resistance measurements. For instance, in the case of control CFRPs, there was only a 3 % increase in normalized electrical resistance, whereas in the MWCNTs-enhanced composites, this increase was approximately 40 %. The authors concluded that introducing MWCNTs has increased the number of electrical contacts in the composite structures. Consequently, the sensitivity of the measurements in the bulk and the through-thickness direction was significantly improved, enabling the detection of even the slightest strain or damage-induced changes.

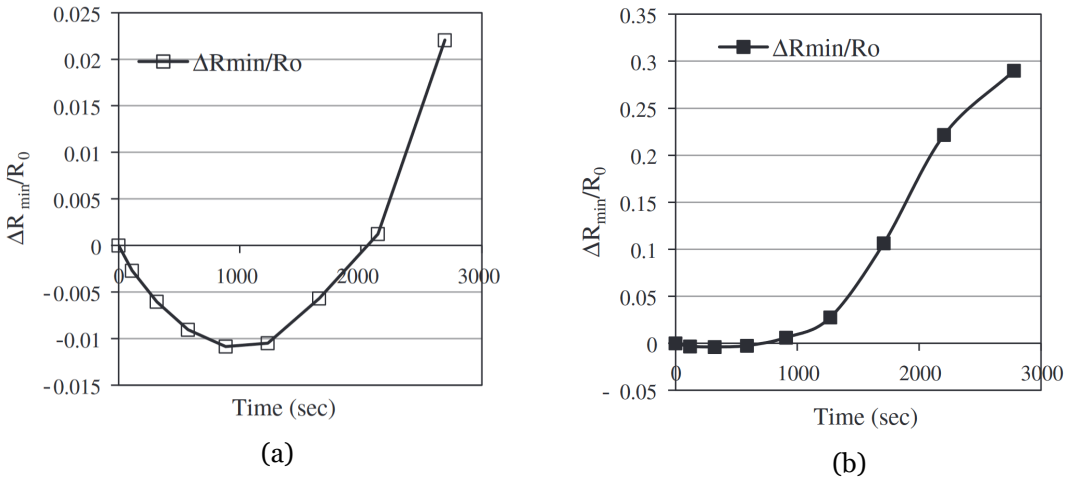

Figure 2.21: Resistance change normalized by the initial resistance at the end of each cycle $(\Delta R/R_{\text{min}})$ *vs.* time: (a) plain CFRPs; (b) MWCNT enhanced CFRPs, from [107].

Arronche *et al.* [108] investigated the use of an epoxy matrix with 0.5 wt% of MWCNTs for damage detection in GFRP laminates. The MWCNTs were dispersed using acetone as a solvent, followed by additional sonication with the epoxy matrix. The composites were manufactured through hand lay-up process employing unidirectional woven glass fiber arranged in a stacking sequence of $[(0/90)_7,0]$. Static tensile tests revealed that MWCNTs do not significantly affect the maximum tensile stress and reduce the longitudinal Young's modulus, possibly related to the lack of interfacial adhesion between the MWCNTs and the epoxy. To compare the effectiveness of two-point probe and four-point probe methods for measuring changes in electrical resistance before and after impact, a drop-weight machine at energy levels of 50 and 70 J was used. The results showed that the four-point probe method was significantly more reliable and repeatable than the two-point probe method. The mean normalized resistivity changes registered a < 10 % variation for the 50 J impact energy and ~ 15 % for the 70 J impact. However, according to the authors, these resistivity changes were not significant for the impact energies applied, revealing a lack of reliability in detecting damages caused by the low-velocity impact. The study also highlights the importance of considering the manufacturing process and material composition when comparing the results of other studies, pointing out that the lack of functionalization of the MWCNTs might explain the lack of damage detection.

Al-Bahrani and Cree [109] investigated real-time detection and quantification of damage in GFRP composites under different impact loadings (12, 24, 36 J). The study focused on the effect of different MWCNTs contents (0.5, 1, 1.5, 2 wt%) on the electrical and mechanical properties of the nano-enhanced composite. Dispersion of the MWCNTs was carried out using a solvent (acetone) with further sonication within the epoxy using a high intensity ultrasonic probe. The solution was then placed between 10 layers of woven plain glass fiber through a hand lay-up process. In-plane electrical resistance measurement based on two-probe technique was used, placing the electrodes on the opposite ends of the samples. A drop-weight impact test machine with a hemispherical impactor was used to carry out the LVI tests. The percolation threshold was reached for the 0.5 wt% MWCNT concentration, registering a value in the range of 10^{-4} S/m. Three-point flexural tests revealed notable improvements in ultimate flexural strength and modulus for the MWCNT-enhanced composites compared to control ones. The optimal concentrations were found to be 1.5 and 2 wt% MWCNTs for flexural strength and modulus, respectively. Additionally, at 1.5 wt% of MWCNTs, the most homogeneous dispersion was observed, with maximum energy absorption and the lowest damage factor. This concentration, showing the highest energy absorption, led to further flexural after-impact tests for 1.5 wt% concentration. Results for flexural stress-strain and normalized residual flexural properties at different impact energies are shown in Figures 2.22a and 2.22b, respectively. As expected, impact events caused reductions in GFRP laminate strength and modulus. With increasing impact energy, residual flexural strength decreased significantly compared to residual flexural modulus, indicating that flexural modulus is less affected by impact damage than flexural strength.

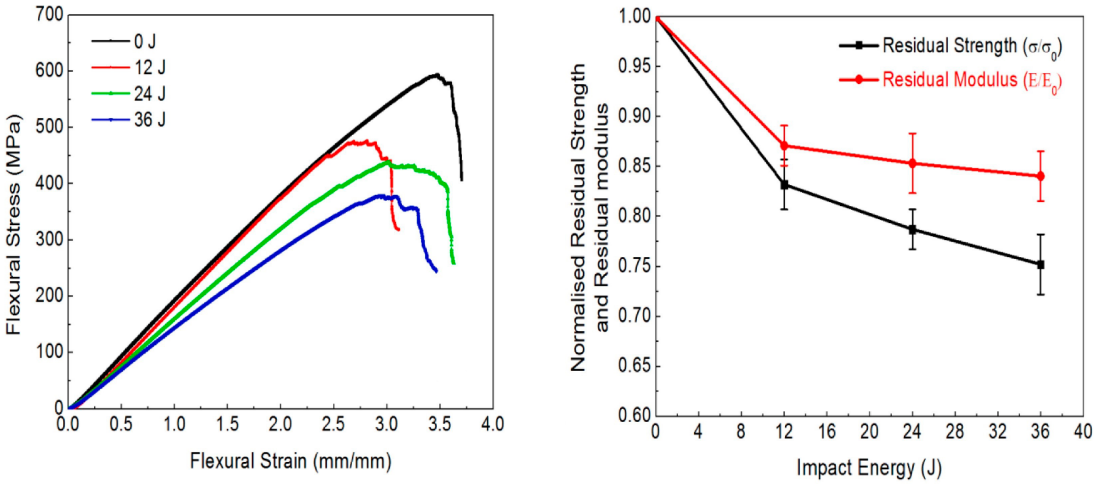

(a) (b)

Figure 2.22: Flexural properties *vs.* impact energy for self-sensing composite with 1.5 wt% MWCNTs concentration: (a) flexural stress-strain; (b) normalized residual flexural properties, from [109].

Analysis of the normalized change in electric resistance ($\Delta R/R_0$) as a function of time for different levels of impact energies reveals that when the sample is subjected to an instantaneous impact load, the normalized electrical resistance change of all samples initially increases linearly with time, reaching a maximum value before gradually decreasing non-linearly until a certain stabilization level is reached. This increase in electrical resistance change is caused by disruptions in the MWCNTs' conducting networks during impact. Upon rebound, some fractures may close (elastic deformation), re-establishing MWCNT contacts and lowering resistance. The authors discovered that composites with higher concentrations of MWCNTs had lower values of $\Delta R/R_0$ than those with lower concentrations. This indicates that composites with the lowest contents of MWCNTs were the most sensitive to damage detection. For example, as shown in Figure 2.23afor the 36 J impact energy, the peak $\Delta R/R_0$ values were 0.51, 0.56, 0.63, and 0.74 for samples containing 2, 1.5, 1, and 0.5 wt% of MWCNTs, respectively. The lower value of $\Delta R/R_0$ for samples with high MWCNT content could be attributed to the higher electrical conductivity of the samples. Interestingly, it should also be noted that the self-sensing specimens containing higher MWCNT concentrations showed a less permanent change to the electrical resistance (λ), and the total response time (time elapsed until stabilization) decreased with increasing MWCNT content. Additionally, it was determined that the peak of the electrical resistance variations increased with increasing impact energy level, as depicted in Figure 2.23b. The paper concludes that it is possible to correlate the degree of damage to the composite structure with the ERC of the nano-enhanced GFRP both during and after impact. Nevertheless, care for the employment of an optimal concentration and fine distribution of MWCNTs are key factors to successfully detect damage at any region in the composite structure.

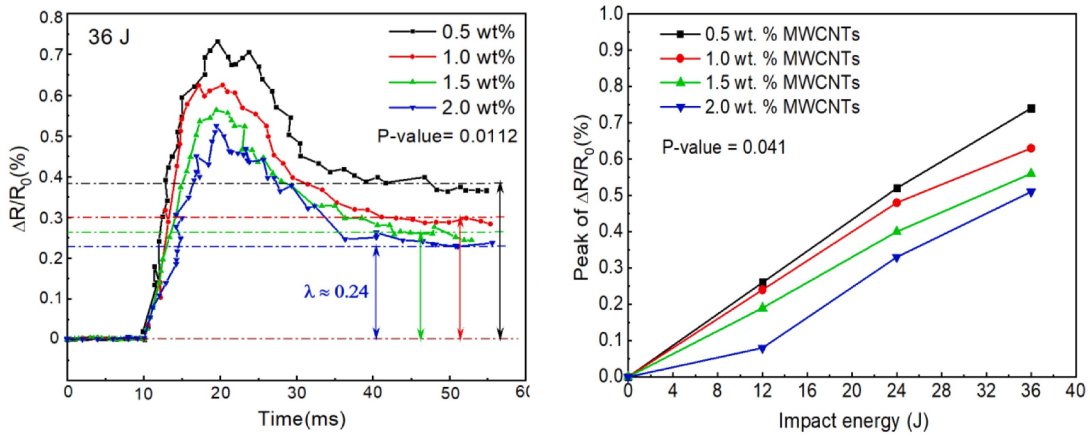

(a) (b)

Figure 2.23: Impact-induced changes in electrical resistance: (a) $\Delta R/R_0$ *vs.* time for different MWCNTs concentration at 36 J impact energy; (b) peak of $\Delta R/R_0$ *vs.* impact energy level for different MWCNT concentrations, from [109].

The aforementioned studies and results showed the effectiveness of integrating CNTs into polymeric insulating matrices, particularly epoxy, as an effective method for establishing a self-sensing network capable of real-time deformation, damage detection, and propagation tracking via electrical resistance measurements. This innovative approach not only offers simplicity but also exhibits remarkable efficiency, thereby holding great promise for structural health monitoring in FRP composite structures.

In the context of CFRPs, where electrical conductivity is inherently more pronounced in the direction of reinforcement, introducing a conductive matrix addresses the challenge of electrical anisotropy by significantly improving the overall piezoresistive sensitivity. Conversely, in GFRP composites, where the reinforcement is inherently non-conductive, the incorporation of CNTs effectively transforms the matrix into a conducive medium for the application of electrical resistivity methods. This approach allows effective strain and damage monitoring under various scenarios, including tensile, flexural, and impact loading. Nevertheless, specific persistent challenges, particularly those associated with uneven dispersion, aggregation at elevated CNTs concentrations, and arrangement of CNTs within the matrix, still need to be overcome as they directly impact the electrical sensing behavior. Table 2.7 summarizes the main aspects of the studies mentioned above, highlighting the materials used, test type, and most relevant results.

Table 2.7: Summarized researches on epoxy matrix dispersed CNTs as multifunctional sensors for SHM of FRPs.

Materials	**Test Type**	**Main Results**	**References**
GFRP/ MWCNTs (0.5 wt%)	Tensile loading	Formation and opening/closing of cracks lead to significant hysteresis in the resistance/strain relations. A parameter for quantitative assessment of damage can be obtained by interpreting the resistance response curves.	Thostenson and Chou [103]
CFRP/ MWCNTs (0.1 - 1.0 wt%)	Tensile loading	The presence of the CNT network acted as a direct sensor of matrix-related damage phenomena, improving the transverse conductivity and enhancing the damage sensing capabilities of the composite.	Kostopoulos *et al.* [104]
GFRP/ MWCNTs (0.1 - 0.5 wt%)	Low-velocity impact	Results showed that it is possible to associate the increase in electrical resistance of the composite with the formation of damages when subjected to a low-velocity impact on its surface.	Monti *et al.* [105]
GFRP/ MWCNTs	Low-velocity impact	Formation of *in situ* electrically percolating networks sensitive to detecting microcrackings initiation and growth. Elastic deformation and damage evolution could be identified from the ERC after repeated impact loadings.	Gao *et al.* [106]
CFRP/ MWCNTs (0.5 wt%)	Tensile loading	Incorporation of CNTs in CFRPs composites reduces the electrical anisotropy of the system. The CNT enhanced CFRPs had increased electrical resistance sensitivity and were found to be more reliable than the plain CFRPs.	Grammatikos and Paipetis [107]
GFRP/ MWCNTs (0.5 wt%)	Low-velocity impact	Four probes measurement produced better sensing data than the two probe method. Resistivity changes under impact loads were not significant for damage detection. Functionalization of the MWCNTs is recommended.	Arronche *et al.* [108]
GFRP/ MWCNTs (0.5 - 2.0 wt%)	Low-velocity impact	Changes in electrical resistance increase with increasing impact energy. Higher MWCNTs concentrations show lower sensitivity and damage factors. Ability to detect and quantify damage from low-velocity impacts.	Al-Bahrani and Cree [109]

Chapter 3

Experimental Procedure

This chapter covers all the pertinent information and methodologies employed to prepare and conduct the experimental work. It begins by introducing the materials used, followed by a detailed description of the procedures employed to manufacture the laminated composites. Subsequently, the experimental setup elucidates the equipment employed for testing and data collection in this study. Furthermore, it provides an explanation of the principles and calculations employed to determine the parameters for the various specimens and tests conducted throughout the research.

3.1 Materials

To manufacture the glass/epoxy laminates, an SR 8100 epoxy resin and an SD 8824 hardener, both supplied by Sicomin®, were used. Table 3.1 gives some relevant information about the SR 8100/SD 8824 epoxy system, such as the viscosity and the mixing ratio of the compounds, as well as the mechanical properties obtained from the given curing cycle. The 1195P woven bidirectional glass fiber (195 g/m^2) with a thickness of 0.17 mm from Rebelco® was used to reinforce the epoxy matrix [110]. Once the glass fiber is electrically insulating, it is possible to restrict the contribution to the electrical conductivity given by the inclusion of MWCNTs in the matrix.

Table 3.1: Physical and mechanical properties of the epoxy resin [111].

Properties	**Unit**	**Sicomin® SR 8100/SD 8824**
Appearance	–	Liquid
Color	–	Light yellow
Viscosity (@ 20°C)	mPa.s	300
Mixing ration (by weight)		100:22
Curing cycle	–	24h @ ambient temperature + 24h @ 40 °C
Modulus of elasticity	MPa	2900
Maximum strength	MPa	108
Elongation at break	%	11.8
Elongation at max strength	%	4.9

To form an electrically semi-conductive network, NC 7000™ multi-walled carbon nanotubes from Nanocyl® were added to the epoxy matrix. These are produced via catalytic chemical vapor deposition process and were chosen due to their excellent purity, reasonable price, and small variation of diameter and size. The NC 7000™ MWCNTs also exhibit a low degree of entanglement and high electrical conductivity, a primary interest in applications requiring low electrical percolation threshold [112]. The properties of the MWCNTs are presented in Table 3.2.

Table 3.2: Physical and electrical properties of the NC 7000™ MWCNTs [112].

Properties	**Unit**	**Value**
Average diameter	nm	10
Average length	μm	1.5
Surface area	m^2/g	250 - 300
Purity	%	90
Metal content	%	< 1
Resistivity	Ω.cm	10^{-4}

To ensure good ohmic contact between the surface of the sample and the probe tips, the 842AR Super Shield™ conductive silver paint was used. This is a solvent-based acrylic lacquer, pigmented with highly conductive silver flake. It has a quick dry time, with no heat cure necessary. It can be applied through spraying or brushing, providing excellent adhesion to plastics, extreme conductivity, and extreme corrosion resistance [113]. The properties of the silver paint can be seen in Table 3.3.

Table 3.3: Physical and electrical properties of the silver paint [113].

Properties	**Unit**	**842AR Super Shield™**
Appearance	–	Liquid
Color	–	Light gray
Density	g/mL	1.7
Viscosity (@ 25°C)	mPa.s	873
Solid Content	%	61
Cure Time (@ 22°C)	h	24
Resistivity	Ω.cm	1×10^{-4}

3.2 Manufacturing Process

The following section will disclose the manufacturing process implemented to obtain the self-sensing composites. As this was an iterative process involving several steps regarding the dispersion and optimization of the MWCNTs content in the epoxy matrix, this section will be divided into the different procedures carried out to obtain the desired solution.

3.2.1 Baseline Procedure

For the preparation of the laminated composites, the manufacturing process given by Santos *et al.* [114] was considered as a baseline, which consisted of an extensive analysis of the effect of some manufacturing parameters on the mechanical properties of nano-reinforced composites.

Therefore, to start the preparation of the nano-reinforced laminates, it is first necessary to measure the required mass of resin and hardener, taking into account the mixing ratio provided by the manufacturer, given in Table 3.1. As described in sub-section 2.3.2.1, the percolation threshold of epoxy-CNT composites is strongly dependent on the processing parameters. Because no defined content value guarantees electrical percolation, the decision was to start with a content of 0.25 wt% of MWCNTs. A Nahita Blue 5162 series electronic scale was used to weigh both the resin and hardener and the MWCNTs.

The dispersion procedure started with adding the pre-calculated weight of MWCNTs to the epoxy matrix, which were mixed using an overhead stirrer Labbox STIV-020-001 (Figure 3.1a) at a speed of 1000 rpm for 3 h. The mixing was combined with an ultrasonic bath through an Argolab AU-65 ultrasonic cleaner (Figure 3.1a) at a frequency of 40 kHz, 180 W, to improve the dispersion of the carbon nanotubes. The mixture was kept in an ice bath throughout the process to avoid overheating. After mixing the MWCNTs, the hardener was homogenized in the mixture for 10 min at 150 rpm.

During the mixing process, there is always the probability that air can be trapped within the matrix, therefore, the entrapped air must be removed to prevent voids from occurring inside the composite layers, which can affect the properties of the structure. As such, the mixture was degassed for 10 min inside a Bacoeng vacuum chamber with a VEVOR 3CFM vacuum pump (Figure 3.1b).

Subsequently, 12 hand-cut 1195P glass fiber layers with dimensions of 330 × 330 mm^2 were stacked one by one, all in the same direction, using the hand lay-up technique. In this step, special care must be taken to ensure precise alignment of the layers and even resin distribution. Once all the layers had been stacked, the entire assembly was placed between two release agent films, and an absorbent fabric was positioned around the assembly to absorb any excess resin and facilitate air circulation.

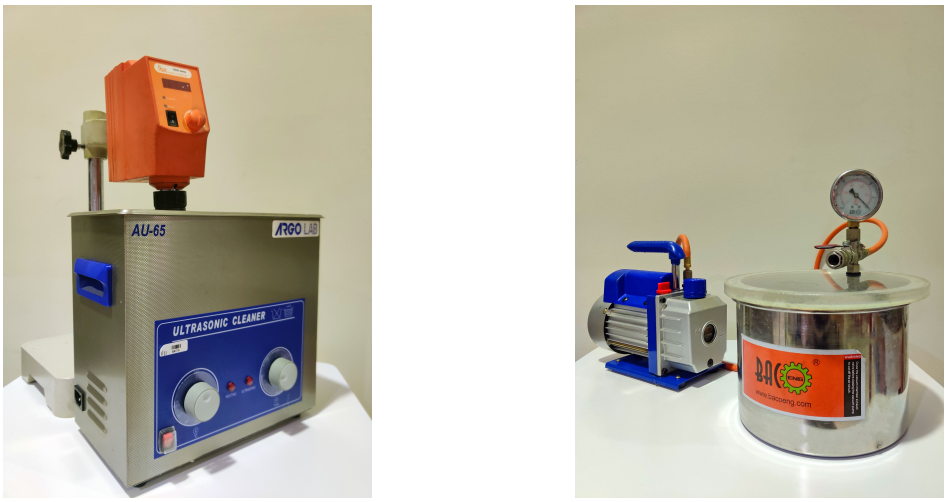

(a) (b)

Figure 3.1: Equipment used for mixing and degassing the CNT-epoxy matrix: (a) Labbox STIV-020-001 overhead stirrer (back) and Argolab AU-65 ultrasonic cleaner (front); (b) VEVOR 3CFM vacuum pump (left) and Bacoeng vacuum chamber (right).

Finally, the assembly was carefully enclosed within a vacuum bag, ensuring airtight sealing, and subjected to a controlled pressure of 2.5 MPa using a hydraulic press. This process was crucial in order to preserve a consistent fiber volume fraction and achieve a uniform thickness across the laminate during the curing phase. The vacuum bag remained attached to the vacuum pump during the first 30 min under the hydraulic press to eliminate any air bubbles remaining in the composite.

The curing process of the laminates adhered to the guidelines provided by the epoxy manufacturer. Initially, the laminate underwent a curing period of 24 hours at room temperature, allowing the chemical polymeric reactions to progress and facilitate the formation of strong molecular bonds. Following the initial curing stage, a subsequent post-cure was conducted at a temperature of 40°C on a Carbolite NR200-F fan convection oven for an additional 24 hours.

After the curing process was completed, samples were cut to test the electrical conductivity using a digital multimeter Keysight 34461A. However, from the samples obtained, no electrical conductivity was measured, raising two fundamental questions: whether the problem was due to the manufacturing process or the insufficient concentration of nanotubes. Based on what has been experimentally observed in the manufacturing procedure, especially during the hand lay-up process, it became evident that some small clusters of carbon nanotubes were still visible in the epoxy matrix, a possible indicator that the lack of conductivity could be related to the manufacturing procedure, namely during mixing.

Nevertheless, to determine whether the MWCNT clusters were still present in the matrix after the curing process, a Nikon SMZ-2T optical microscope was used to evaluate the degree of MWCNTs agglomeration in the laminate samples. As can be seen from the image shown in Figure 3.2a, the dispersion of CNTs in the matrix is roughly poor, evidencing many areas of the laminate with voids where no conductive fillers are present. Additionally, due to the poor dispersion of the nanotubes, the samples have areas of high translucency. As such, a very elucidating image arises when placed under the optical microscope with a light source directed at the face opposite to the one being observed. From Figure 3.2b, it is clear that the MWCNT clusters are still present in the matrix and very far apart from each other, which makes it impossible to form a conductive network, confirming that the carbon nanotubes were not being properly disaggregated and dispersed.

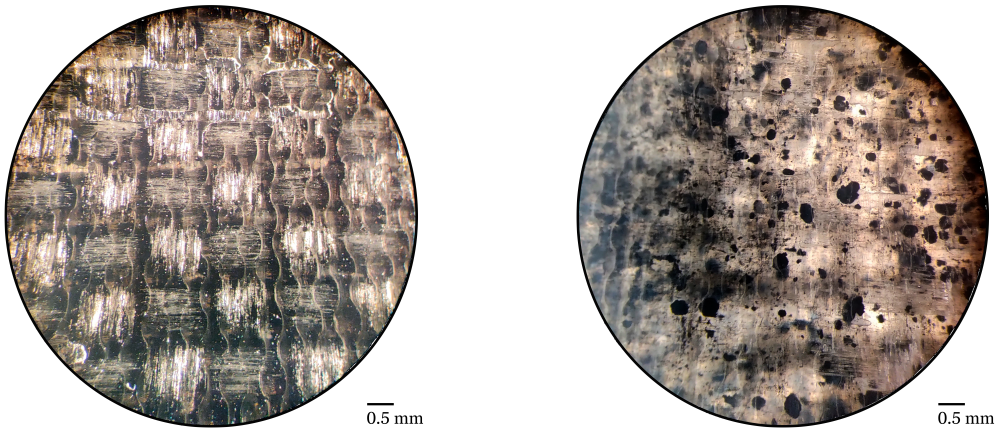

(a) (b)

Figure 3.2: Optical microscopic images of the samples with 0.25 wt% of MWCNTs obtained from the baseline manufacturing procedure: (a) light source directed towards the observed face; (b) light source directed towards the opposite face being observed. Magnification of 20×.

3.2.2 Disaggregation and Dispersion Refinement

At it was previously mentioned, the decision was to look for ways to improve the manufacturing process, and from the conclusions drawn, the methods used in the mixing process, namely the overhead stirring and the ultrasound bath, were not sufficient for even dispersion and disaggregation of the CNTs in the epoxy matrix. To solve this problem, the decision was to introduce an ultrasonic probe to the manufacturing process, a commonly used technique for the disaggregation of carbon nanotubes [107, 109].

As this is a much more invasive equipment than the ultrasound bath, due to the ultrasonic probe being in direct contact with the mixture, it is crucial to bear in mind that disaggregation of nanofillers through an ultrasonic process is accomplished due to cavitation forces,

which can have two contrasting effects. On the one hand, cavitation forces promote the disaggregation of nanofillers, resulting in a well-dispersed mixture with reduced agglomeration and an increased effective aspect ratio. This leads to a decrease in the percolation threshold and increased electrical conductivity. On the other hand, the aggressive cavitation forces can cause the breakage of nanoparticles, particularly for carbon nanotubes, due to their high aspect ratio and low bending strength. This breakage reduces the effective aspect ratio of the nanoparticles, leading to an increase in the percolation threshold and a decrease in electrical conductivity. The prevalence of each mechanism depends on various factors, such as the viscosity of the media. When the media has a lower viscosity, the cavitation forces have a more significant influence, indicating that the sonication process is more effective in such cases. Therefore, it is important to determine the optimum sonication time that achieves a well-disaggregated network without causing excessive breakage of the nanofillers [115].

As such, the equipment used for this process was a Qsonica Q125 Sonicator with a standard probe (Figure 3.3) at a frequency of 20 kHz, 125 W. A total of 1 min of sonication with the probe was carried out. Due to the ultrasonic probe's introduction and considering the cavitation forces previously mentioned, the time spent on the ultrasound bath was reduced to 2 h. Therefore, the mixture would be initially sonicated for 1 h in the ultrasound bath. Afterward, it would pass to the ultrasonic probe for 1 min, with an additional hour in the ultrasound bath. It is important to note that the rest of the steps from the baseline procedure were kept the same, being the only changes applied to the mixing process.

Figure 3.3: Qsonica Q125 Sonicator ultrasonic processor with standard probe.

With the samples in hand, electrical tests were carried out to assess the electrical conductivity of the samples. However, as for the baseline samples, no electrical conductivity was measured. Nevertheless, it was worth understanding if introducing the ultrasonic probe improved the dispersion of the carbon nanotubes. From the optical microscopic image depicted in Figure 3.4a, it is clear that there has been an improvement in the dispersion of the nanotubes in the epoxy matrix, with a significant decrease of voids throughout the matrix. It is also evident from Figure 3.4b that the prevalence of small individual clusters has been significantly reduced, with the majority of zones with larger MWCNTs concentration.

At this point, and not having reached the percolation threshold, the decision was to increase the MWCNTs content in the matrix. Arguably, the disaggregation and dispersion of the CNTs could be further optimized. However, such optimization could take several iterations, with the potential of becoming a very time-consuming task. Therefore, as this work focuses on attaining self-sensing composites with piezoresistive properties, the increase of MWCNTs content seemed to be the most appropriate approach to this particular case.

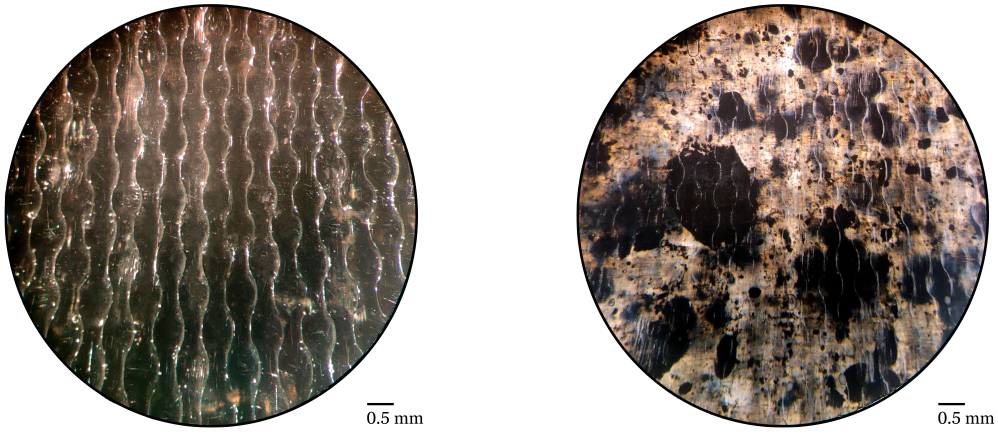

(a) (b)

Figure 3.4: Optical microscopic images of sample with 0.25 wt% of MWCNTs obtained from the refined manufacturing procedure: (a) light source directed towards the observed face; (b) light source directed towards the opposite face being observed. Magnification of 20×.

3.2.3 MWCNTs Content Optimization

Having concluded that the MWCNTs content of 0.25 wt% was below the percolation threshold for this particular case, a MWCNTs content increase in the epoxy matrix was carried out. To avoid the risk of falling below the percolation threshold once again, and taking into account the results reported in the literature, the decision was to increase the carbon nanotubes content to 0.5 wt%. To manufacture the samples with 0.5 wt% of MWCNTs, the same steps indicated in the baseline procedure were followed, along with the refinements introduced to the mixing process. However, due to an increase in the MWCNTs content, the mixture's viscosity also increased significantly, which implied minor tweaks to the overall process. In line with the fact that a higher mixture viscosity reduces the cavitation forces' effectiveness, the ultrasonic probe's time was increased from 1 to 1.5 min. Secondly, the hardener had to be dispersed at a higher rate, increasing the speed from 150 to 800 rpm. Finally, the degassing time was also refined, increasing from 10 to 15 min.

Upon completion of the manufacturing process, tests were performed to determine the electrical conductivity of the laminated composite. Preliminary tests measured resistivity values in the order 10^4 Ω.cm, being in the range of semiconductor materials, making it useful for applications as piezoresistive sensors [116]. From these results, it can be concluded that the percolation threshold has been reached. Observations under the optical microscope comparing the 0.25 wt% with 0.5 wt% MWCNTs can be seen in Figure 3.5, where it is possible to observe the difference between the samples with different nanotube contents. This is a very interesting observation, as it is not only possible to perceive the undoubtedly superior homogeneity and dispersion of nanotubes for the 0.5 wt% content, but it can also be depicted as a "visual representation" of the percolation threshold.

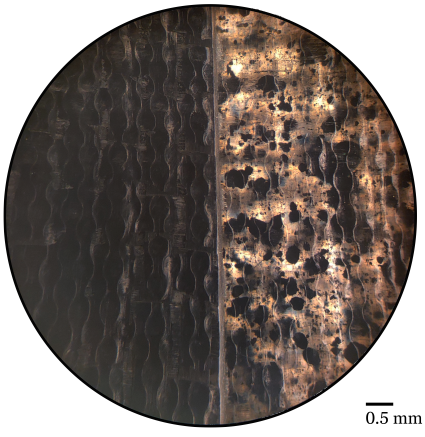

Figure 3.5: Optical microscopic image of sample with 0.5 wt% of MWCNTs (left) and sample with 0.25 wt% of MWCNTs (right) obtained from the refined manufacturing procedure. Light source directed towards the opposite face being observed. Magnification of 20×.

3.3 Specimens

In preparation for the experimental characterization, the specimens were obtained from the original plates using a Struers Accutom-2 cutting machine, equipped with an IsoMet diamond disc 15LC. To ensure that the specimens possessed the specific dimensions and geometry, special care was taken throughout the cutting process by maintaining an appropriate cutting speed and lubrication of the diamond disc.

In order to proceed with all the desired tests, the specimens are cut in a flat rectangular shape, with dimensions of 100 × 100 × 2.2 mm^3, as depicted in Figure 3.6.

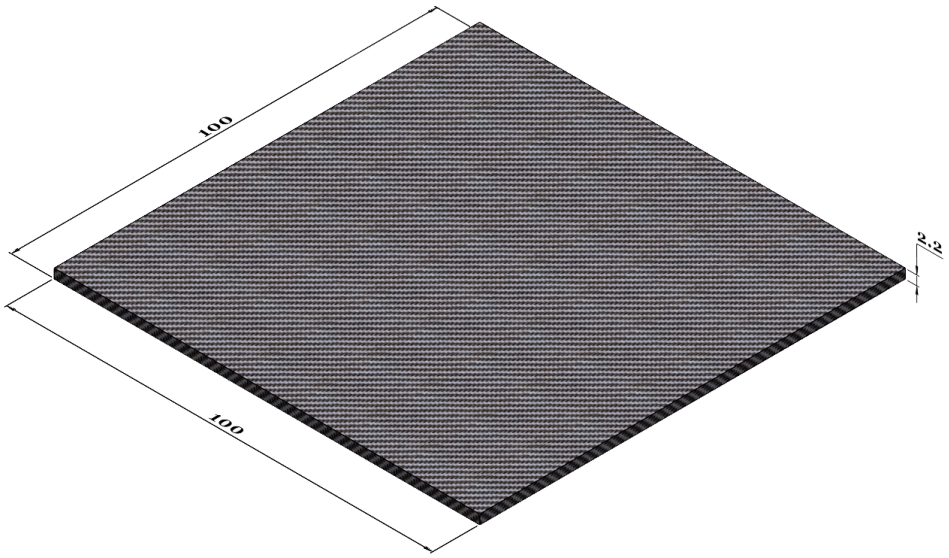

Figure 3.6: Schematic specimen geometry and dimensions.

3.4 Testing Procedure

3.4.1 Flexural Properties

Flexural characterization of the specimens was performed both before and after the LVI. These are of paramount importance to assess the mechanical properties of the laminated structure before and after the impact, as well as evaluate how the introduction of carbon nanotubes to the epoxy matrix influences the mechanical properties of the laminates.

Following the recommendations of the ASTM D790 [117] standard test method, three-point bending (3PB) static tests were carried out at room temperature. The Shimadzu Autograph AGS-X universal testing machine with a 10 kN load cell and a displacement rate of 2 mm/min was used to test the samples. The data from the flexural test is processed using the *Trapezium v1.5* software. A schematic representation of the setup used in the 3PB tests is depicted in Figure 3.7.

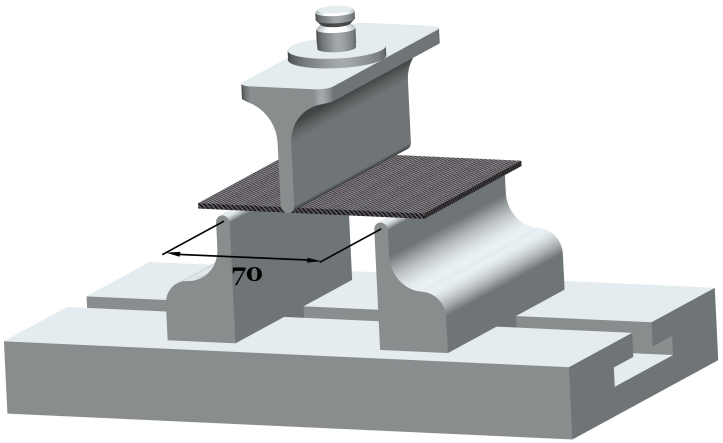

Figure 3.7: Schematic view of the 3PB apparatus.

It is important to note that the commonly used span-to-depth ratio of 16:1 was not applicable to this case. According to the ASTM D790 [117] standard, for high strength reinforced composites, the support span-to-depth ratio shall be chosen such that failures occur in the outer fibers of the specimens, due only to the bending moment. Therefore, a span-to-depth ratio larger than 16:1 may be necessary. Having this in mind, and in order to be possible to comply with the specimens' dimensions, the recommended support span-to-depth ratio of 32:1 was used, resulting in a span length of 70 mm.

The flexural stress, also known as bending stress, was obtained from the nominal stress at the central span section using Equation 3.1:

$$\sigma_f = \frac{3PL}{2wb^2} \quad (3.1)$$

where P is the load, L the span length, w the width of the specimen, and b the thickness of the specimen. The flexural strain, which is the nominal fractional change in the length of an element of the test specimen outer surface at the central span, can be calculated as given in Equation 3.2:

$$\varepsilon_f = \frac{6Db}{L^2} \quad (3.2)$$

where D is the deflection. Both flexural strength and strain can be correlated in a strain-stress curve, as depicted in Figure 3.8. This figure shows a schematic example of typical flexural stress-strain curves of specimens under transverse loading. The flexural stress-strain curve of FRPs resembles a combination of those same curves from its main constituents, the matrix and the fibers, where the reinforcing phase (fibers) is considered to be totally brittle, and the matrix phase to be reasonably ductile [118].

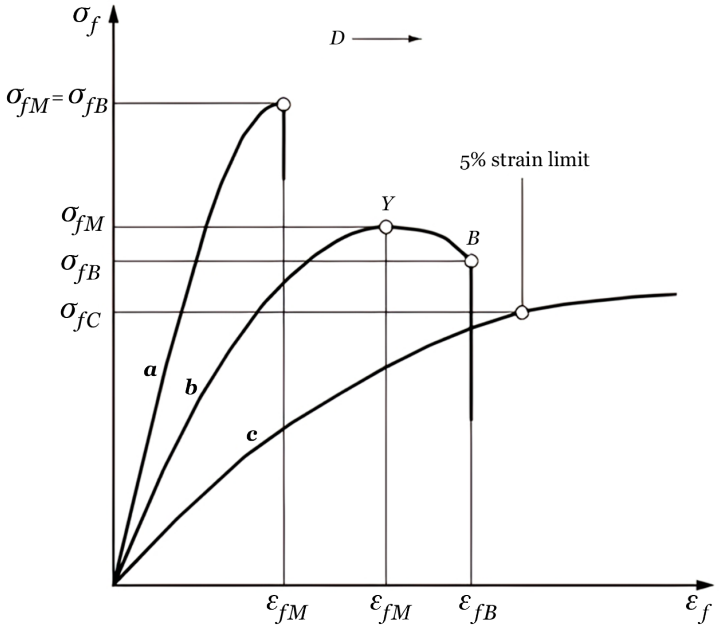

Figure 3.8: Typical flexural stress-strain curves for unreinforced and reinforced plastics for specimens subjected to transverse loading, adapted from [117].

Additionally, from Figure 3.8, it is also possible to distinguish three curves that correspond to different behaviors upon transverse flexural loading. Curve (a) depicts a specimen that breaks before yielding. Therefore, the failure stress, σ_{fB}, matches the maximum flexural stress, σ_{fM}, in which case $\varepsilon_{fB} = \varepsilon_{fM}$. On the other hand, curve (b) shows a specimen that yields (Point Y) and then breaks (Point B) before it reaches the 5 % strain limit. In this case $\varepsilon_{fB} > \varepsilon_{fM}$. Lastly, curve (c) displays a specimen that neither yields nor breaks before the 5 % strain limit.

The flexural modulus was determined accordingly to the ASTM D790 standard. Using the chord method, two discrete points are chosen at the stress-strain curve on the elastic region, as depicted in Equation 3.3:

$$E_f = \frac{\sigma_{f2} - \sigma_{f1}}{\varepsilon_{f2} - \varepsilon_{f1}} \quad (3.3)$$

where σ_{f1} and σ_{f2} are the flexural stresses, and ε_{f1} and ε_{f2} are the flexural strain values measured at the predetermined points on the load-deflection curve.

Lastly, to ascertain any deviation and/or associated error with the, at least, three measurements performed for each condition, the mean values of the tested properties (flexural strength, flexural strain, and flexural modulus), as well as the standard deviation of the experimentally obtained values, were computed by Equations 3.4 and 3.5, respectively, as expressed below

$$\overline{X} = \frac{\sum_{i=1}^{n} X}{n} \quad (3.4)$$

$$SD = \sqrt{\frac{\sum_{i=1}^{n} (X - \overline{X})^2}{n - 1}} \quad (3.5)$$

where $\overline{X}$ is the arithmetic mean of the set of tests, n is the number of tested specimens, X is the value of a single test for a given property, and SD is the standard deviation.

3.4.2 Low-Velocity Impact Tests

The low-velocity impact tests were conducted at ambient temperature using a drop-weight testing machine IMATEK-IM10, according to the ASTM D7136 standard [119]. This equipment consists of a tower with two guiding rails, in which the impactor moves through bearings. The combination of height, mass, and velocity provides the impact energy, which can be adjusted through the drop height. The existence of an anti-rebound system prevents a second impact from occurring in the same test. Impact parameters such as force, velocity, and displacement as a function of time were recorded through an electronic sensor and a load cell, after which the data is automatically processed in the *Impact v1.3* software.

Specimens with dimensions and geometry described in section 3.3 were secured with four rubber clamps to a supporting frame. The clamping fixture of the specimens has a cut-out with an area of 75×75 mm^2. The specimens are then impacted precisely at their center, using a hemispherical impactor head with a diameter of 10 mm and mass of 2.82 kg. The rounded shape of the impactor head was chosen to avoid penetration of the specimens. A schematic representation of the experimental setup used to perform the low-velocity impact tests is depicted in Figure 3.9.

Following the barely visible impact damage approach, two different impact energies, 3 and 6 J, were selected according to preliminary impact tests. For each energy level, six specimens were tested. Out of these, three were selected to assess the post-impact flexural properties of the composites, while the remaining three were used to evaluate the post-impact cyclic behavior. Overall, 24 specimens were tested (12 control + 12 MWCNT-enhanced).

The details of the low-velocity impact test parameters, including the drop mass, drop height, and impact velocity for each of the two impact energies, can be found in Table 3.4.

Table 3.4: Low-velocity impact test parameters.

Impact Energy [J]	**Drop Mass [kg]**	**Drop Height [m]**	**Impact Velocity [m/s]**
3	2.82	0.11	1.46
6	2.82	0.22	2.06

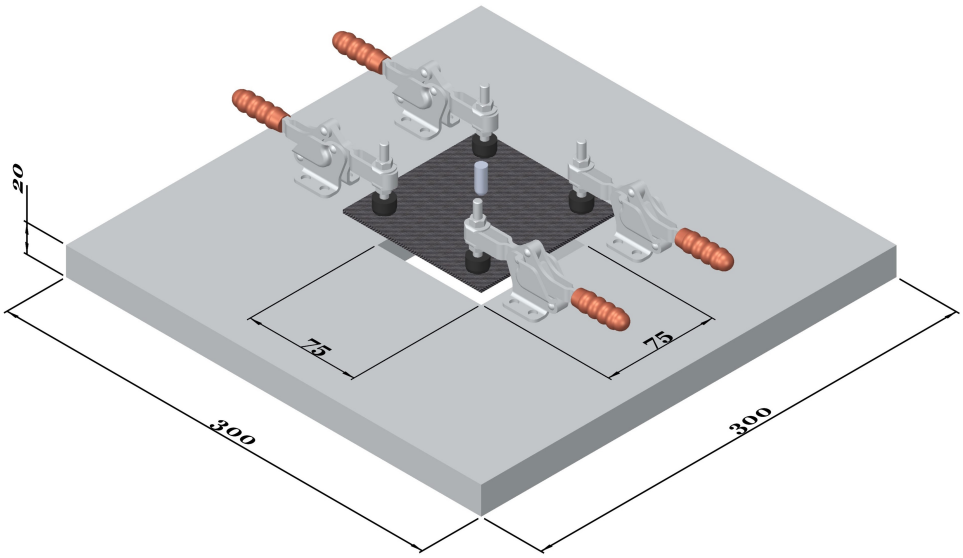

Figure 3.9: Schematic view of the low-velocity impact test apparatus.

3.4.3 Resistance Measurements and Piezoresistivity

As already mentioned, a digital multimeter Keysight 34461A was used to measure direct current (DC) electrical resistance. The measurements of electrical resistance for all the self-sensing composite samples were conducted at room temperature using a two-point probe technique. This method was preferred because it is the simplest and most common method of measuring the resistivity, and has successfully been applied in literature for resistance measurements [105, 106, 109]. The two-point probe technique is particularly useful when the resistance of a given sample is large, as it allows for the determination of changes in resistivity along the length of the sample [120].

As the main goal of this work is to monitor the damage on the composite structure upon a LVI, the electrode configuration consists on a volumetric electrical resistance measurement in order to capture the damage throughout the whole composite thickness. Based on the configurations used by Gao *et al.* [106] and Al-Bahrani and Cree [109], copper electrodes were fixed on the opposite ends of the sample using the 82AR Super Shield™ conductive silver paint by covering the entire specimen thickness. Prior to the application of silver paint, the surfaces of the specimens were cleaned and slightly sanded. The contact resistance was neglected, given that the recorded electrical resistance for all specimens was within the range of kΩ to MΩ. A schematic representation of the electrodes configuration can be seen in Figure 3.10.

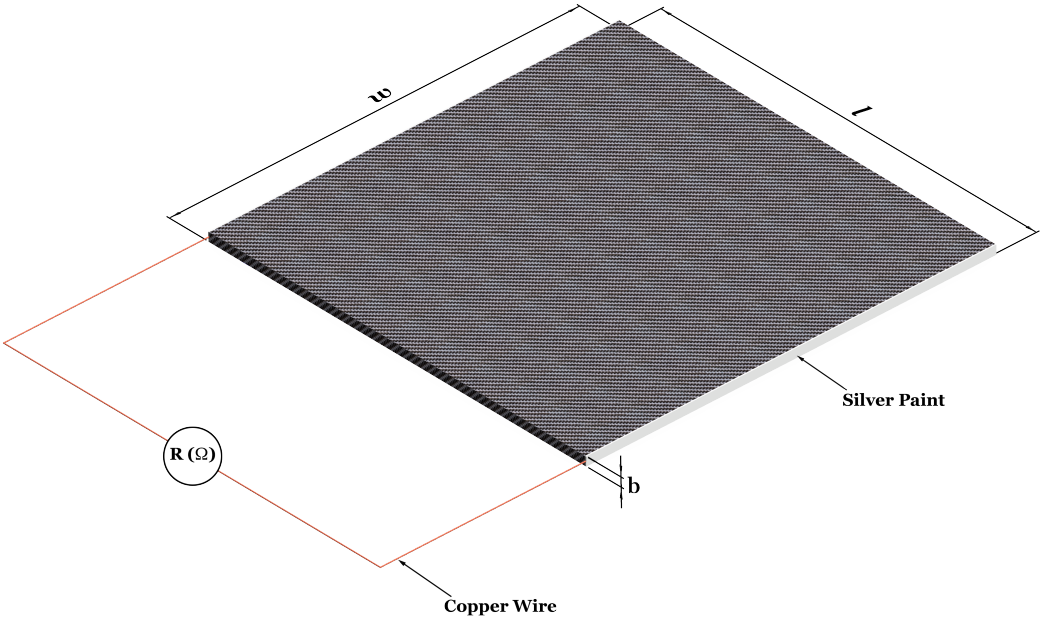

Figure 3.10: Schematics of electrode's disposition for resistance change monitoring.

Due to the electrode configuration, located at opposite ends of the sample, the resistivity measurements involved volume resistivity, which is calculated by Equation 3.6 [120]:

$$\rho_v = R\frac{wb}{l} = R\frac{A}{l} \quad (3.6)$$

where ρ_v is the volumetric resistivity, R is the measured resistance, w is the width of the sample, b is the thickness of the specimen, l is the sample length and A is the electrode area (cross-section area of the specimen).

It is of paramount importance to know that resistance and resistivity have different meanings. The resistivity depends on the type of material, while the resistance depends on how much of the material is present. In general terms, resistance is the capacity of a material to oppose the flow of an electrical current while resistivity is calculated by measuring of resistance. In turn, resistivity is the reciprocal of conductivity [120]. This means that a high resistivity is the same as a low conductivity, as given in Equation 3.7:

$$\rho_v = \frac{1}{\sigma_v} \quad (3.7)$$

where σ_v is the volumetric conductivity.

Simultaneously with the 3PB tests, electrical resistance measurements were performed to evaluate the piezoresistive behavior of the self-sensing composites. During the monotonic and cyclic flexural tests, the Keysight 34461A digital multimeter was connected to the specimen's electrodes, continuously recording the electrical resistance in real time. The digital multimeter recorded the data from the resistance measurements for later correlation with the flexural data obtained at a rate of 1 point per second. Figure 3.11 depicts the experimental setup for the piezoresistive measurements under 3PB tests.

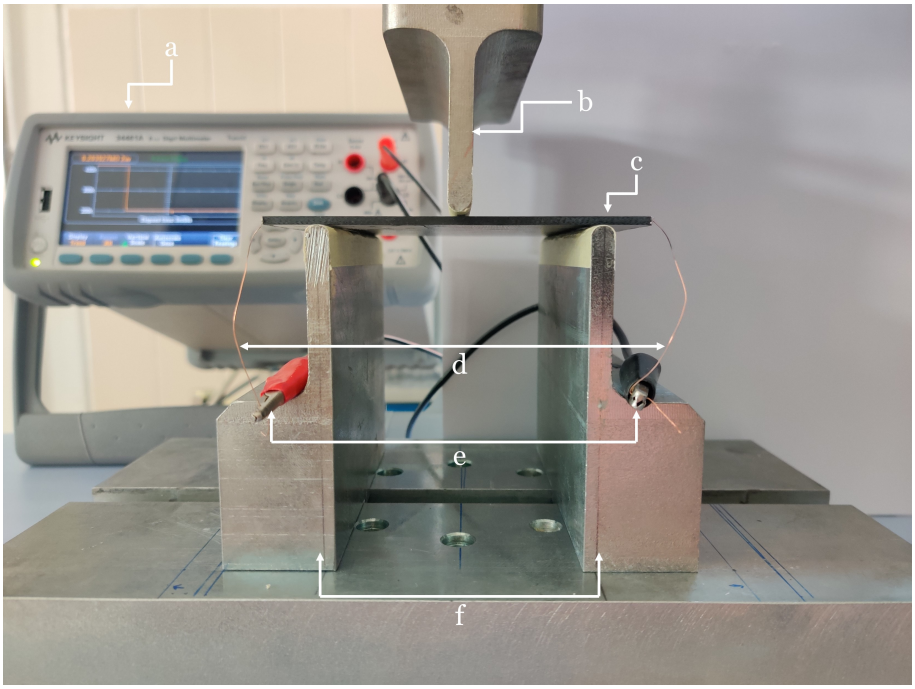

Figure 3.11: Experimental setup for the piezoresistive flexural tests: (a) Keysight 34461A; (b) loading nose; (c) specimen; (d) copper electrodes; (e) electrical connections; (f) loading supports.

As previously introduced in sub-section 2.3.2.2, the piezoresistive sensitivity of the self-sensing composites is determined by the gauge factor. This parameter is calculated on the linear section of the electrical resistance change and strain curve. Having in mind the Equation 2.1, under piezoresistive flexural tests, the gauge factor can be quantitatively calculated using Equation 3.8:

$$GF = \frac{\Delta R/R_0}{\varepsilon_f} \quad (3.8)$$

where $\Delta R/R_0$ is the normalized electrical resistance change, and ε_f is the flexural strain.

Under low-velocity impact, the assessment of the piezoresistive behavior followed the same principles as for the flexural tests. The digital multimeter was connected to the copper electrodes and continuously recorded the changes in electrical resistance throughout the impact event. However, in this case, the digital multimeter was set to record the data from the resistance measurements at the smallest rate possible (1 point every 0.407 ms). The experimental setup used for the LVI piezoresistive tests is depicted in Figure 3.12.

Is it important to note that, both on the flexural and LVI piezoresistive tests, the metallic components comprising the experimental apparatus (e.g., loading supports, loading nose, supporting frame, impactor head), were covered with insulating paper tape to safeguard the electrical signal from potential disruptions caused by the conductive nature of these metallic components, maintaining data accuracy and reliability.

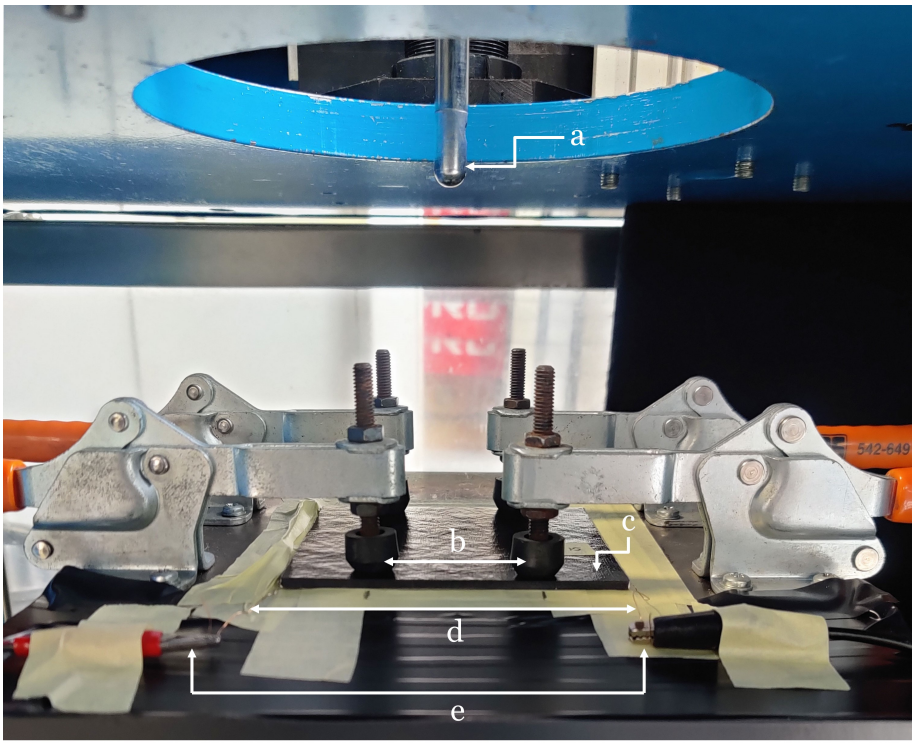

Figure 3.12: Experimental setup for the piezoresistive LVI tests: (a) impactor head; (b) rubber clamps; (c) specimen; (d) copper electrodes; (e) electrical connections.

Chapter 4

Results and Discussion

4.1 Flexural Properties

As already stated, aerospace composite structures subjected to low-velocity impact events suffer several internal damages with the potential to jeopardize the composite structure's ability to withstand loads. Therefore, this section pretends to assess the mechanical properties of the composites both before and after the low-velocity impact tests, as well as understand how the introduction of MWCNTs to the epoxy matrix contributes to the overall mechanical properties.

4.1.1 Before Low-Velocity Impact Tests

Static flexural tests were performed on the control and the 0.5 wt% MWCNT-enhanced GFRP laminates to evaluate their bulk stiffness and strength before the LVI tests. The representative flexural stress–strain behavior of these composites is shown in Figure 4.1.

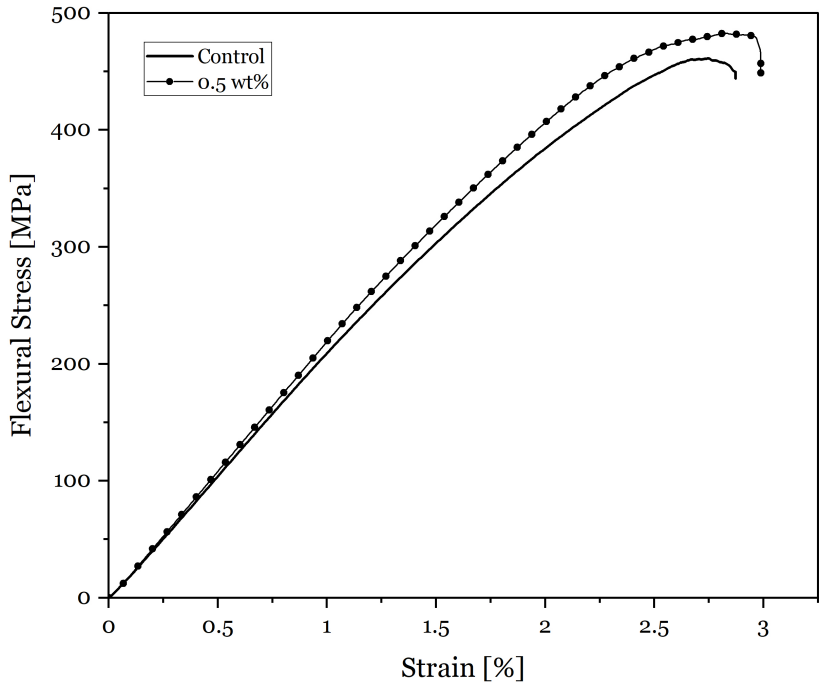

Figure 4.1: Representative flexural stress-strain curves before low-velocity impact tests.

Both curves show an initial linear increase of the bending stress with the strain, where both fibers and matrix deform elastically. As the deformation progresses, the curve transitions into a nonlinear elastic regime at around 1.3 % and 1.5 % of flexural strain for the control and MWCNT-enhanced composites, respectively. The fibers and matrix begin to deform plastically, and the stress-strain curve is no longer linear. The point of deviation from linearity indicates failure initiation owing to the development of cracks on the tension side (opposite to the direction of loading) [118, 121]. As the composite approaches the maximum flexural stress and before the material's ultimate failure, both curves are marked by an increase in strain with little or no increase in stress. This suggests that specific damage phenomena are occurring within the material. These could be attributed to intricate factors, such as fiber-matrix debonding, fiber pull-out, fiber breakage, and delaminations. As the load increases, individual fibers within the material may experience different stress levels depending on their orientation, position within the matrix, and inherent variations in material properties. Some fibers might start to reach their failure point and break, reducing load-bearing capacity. However, other fibers might still be intact and capable of carrying a portion of the load. This leads to a temporary plateau in the stress-strain curve, more pronounced in the MWCNT-enhanced composite, due to an additional crack propagation resistance from the pull-out and bridging of MWCNTs [122, 123].

Despite the curves displaying an identical behavior, it is clear that the specimens containing 0.5 wt% of MWCNTS have superior flexural strength, together with a linear increase in the stiffness (slope) relative to the control composite, resulting in a higher flexural modulus, as can be seen in Table 4.1. Both flexural strength and modulus of the specimens containing 0.5 wt% of MWCNTS were superior to the control laminates. Flexural strength had a 3.25 % enhancement compared with the control composites, while the flexural modulus registered a 3.36 % increase. This improvement in strength and modulus can be attributed to a more effective load transfer mechanism from the epoxy matrix to the reinforcing fibers due to the presence of the MWCNTs [45, 109].

Table 4.1: Flexural properties before low-velocity impact tests.

Specimen	**Flexural Strength [MPa]**	**Flexural Modulus [GPa]**	**Failure Strain [%]**
Control	465.14 ± 4.66	22.31 ± 1.23	2.69 ± 0.15
0.5 wt%	480.81 ± 4.86	23.09 ± 0.36	2.81 ± 0.02

4.1.2 After Low-Velocity Impact Tests

Post-impact flexural tests were performed on both the control and MWCNT-enhanced specimens, and the representative flexural stress-strain curves are depicted in Figure 4.2. The non-impacted curves are also plotted to give a better perspective on the changes caused by the low-velocity impacts.

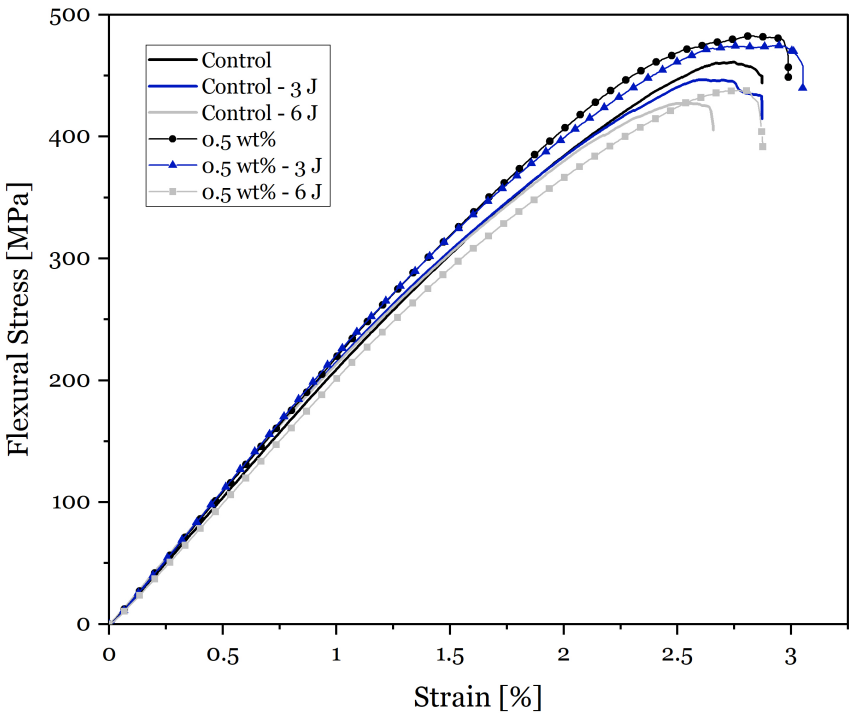

Figure 4.2: Representative flexural stress-strain curves before and after low-velocity impact tests.

By observing the representative curves, a reduction in flexural strength can be clearly identified for all the pos-impacted curves, while the flexural modulus exhibits a slighter reduction, as will be explained later in this section. Contrary to initial expectations, after the 3 J impact, both control and MWCNT-enhanced specimens did not experience any reduction regarding the ultimate failure strain, even showing a slight increase, as seen in Table 4.2. This outcome can be attributed to a combination of various factors. Firstly, it is important to note that despite carefully following the manufacturing process, the results can be affected by variability due to the presence of defects or small changes in the composition of the laminate (e.g., fiber/matrix volume), leading to differences in mechanical properties. A similar observation can be found in Al-Bahrani and Cree [109], where the reduction in ultimate flexural strain after the LVIs does not follow a consistent trend, with 12 J impacts causing a higher reduction in ultimate flexural strain than 24 J and 36 J energy impacts. In addition, the relatively low energy input of 3 J may not have surpassed the material's damage threshold to induce a drastic alteration in ultimate flexural

strain. This hypothesis follows the observations reported by Strugala *et al.* [124], which found that a 3 J impact in a seven-layer plain woven GF/epoxy laminate caused insignificant internal damages to the composite structure. As such, it is plausible to state that a 3 J impact energy may be insufficient to inflict significant internal damages capable of compromising the flexural strain after the impact.

Table 4.2: Flexural properties after low-velocity impact tests.

Specimen	**Energy [J]**	**Flexural Strength [MPa]**	**Flexural Modulus [GPa]**	**Failure Strain [%]**
Control	3	448.37 ± 2.32	21.92 ± 0.03	2.81 ± 0.08
	6	416.93 ± 2.55	20.78 ± 0.41	2.62 ± 0.06
0.5 wt%	3	467.43 ± 10.51	22.79 ± 0.43	2.95 ± 0.17
	6	455.23 ± 21.54	21.74 ± 0.69	2.80 ± 0.01

Table 4.3 shows the normalized residual flexural properties of the composites after the low-velocity impacts. As expected, the 3 J impact inflicted less damage, with both the control and MWCNT-enhanced specimens showing a decrease in flexural strength of approximately 4 % and 3 %, respectively. Moreover, the flexural modulus underwent a slight reduction of 1.7 % for the control samples, and 1.3 % for the MWCNT-enhanced ones. Following the 6 J impact, the flexural modulus shows a reduction of 6.9 % and 5.8 % for the control and MWCNT-enhanced specimens, respectively. On the other hand, the flexural strength decreases by 10.4 % for the control specimens, almost double the 5.4 % reduction experienced by the MWCNT-enhanced counterparts, suggesting that the property enhancement by adding MWCNTs will be more pronounced for higher impact energies.

As seen, the residual flexural strength has a more significant reduction and to a greater extent when compared to the residual flexural modulus. This can be explained by considering the nature of impact loading. Impact events typically result in localized damage within the composite structure, affecting specific regions where the impact occurred. The flexural strength is more sensitive to this localized damage because it quantifies the maximum force the composite can withstand at the precise point of impact, and is dramatically reduced due to the presence of impact degradation. In contrast, the flexural modulus is determined by analyzing the material's response to deformation across its entire span. It considers the material's overall behavior throughout the entire force-deflection curve. Consequently, the flexural modulus is less influenced by localized damage caused by impact since it considers the material's global response [109, 125]. In conclusion, the higher sensitivity of the flexural residual strength to impact damage resides in the fact that damage is localized to the impact site and, therefore, has a minimal effect on the other macro properties, such as the flexural modulus.

Additionally, the composites containing 0.5 wt% of MWCNTs experienced a marginal reduction in failure strain (< 1 %) in contrast to the control samples (2.6 %). This can be explained as a consequence of the crack bridging and pull-out toughening mechanism created by the MWCNTs network inside the matrix, resulting in increased fracture toughness [45]. Overall, the results show that incorporating MWCNTs improves post-impact flexural properties and enhances the impact damage resistance of the composites.

Table 4.3: Normalized residual flexural properties after low-velocity impact tests.

Specimen	**Energy [J]**	σ_f / σ_{f0}	E_f / E_{f0}	ε_f / ε_{f0}
Control	3	0.964	0.983	1.04
	6	0.896	0.931	0.974
0.5 wt%	3	0.972	0.987	1.05
	6	0.946	0.942	0.996

4.2 Low-Velocity Impact Tests

Besides the flexural properties, it is crucial to understand how the introduction of MWCNTs to the epoxy matrix affects the laminate response to low-velocity impacts. A comprehensive analysis of parameters like absorbed energy, peak force, and maximum displacement is presented herein. This section also dissects the aftermath of the LVIs by investigating the damage to the laminated structure through a cross-section cut of the samples.

4.2.1 Impact Response and Damage Characterization

The representative force-displacement curves depicted in Figure 4.3 provide crucial information regarding the peak force, which is the maximum load the specimen can sustain on fracture. It is observed that the MWCNT-enhanced composites exhibit a slightly higher peak force value, measuring 1.61 kN and 2.32 kN for the 3 J and 6 J impact, respectively. In contrast, the control samples exhibit a slightly lower peak force of 1.59 kN for the 3 J and 2.30 kN for the 6 J impact. This indicates that the MWCNT-enhanced composites can withstand a marginally higher force before significant damage starts to develop within the composite. The higher peak force sustained by the composites with 0.5 wt% of MWCNTS reveals improved impact resistance and ability to better withstand external forces.

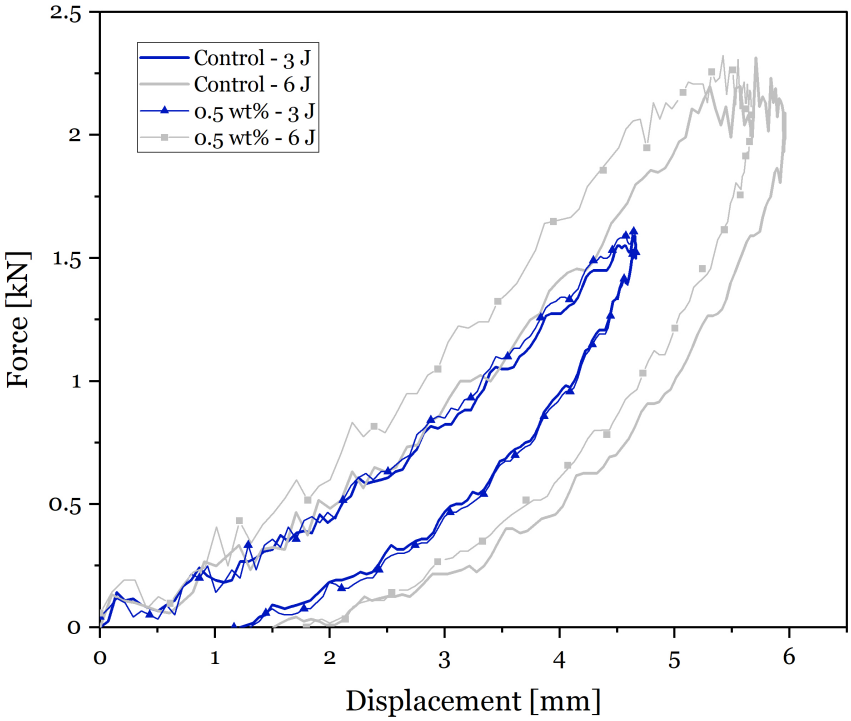

Figure 4.3: Representative force-displacement curves from the low-velocity impact tests.

In addition, the MWCNT-enhanced composites display a lower maximum displacement of 4.58 mm for the 3 J and 5.60 mm for the 6 J impact. On the other hand, the control sample exhibits a slightly higher maximum displacement of 4.67 mm and 6.01 mm for the 3 J and 6 J impact, respectively. This means that although the composites with 0.5 wt% of MWCNTs can endure higher forces, they undergo less deformation or displacement during the impact event, which can be associated with their higher stiffness. From the representative force-displacement curves given in Figure 4.3, one can also determine the energy absorbed by the composite through the integration of the area between the loading and unloading phases of the curves. The absorbed energy is one of the most critical parameters to access in low-velocity impact events, as it refers to the total energy dissipated by the composite during impact through the formation of damage inside it. This approach allows to quantitatively determine the energy transformations within the composite material during the low-velocity impact event.

Figure 4.4 displays the representative energy-time curves obtained for the 3 J and 6 J impacts in both types of specimens. The peak on the curves represents the impact energy, and the decrease corresponds to the elastic recovery after the impact. In an ideal scenario, the curve would return to zero after the peak energy has been reached, which cannot be achieved due to friction and elastic energy. In this particular case, part of the impact energy has not been absorbed elastically and has been converted into structural damage, which means that no penetration occurred, and the excessive energy (impact energy minus absorbed energy) was retained by the impactor and used to rebound after impact.

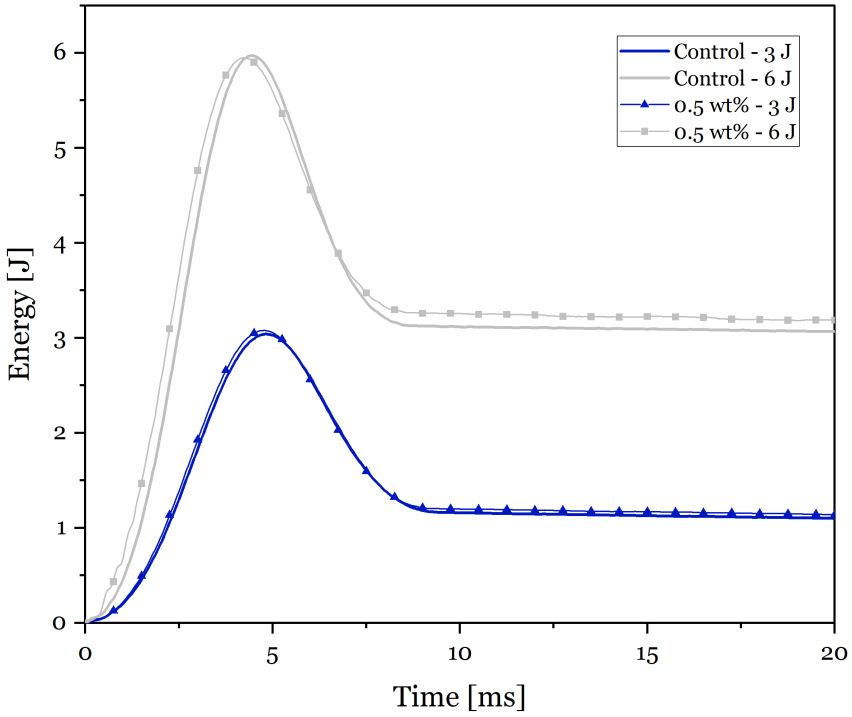

Figure 4.4: Representative energy-time curves from the low-velocity impact tests.

A deeper analysis of the curves previously shown reveals noteworthy differences in absorbed energy between the 3 J and the 6 J impacts. The 3 J impact curves do not reveal significant differences between the MWCNT-enhanced and the control composites. The specimens containing 0.5 wt% of MWCNTs exhibit marginally higher energy absorption than the reference material, with a mere increase of 1.67 %, showing that at lower impact energies, the influence of adding MWCNTs to the matrix does not reflect in major differences. However, for the 6 J impact curves, noticeable differences concerning the amount of energy absorption can be found. The curve representing the composites with 0.5 wt% of MWCNTs exhibits a higher value of absorbed energy than the control sample, with an increase of roughly 3.87 %.

The highest energy absorption ratio is registered for the 6 J impact, with the composites containing 0.5 wt% of MWCNTs reaching a value around 54 %, while the control samples register a value of 52 %. On the other hand, lower percentages of absorbed energy ratio are seen for the 3 J impact energy, as both the control and MWCNT-enhanced composites reach a value of approximately 40 %. The lower energy absorption ratio observed on the 3 J energy impacts is expected, once lower impact energy levels result in less induced damage to the composite. Therefore, the composites dissipate less energy through damage.

At this point, it remains unclear whether the MWCNT-enhanced composites demonstrate a better impact behavior regarding developed damage. Despite the increased energy absorption by the MWCNT-enhanced composites for higher values of impact energy, this can be explained as a result of the additional energy consumption mechanisms provided by the breakage, pull-out, and bridging of the MWCNTs, not necessarily meaning higher development of structural damages associated to LVI. In fact, it is most likely that such damages are predominant in the control specimens, as all the energy will be dissipated through matrix cracking, fiber breakage, and/or delaminations, resulting in an increased damaged area [80, 81].

Finally, Figure 4.5 displays the impact force-time curves for the 3 and 6 J impact energy levels of the composites under analysis. The first thing to notice is the shape of the curves, which closely resemble the typical curve obtained for a large-mass impact, as previously explained in sub-section 2.2.3.3. It is possible to understand that with an increase in impact energy, there is a corresponding increase in the peak impact forces, and the oscillations exhibit greater amplitude, resulting in more significant damage to the laminates. Initially, the impact force experiences gradual and fluctuating growth until it reaches its peak. These initial oscillations occur due to elastic waves and vibrations generated in the specimens upon impact [126]. Subsequently, as the impactor rebounds, the curves become smoother, and the impact force gradually decreases until zero.

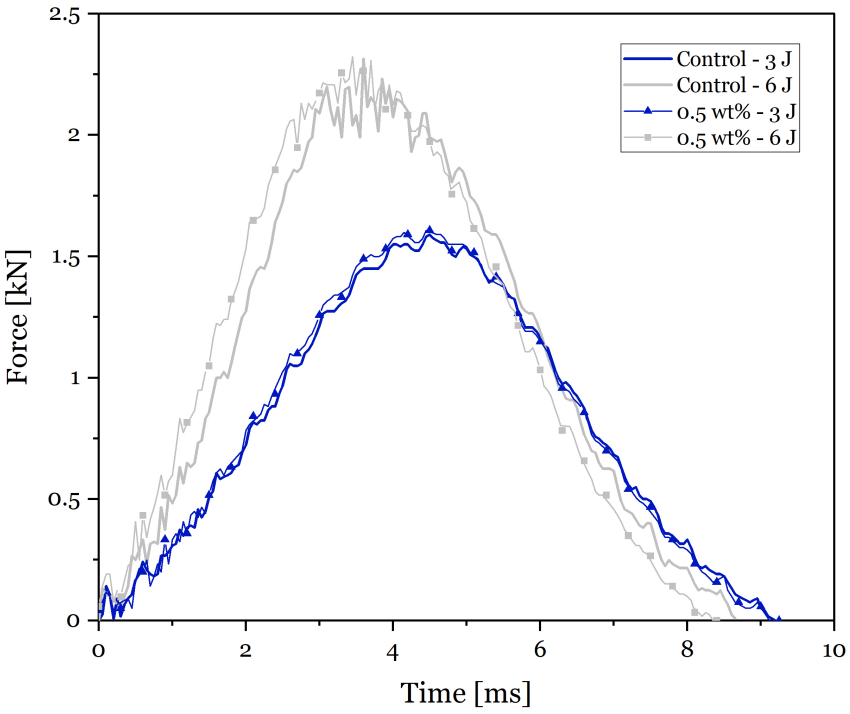

Figure 4.5: Representative force-time curves from low-velocity impact tests.

For the 3 J impacts, both curves show very identical behavior. There are no sudden changes in impact force, and the oscillations have a small amplitude, indicating that no significant damages are inflicted on the composite structure. However, more severe oscillations occur for the 6 J impact energy, mainly from t = 3 ms to t = 4.5 ms, when there are sudden and large decreases in impact forces amplitude, possibly caused by matrix damage and delaminations in the impacted region. Violent oscillations are observed near the peak force, and a sudden drop occurs with the appearance of fiber breakage [127]. After the impact force reaches its peak, fluctuations in these curves decrease gradually after roughly 1 ms. The impactor starts to rebound, and the impact curves become relatively smooth. Finally, the impact force vanishes when the impactor and sample completely separate.

Moreover, the representative force-time curves shown in Figure 4.5 reveal noteworthy information regarding the impact duration of the LVIs. Notably, the 3 J impact has a slightly lower impact velocity (1.46 m/s), maintaining contact with the composite for a longer period, having a total impact duration of approximately 9 ms, with the peak force occurring at around 4 ms. In contrast, the 6 J impact, delivering twice the energy, imparts a higher impact velocity (2.06 m/s), leading to a shorter total impact duration of roughly 8.5 ms, with the peak force occurring earlier in the process, approximately 3.5 ms. This difference may look insignificant (0.5 ms for both peak and total impact duration), but it underscores the significant influence of impact velocity on total impact duration and peak force timing, providing valuable insights into the composite material's dynamic response to varying energy levels.

Table 4.4: Low-velocity impact test results.

Specimen	**Energy [J]**	**Absorbed Energy [J]**	**Peak Force [kN]**	**Max. Displacement [mm]**
Control	3	1.19 ± 0.01	1.59 ± 0.004	4.68 ± 0.04
	6	3.10 ± 0.01	2.30 ± 0.06	6.01 ± 0.04
0.5 wt%	3	1.21 ± 0.01	1.61 ± 0.004	4.58 ± 0.10
	6	3.22 ± 0.07	2.32 ± 0.08	5.60 ± 0.05

4.2.2 External and Cross-Section Impact Damage Analysis

After the low-velocity impact response and damage characterization, visual inspections on the impacted and non-impacted surfaces of the composites were performed, along with a cross-section analysis of the impacted specimens. This was carried out to better assess how the resulting damages corresponded to the theoretical concepts and previous analyses, thereby providing valuable insights into the alignment between experimental observations and anticipated behaviors.

By analyzing the 3 J impact on the control specimen, a slight but noticeable indention on the impacted surface can be seen in Figure 4.6a. The non-impacted surface, where the most serious damage from the impact event arises, reveals damage inside the composite structure, corresponding to delamination (Figure 4.6b). These observations follow the descriptions given in sub-section 2.2.3.2, as the delamination has a rounded shape appearance, affecting a larger area than the initial indentation and propagating toward the bottom (non-impacted surface).

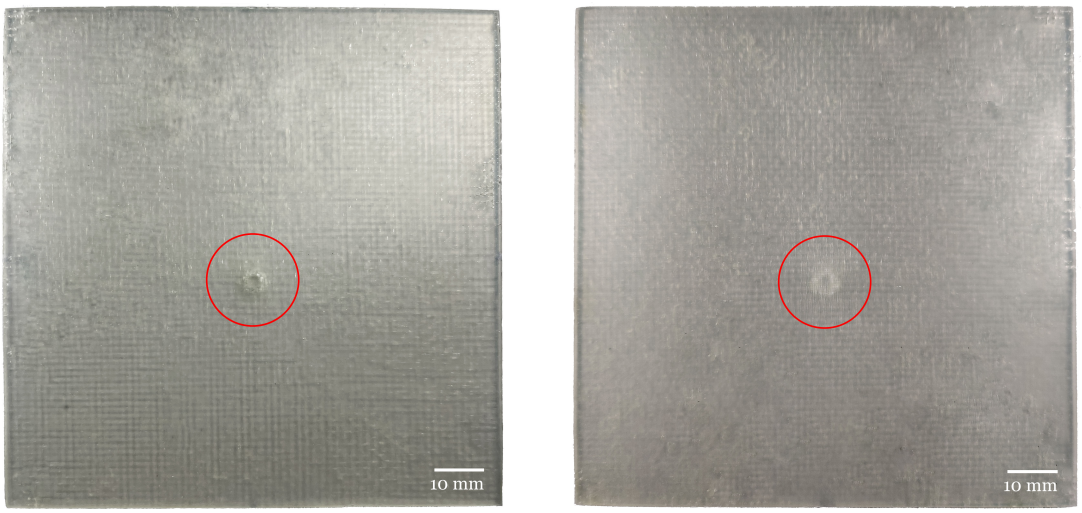

(a) (b)

Figure 4.6: External damage on control specimen after a 3 J impact energy: (a) impacted surface; (b) non-impacted surface.

On the other hand, the 6 J impact energy on the control laminate shows significant damage on the impacted surface, revealing a larger indentation area (Figure 4.7a). As expected, the non-impacted surface reflects a higher degree of damage on the laminate, mainly when compared to the 3 J impact energy. As shown in Figure 4.7b, the non-impacted surface displays the typical failure attributed lay-up of bi-directional woven fabric composites, known as the four-sided pyramidal fracture, involving significant matrix cracking and fiber breakage [128].

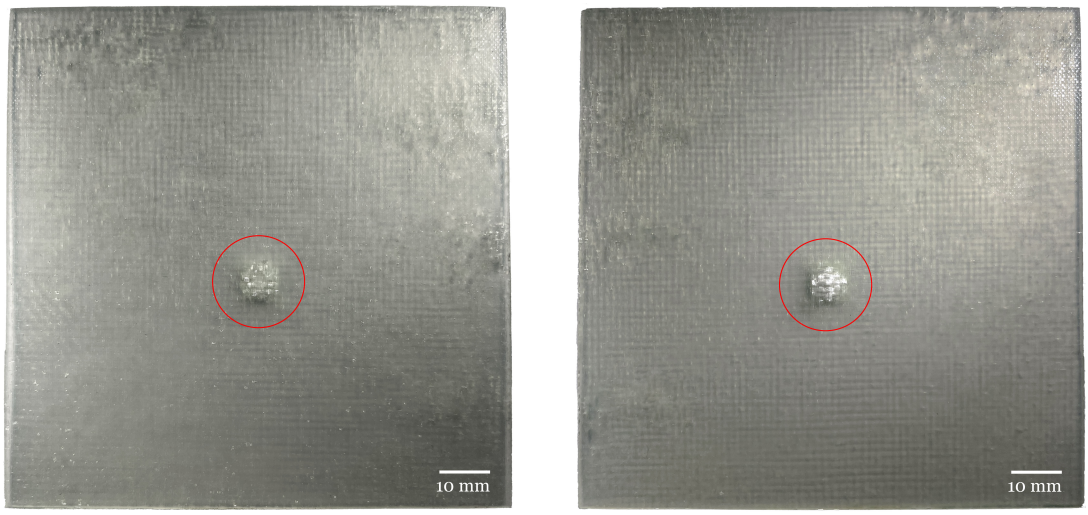

(a) (b)

Figure 4.7: External damage on control specimen after a 6 J impact energy: (a) impacted surface; (b) non-impacted surface.

For the composites containing 0.5 wt% of MWCNTs, barely visible impact damage occurs for the 3 J impact. On the impacted surface (Figure 4.8a), it is extremely difficult to perceive any indentation indicative of a low-velocity impact, and on the non-impacted one (Figure 4.8b), there is practically no visible damage to the composite structure. An important fact to note is that, unlike the translucent control laminates that allow for better identification of damages on the composite, the inherent black color of the MWCNT-enhanced composite makes the detection of low-velocity impact damages even harder.

(a) (b)

Figure 4.8: External damage on MWCNT-enhanced specimen after a 3 J impact energy: (a) impacted surface; (b) non-impacted surface.

Following the behavior previously described for the control specimens, the 6 J impact on the MWCNT-enhanced laminates led to a significant indentation in the impacted surface, resulting from the higher impact energy level. Additionally, in the non-impacted surface, matrix cracking and fiber breakage associated with the four-sided pyramidal fracture can be easily identified due to the contrast caused by the color of the specimen.

(a) (b)

Figure 4.9: External damage on MWCNT-enhanced specimen after a 6 J impact energy: (a) impacted surface; (b) non-impacted surface.

Besides the external visual inspection, a cross-section analysis was also performed to evaluate the damages within the impacted specimens. The Struers Accutom-2 cutting machine was used to cut the specimens precisely in the middle of the impacted area, and special care was taken to avoid inducing additional damage to the composite structure. After cutting, both control and MWCNT-enhanced specimens were observed under the Nikon SMZ-2T optical microscope. Once the epoxy and the glass fibers have a translucent appearance, evaluating and identifying impact damages on the control laminates was extremely difficult due to the lack of color contrast between the two components. For this reason, a cross-section analysis of the control specimens was not possible. Nevertheless, the specimens containing MWCNTs offered a clear view of the internal damage caused to the composite after impact.

By observing the cross-section cut of the 3 J impacted specimen given in Figure 4.10, no significant internal structure damage can be found. The absence of pronounced damage modes, such as matrix cracks, delaminations, or catastrophic fiber failure, is in accordance with the conclusions drawn in sub-section 4.1.2. Apart from the slight indentation on the top surface, slight damage is visible on the rear surface of the composite, with minor development of fiber breakage, suggesting that the composite maintained much of its structural integrity.

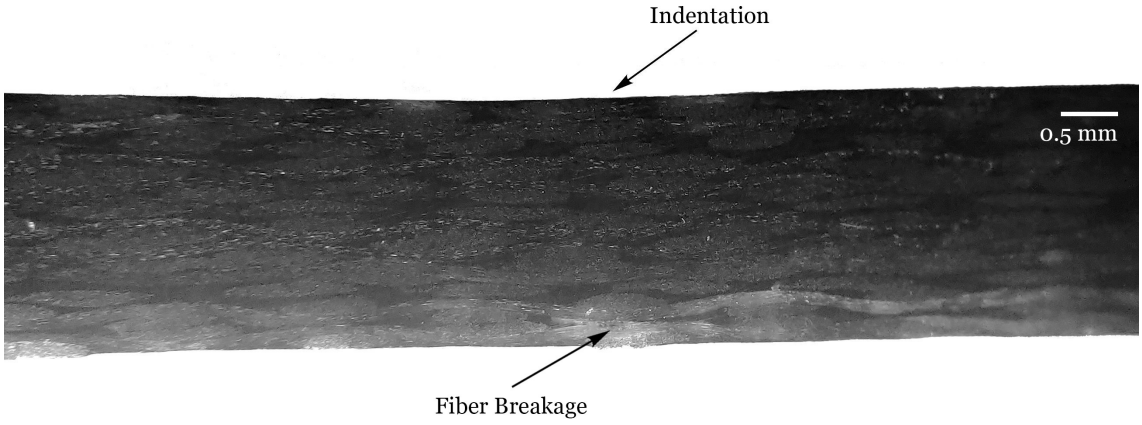

Figure 4.10: Optical microscopic image of a cross-section cut from a MWCNT-enhanced specimen after a 3 J impact. Magnification of 20×.

A completely different scenario is registered on the specimen subjected to 6 J impact. The previous external visual inspection had already revealed the presence of significant damages indicative of severe internal damages, and the cross-section analysis shown in Figure 4.11 confirms the existence of various impact-related damages within the composite structure. The first thing that stands out by analyzing the cross-section view is that LVI damage develops in a typical ”pine-tree” pattern, commonly associated with low-velocity impacts in FRP composites [10]. Apart from the much deeper indentation, there is evidence of all the main impact-related damages in the specimen's structure. It is possible to identify shear cracks, characterized by the 45° angle relative to the impacted surface, and bending cracks. The latter ones are predominant in the lower plies due to excessive transverse deflection as a consequence of the small thickness of the laminate [57].

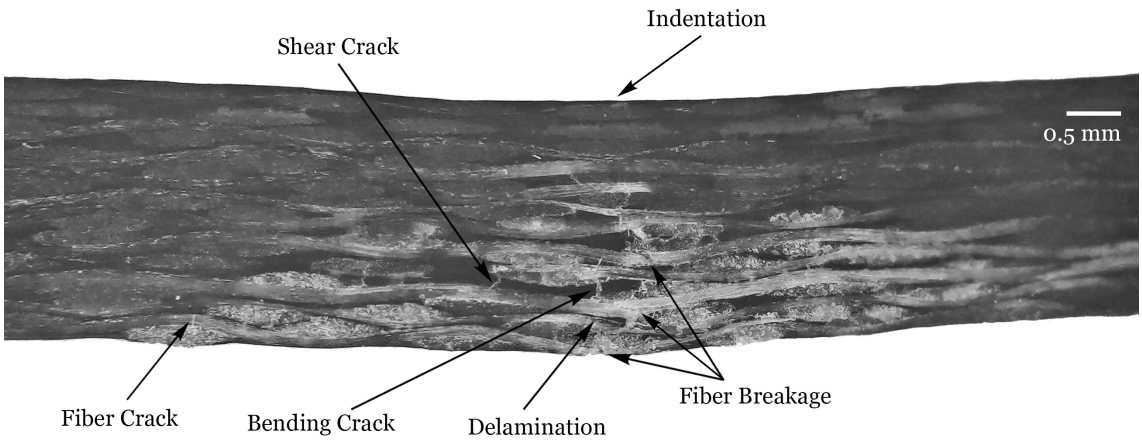

Figure 4.11: Optical microscopic image of a cross-section cut from a MWCNT-enhanced specimen after a 6 J impact. Magnification of 20×.

It is also possible to find considerable fiber breakage in the non-impacted surface and its vicinities. This damage occurs due to local tensile forces and is located near significant matrix cracks. The high incidence of fiber breakage is explained by the larger deflections (prominent in thin laminates) and the fibers' woven configuration. The fibers' inherent interlacing causes kinks at the cross-over locations, resulting in a concentration of stresses that potentiates breakage [73, 74].

The presence of significant delaminations is not very noticeable from the cross-section view in Figure 4.11. A closer look into the optical microscopic image can identify minor damage resembling delamination near a transverse matrix crack in the lower layers of the composite. As stated, the lower plies are susceptible to the formation of bending cracks that reach the matrix/reinforcement interface and cause delamination due to the stress concentration at their crack tips [66]. Various factors can explain the absence of widespread delamination. Firstly, the layers are all stacked in the same orientation, reducing their stiffness mismatch and mitigating the development of delaminations [70]. Secondly, as the specimen has a small thickness, it will absorb energy mainly through intralaminar damage, which explains the prominence of fiber breakage and cracks [84]. Finally, The impact load sustained by the composite may fall below the critical load threshold required to initiate delamination propagation within the material.

Even though a comparative study between the damage on the cross-section of the control and MWCNT-enhanced specimens was not made possible, this analysis was fundamental to understanding the effects of LVI on the composite structure. As the impact energy increased from 3 to 6 J, a discernible transformation was observed in the composite structure. What initially manifested as a BVID with minimal internal damage evolved to a clearly visible impact damage characterized by significant damage to the internal structure. This evolution in the damage profile underscores the profound influence of varying impact energies on the composite's structural integrity. It is important to note that the 6 J impact, which has been experimentally tested, could easily occur in a real-life situation. For instance, when performing maintenance on an aircraft composed of FRP composite structures, if a technician accidentally drops a torque wrench, which alone can weigh around 700 g, from a height of just over a meter, the impact on the composite structure would already be higher than 6 J. If the mechanic is unaware of the damage caused to the structure, the aircraft could enter service with severe internal damages, similar to those shown in Figure 4.11. Those same damages have the potential to develop into even more severe damages over time, which can have catastrophic consequences. As such, this is one of the main reasons why developing self-sensing composite structures capable of continuously detecting and monitoring internal damage is so important.

4.3 Electrical Resistance Measurements and Piezoresistivity

4.3.1 Specimens Electrical Conductivity

Before starting the piezoresistive characterization of the MWCNT-enhanced composites, DC electrical conductivity measurements were conducted. This assessment sought to establish the baseline electrical conductivity of the specimens under zero-load conditions, meaning that no mechanical strain was being applied. Following the experimental procedure detailed in sub-section 3.4.3, the specimens containing 0.5 wt% of MWCNTs registered a mean volumetric conductivity value of $1.5 \times 10^{-4} \pm 9.7 \times 10^{-5}$ S/cm. It is of paramount significance to note that this value is consistent with the established range of conductivity values reported in the literature, especially concerning MWCNT-enhanced GFRP composites [105, 108, 109]. The alignment with existing findings underscores the promising application of the MWCNT-enhanced composites as self-sensing materials. As such, the following sub-section will be dedicated to evaluating the structural health monitoring capabilities of the composites under different types of mechanical loads.

4.3.2 Piezoresistive Sensing

4.3.2.1 Monotonic Flexural Loading

In this section, failure tests were conducted to assess the self-sensing capabilities of the specimens containing 0.5 wt% of MWCNTs under monotonic flexural loading. The results concern the mechanical loading (i.e., flexural stress), on the left vertical axis, plotted against the flexural strain. Simultaneously, the normalized change of electrical resistance $\Delta R/R_0$ is plotted on the right vertical axis, where R_0 is the steady-state electrical resistance of the material without applying any strain (i.e., $\varepsilon_f = 0$), and ΔR is the instantaneous change in electrical resistance (i.e., $R - R_0$). Herein, a direct relationship between the two plotted parameters can be observed. It is important to note that the data plotted on the right vertical axis, relating to $\Delta R/R_0$, is in decreasing order to better perceive the correlation between the electrical and the mechanical response.

Firstly, the piezoresistive behavior of the non-impacted specimens was evaluated, as depicted in Figure 4.12. From the given plot, two different operating regions can be identified, as previously mentioned in section 4.1. The elastic region corresponds to the lower strain levels, up to approximately 1.5 % relative to the rest position. In this region, $\Delta R/R_0$ increases linearly with strain, which can be attributed to the elastic behavior of the composite. For strain levels greater than 1.5 %, $\Delta R/R_0$ shows a non-linear behavior, associated with damage initiation within the composite.

As strain increases, slight fluctuations happen during the phase that precedes the failure of the specimen, associated with a gradual development of damage inside the composite structure. These fluctuations in $\Delta R/R_0$ are indicative of the evolving nature of damage inside the composite structure. The material experiences crack formation, fiber failure, and other damage mechanisms that collectively contribute to these fluctuations. At around 3 % of strain, catastrophic failure of the specimen is observed, which discontinues the electrical measurements and leads to the specimen's collapse, resulting in an abrupt increase of electrical resistance due to the complete breakage of the conductive network. From Figure 4.12, it is also noteworthy that the self-sensing composite exhibits a negative piezoresistive behavior. Negative piezoresistivity happens when the electrical resistance decreases as strain increases, whereas positive piezoresistivity features an increase in electrical resistance as strain increases. As previously mentioned in sub-section 2.3.2, the piezoresistive behavior of a self-sensing composite based on the incorporation of MWCNTs in an epoxy matrix depends on various factors, including the position of the electrodes, MWCNTs morphology, MWCNTs concentration and dispersion within the matrix, the interactions between polymer chains and MWCNTs, the Poisson's ratio of the materials, mechanical and rheological characteristics of the matrix, CNTs intrinsic piezoresistivity, and type of loading [88]. As such, the prediction and analysis of the piezoresistive behavior can be complex as it depends on the intricate combination of those factors.

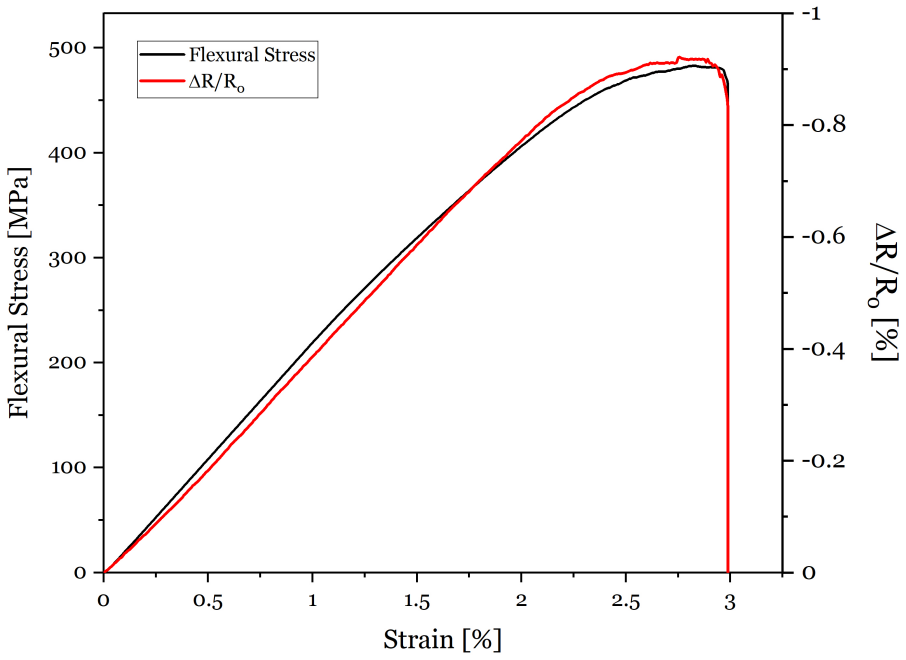

Figure 4.12: Representative piezoresistive curve of non-impacted specimens under monotonic flexural loading.

Unlike a surface measurement, where the piezoresistive behavior depends mainly on the arrangement of the MWCNT network in the specific surface where the electrodes are mounted, a volumetric measurement captures the influence of many electro-mechanical phenomena happening throughout the composite structure. Under a 3PB test, the specimen experiences an inflection, giving a curvature according to an arc of circumference generated by the bending moment. Following the inflection, it is possible to divide the specimen into two distinct zones. One is located above the neutral plane, and the other is below the neutral plane, whereas the neutral plane defines the surface where the MWCNT network remains undeformed. According to the observations reported by Luo *et al.* [129], the Poisson effect explains the existence of different piezoresistive responses under flexural loading. Based on their findings, the MWCNT network above the neutral plane is under compression in the longitudinal direction and under tension in the transverse direction. The transverse tension is predominant over the longitudinal compression, causing the MWCNTs to distance from each other, increasing the electrical resistance (positive piezoresistivity). On the other hand, the MWCNT network below the neutral plane is under tension in the longitudinal direction and compression in the transverse direction. In this case, the compression in the transverse direction predominates over the longitudinal tension, promoting contacts and shortening distances between the MWCNTs, resulting in a decrease in electrical resistance (negative piezoresistivity). It can be concluded that the representative piezoresistive curve given in Figure 4.12 corroborates the influence of the Poisson effect on the piezoresistive response of the MWCNT-enhanced composites, especially the predominance of the compression in the transverse direction below the neutral plane of the composite, hence the negative piezoresistivity.

To assess the piezoresistive sensitivity of the non-impacted specimens under flexural loading, the GF was calculated as the slope of the linear-elastic strain region (0.25 % $\leq \varepsilon_f \leq$ 1 %) of the piezoresistive curves, and the mean value obtained for the GF was -0.40 ± 0.01. The measured GF value is slightly lower than the one reported by Rodríguez-González *et al.* [130], which for a 0.5 wt% content of spray-coated MWCNTs in GFRP composites, reported a GF value of approximately 1.5 under flexural loading tests. However, Vertuccio *et al.* [100], which investigated the piezoresistive response of an aeronautical epoxy resin filled with 0.3 wt% of MWCNTs under axial and flexural stress, reported different results. The DC characterization conducted under tensile stress revealed a linear piezoresistive response with a GF of 0.43. In contrast, the flexural stress showed a non-linear response, with a GF value falling below 0.1. However, the AC characterization performed at a frequency of 1 MHz showed a linear behavior for both tensile and flexural tests, with the GF improving significantly to 0.6 and 1.28 for tensile and flexural loading, respectively.

In this particular case, while the GF of -0.40 obtained from the DC measurements carried on the self-sensing composites may not be exceptionally high, it reveals to be a satisfactory result, not only because it provides a higher sensitivity compared to investigations with similar manufacturing procedures, but because it also registers a linear DC piezoresistive response, which, in the case of Vertuccio *et al.* [100], is only achievable through an AC

measurement. Nevertheless, it is important to note that the GF value must be evaluated from an absolute value perspective. The sign (positive or negative) of the GF merely reflects the direction of resistance change, whether it increases or decreases with strain. For assessment purposes, what must be considered is the magnitude of the GF, i.e., a higher absolute GF value means greater sensitivity, regardless of the direction of the resistance change.

Monotonic flexural tests were also performed to evaluate the low-velocity impact influence on the self-sensing composites' piezoresistive response. Figure 4.13 depicts the representative piezoresistive curve after a 3 J energy impact. Similarly to the behavior registered for the non-impacted case, the $\Delta R/R_0$ increases linearly with strain in the elastic region, corresponding to strain levels up to approximately 1.25 %. Despite the linear response, the $\Delta R/R_0$ curve is not as smooth as in the non-impacted state and evolves with minor but visible oscillations. This behavior indicates the presence of microcracks caused by the 3 J impact, which disrupts the conductive network's electric flow, resulting in a noisy electrical signal. As strain increases, a non-linear response is registered for strain levels within the plastic region. This phase is a critical period where the composite undergoes progressive degradation, and the behavior of the $\Delta R/R_0$ becomes more erratic and unpredictable. In the moments that precede the complete failure of the composite, higher amplitude oscillations can be seen due to significant matrix cracking, fiber failure, and crushing under the load nose [131].

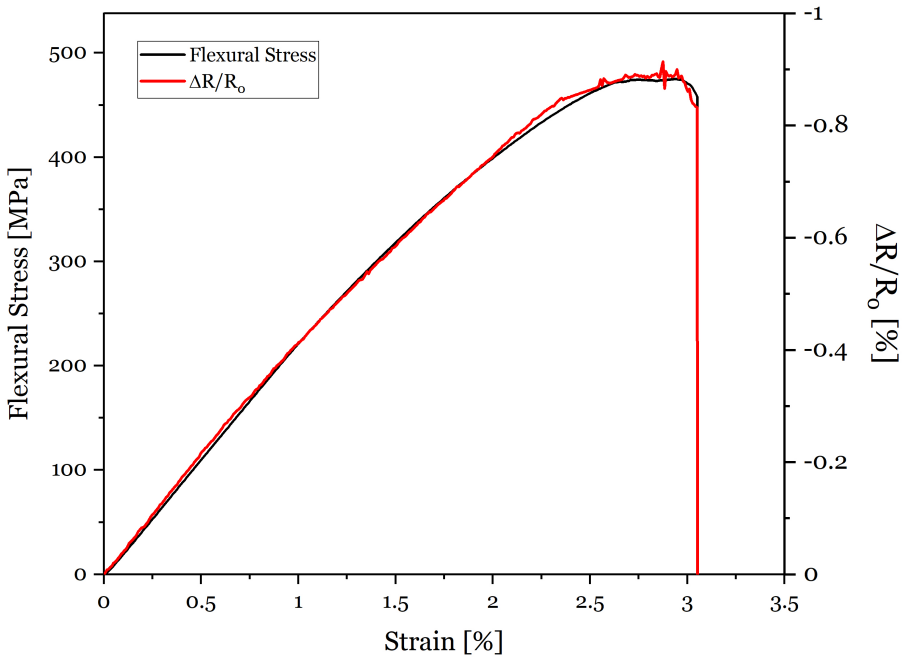

Figure 4.13: Representative piezoresistive curve of 3 J impacted specimens under monotonic flexural loading.

The same negative piezoresistive behavior is observed after the 3 J impact, and, as expected, an abrupt increase in electrical resistance is seen slightly above 3 % of strain as a result of the specimen failure. Post-impact piezoresistive sensitivity was also evaluated, and the GF was calculated in the same linear-elastic strain region as for the non-impacted specimens. A mean value of -0.37 ± 0.06 was obtained, registering a slight decrease of 7.5 % relative to the non-impacted state. This means that the 3 J impact, while not causing severe internal damages to the internal composite structure, is sufficient to disrupt the MWCNT conductive networking, resulting in a piezoresistive response with decreased sensitivity.

To complete the post-impact piezoresistive response under monotonic flexural loading, tests were conducted on the 6 J impacted specimens. As demonstrated in Figure 4.14, the initial phases of the representative piezoresistive curve exhibit a close alignment with the mechanical response curve, displaying a linear correlation. However, a noteworthy deviation in $\Delta R/R_0$ from the flexural curve becomes evident at approximately 0.5 % of strain, preceding the specimen's entry into the plastic deformation regime. In other words, before the material undergoes irreversible plastic deformation, there is already a significant change in the electrical resistance of the material. This change in $\Delta R/R_0$ does not follow the changes in physical deformation as expected from the mechanical response curve, suggesting that the changes in the material's electrical properties do not directly correspond to its physical deformation. This discrepancy in behavior is of significant importance, as it suggests that factors beyond mechanical strain, potentially stemming from the internal damages caused by the impact, might be influencing the material's electrical response.

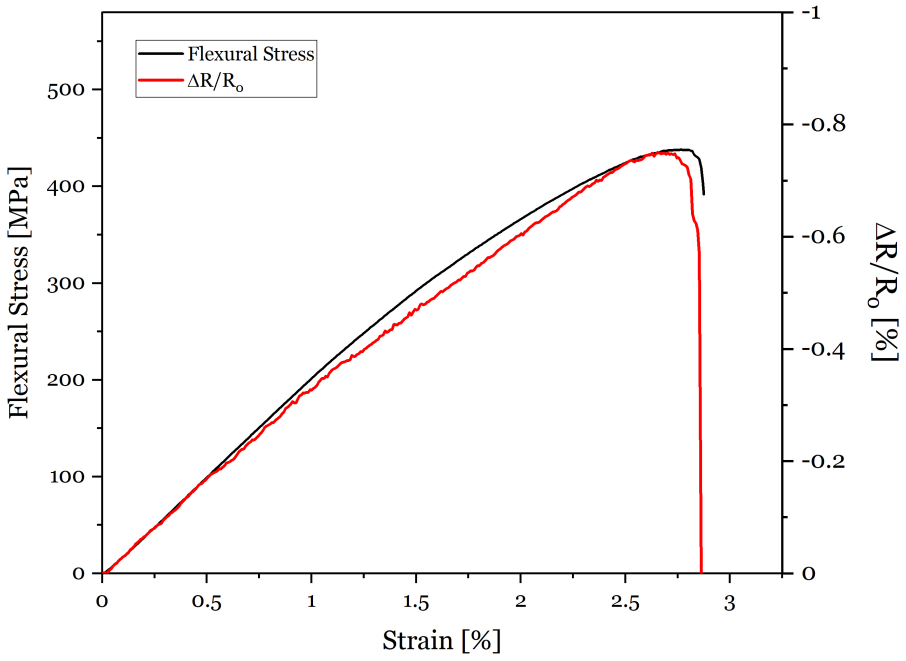

Figure 4.14: Representative piezoresistive curve of 6 J impacted specimens under monotonic flexural loading.

As seen in the cross-section view cut from Figure 4.11, the specimen subjected to a 6 J impact energy reveals severe internal damages, such as intralaminar cracks, matrix cracks, and fiber breakage. These damages significantly influence the piezoresistive response, causing disturbances to the flow of electrical current, originating a very wavery and noisy electrical signal. These oscillations happening throughout most of the elastic and plastic regions are more pronounced than those registered for the 3 J impacted specimens, indicating the presence of significant damages opposing the flow of electrical current. Furthermore, in contrast to the piezoresistive response after the 3 J impact, no visible large amplitude oscillations are observed near the ultimate failure point. Instead, a discernible rise in electrical resistance is detected, characterized by the descending trend of the $\Delta R/R_0$ curve. This occurrence transpires earlier in the loading process than the mechanical failure of the composite. The early increase in electrical resistance is attributed to the premature rupture of the conductive network, as a consequence of the extensive damages inflicted by the 6 J impact. Essentially, this implies that well before the specimen experiences complete structural failure, the integrity of the conductive network is already severely compromised, resulting in an earlier than anticipated escalation of electrical resistance.

In the context of evaluating the piezoresistive sensitivity of the 6 J impacted specimens, the GF was determined within the same strain region as in the previous cases. The mean calculated GF value was recorded as -0.30 ± 0.02. This measurement represents a noteworthy 25% decrease compared to the non-impacted specimens and a 19% decrease compared to the 3 J impacted specimens. A deeper analysis of the results reveals that the loss in piezoresistive sensitivity more than tripled by doubling the impact energy from 3 J to 6 J. The substantial reduction in piezoresistive sensitivity reflects, once again, the influence of the damages inflicted by the 6 J impact, which significantly disrupts the MWCNT electrical conductive network, compromising the piezoresistive response of the self-sensing composites.

In sum, the aforementioned observations have provided valuable insights into the piezoresistive capabilities of self-sensing composites containing 0.5 wt% of MWCNTs. The experiments have unveiled a first glimpse of the composite's innate ability to respond sensitively to flexural strain under monotonic loading conditions. From the collected data, it becomes evident that the integration of MWCNTs within the epoxy matrix leads to pronounced and consistent changes in electrical resistance, aligning with the imposed mechanical deformations. This outcome not only demonstrates the effectiveness of the self-sensing mechanism but also underscores the potential for real-time monitoring of structural integrity under different mechanical loads (e.g., cyclic loading and low-velocity impacts), as it will be further investigated.

4.3.2.2 Cyclic Flexural Loading

In addition to the monotonic strain sensitivity, the stability and repeatability of the self-sensing composites, both before and after impact, were evaluated. To do so, the specimens were subjected to five constant amplitude loading–unloading flexural cycles within the elastic region to verify their piezoresistive response in real service conditions. For all the cyclic loading-unloading tests, the maximum flexural strain was set to 1.5 %. The results concern the flexural strain (left vertical axis) and normalized change of electrical resistance $\Delta R/R_0$ (right vertical axis) as a function of time. Similar to the monotonic flexural tests, the data plotted on the right vertical axis is in decreasing order for a clearer perception of the correlation between the electrical and the mechanical response.

Similar to the experiments conducted under monotonic flexural loading, the assessment of the cyclic piezoresistive behavior started with the non-impacted specimens to establish a baseline for comparative analysis with the impacted counterparts, enabling a comprehensive understanding of the material's response to cyclic loading. As depicted in Figure 4.15, the observations indicate that the variations in electrical resistance exhibited a direct and clean correspondence with the applied strain. Importantly, it is notable that the peak resistance values achieved at each deformation level remained remarkably consistent across multiple mechanical cycles. Furthermore, a particularly noteworthy characteristic of the piezoresistive behavior is that, after each cycle, the material's electrical resistance returned to its initial state, meaning that the electrically conductive network could be basically reset.

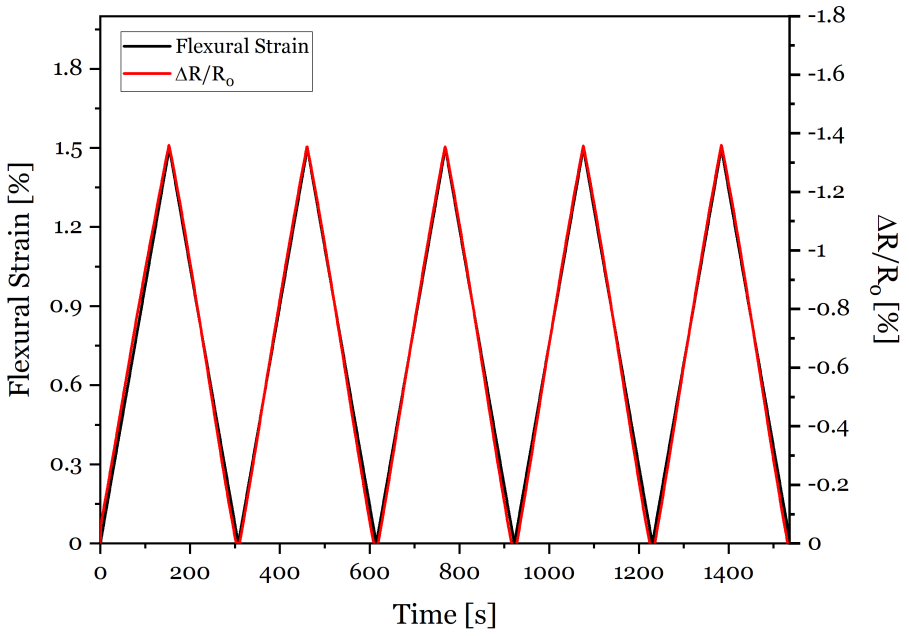

Figure 4.15: Representative piezoresistive curve of non-impacted specimens under cyclic flexural loading.

The consistent electro-mechanical pattern and the reversible behavior throughout the successive mechanical cycles offer valuable insights into the material's self-sensing capabilities and structural integrity. These observations are significant, especially in applications where materials must endure cyclic loading conditions, such as structural components in aerospace engineering. It indicates that, within the observed strain range and cyclic loading conditions, the composite remains structurally intact and capable of accurately and reliably sensing mechanical deformations without suffering long-term damage or irreversible changes in its conductive properties.

Post-impact cyclic flexural tests were performed under the same conditions as the non-impacted specimens to evaluate the influence on the piezoresistive response repeatability after a LVI. From the representative piezoresistive curve given in Figure 4.16, it is possible to conclude that after a 3 J impact, the piezoresistive response reveals signs of degradation. While there is still a linear correlation between the change in electrical resistance and applied strain, a slight deviation in $\Delta R/R_0$ from the strain curve is perceptible. This deviation is particularly pronounced in subsequent cycles, signifying an escalation in the discrepancy between the electrical and mechanical responses. The root of this amplified deviation can be traced back to the structural alterations and damage inflicted by the 3 J impact, which affects the self-sensing specimen's long-term performance, its capacity to sustain repeatability, and its durability under cyclic loading.

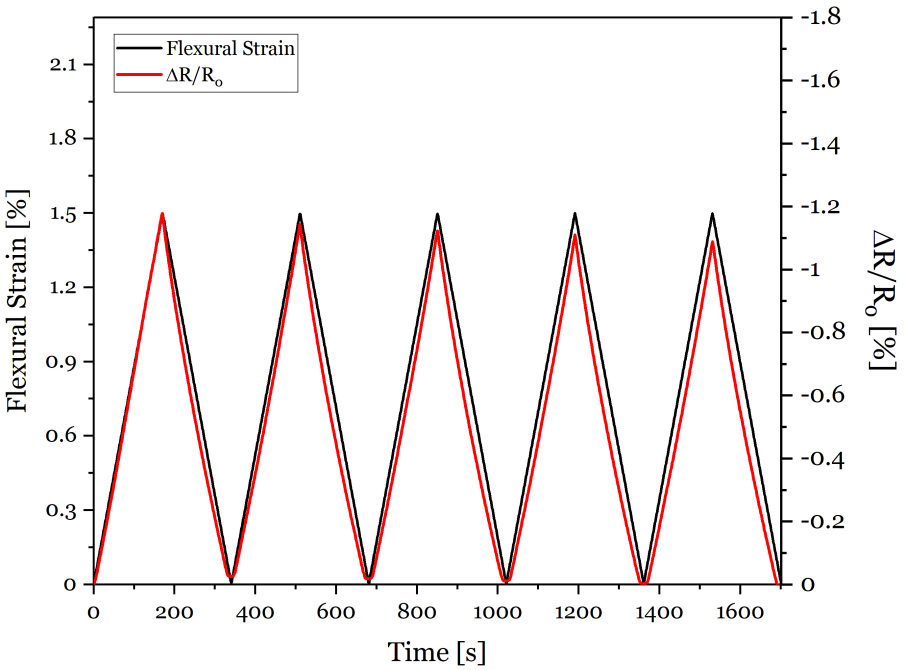

Figure 4.16: Representative piezoresistive curve of 3 J impacted specimens under cyclic flexural loading.

Furthermore, the peak resistance demonstrates a gradual decline after each cycle, indicative of irreversible deformation occurring within the MWCNT network. A deep analysis shows that, at the fifth cycle, the peak normalized resistance dropped by 7.6 % compared to the peak value reached in the first cycle. This phenomenon can be attributed to the formation of microcracks within the electrically conductive matrix following the LVI. These microcracks have the potential to propagate further due to the repeated opening and re-opening during the cyclic loads, ultimately disrupting the conductive pathways established by the MWCNTs within the epoxy matrix. Consequently, with each cycle, a progressive accumulation of damage occurs within the conductive matrix, leading to a permanent loss of piezoresistive sensitivity. A very slight residual resistance is also registered at the end of the first two cycles. However, in the remaining cycles, the electrical resistance returned to its initial state, meaning that the 3 J impact did not affect the resetting of the electrically conductive network upon unloading.

Finally, cyclic flexural testing of the 6 J impacted specimens was conducted, and the representative piezoresistive curve, depicted in Figure 4.17, underscores noteworthy insights. Firstly, a consistent linear correlation between the normalized electrical resistance curve and applied strain is registered, indicating a degree of resilience within the electrically conductive network's ability to monitor strain after a 6 J impact. However, telltale signs reveal a loss of effectiveness regarding the accurate strain sensing of the specimens.

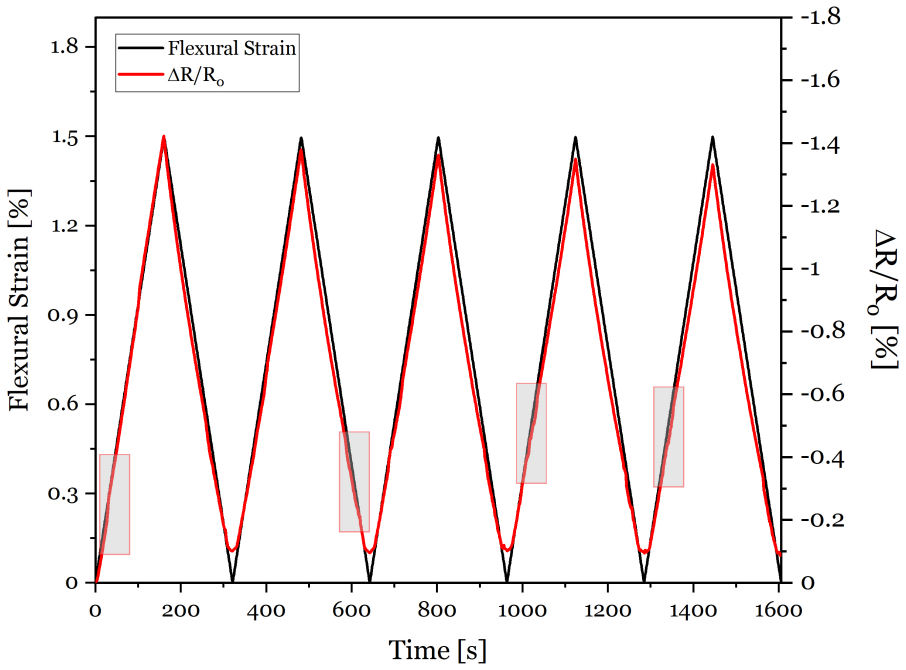

Figure 4.17: Representative piezoresistive curve of 6 J impacted specimens under cyclic flexural loading.

As seen in Figure 4.17, the electrically conductive network fails to return to its initial state throughout the entire loading-unloading cyclic process. A residual resistance of around 0.1 % is clearly visible at the end of each cycle, meaning that the MWCNT conductive network lost the ability to reset. This finding marks a distinctive departure from the behavior of non-impacted and 3 J impacted specimens, indicating a substantial loss of strain-sensing capability due to the more severe damage inflicted by the 6 J impact.

Similar to the observations regarding the 3 J impacted self-sensing specimens, a deviation between the normalized electrical resistance change and the strain curve occurs, and the peak resistance also shows a gradual decline, with the last cycle registering a notable 6.5 % decrease compared to the peak $\Delta R/R_0$ value reached at the first cycle. Additionally, during the loading-unloading cycles, there is the formation of "shoulders" on the normalized electrical resistance curve, identified by the gray squares in Figure 4.17. Despite being very subtle, these so-called "shoulders" reflect the reorganization of the conductive pathways formed by the MWCNTs within the composite, emphasizing the material's evolving response under cyclic loading conditions [132].

A noteworthy observation is that, for the cyclic tests, the changes in electrical resistance within the 1.5 % strain range are higher than those registered for the monotonic flexural tests. At 1.5 % of flexural strain, the peak normalized resistance was between -1.4 and -1.2 % for the cyclic tests, whereas for the same value of strain, the $\Delta R/R_0$ was between -0.6 and -0.4 % for the monotonic tests. Given that both monotonic and cyclic tests were conducted under the same conditions (e.g., displacement rate, span length) and all the specimens had the same geometry, this phenomenon is unexpected. This phenomenon, although unexpected, may be attributed to differences in MWCNT dispersion and arrangement within the epoxy matrix, possibly linked to variations arising from the use of specimens sourced from different plates.

4.3.2.3 Low-Velocity Impact

The results previously obtained from the monotonic and cyclic piezoresistive tests revealed remarkable strain sensing and damage monitoring capabilities. These promising results have laid the foundation for the research conducted in this section, which is, in its essence, the culmination of the work conducted thus far. Herein, the primary focus is evaluating the self-sensing composite's piezoresistive capabilities to enable real-time detection of low-velocity impacts on composite structures.

Figure 4.18 depicts the time-dependent behavior of normalized electrical resistance change in response to low-velocity impacts with energies of 3 J and 6 J, applied to the self-sensing composites. It is clearly observed that when an instantaneous impact load is imposed, the $\Delta R/R_0$ of the specimens increases abruptly, reaching a peak value before gradually decreasing to a certain stabilization level. The abrupt increase in electrical resistance directly results from the disruption incurred in the MWCNT conducting network during the impact event. This phenomenon can be attributed to the dynamic response of the self-sensing material when exposed to impact-induced mechanical deformations.

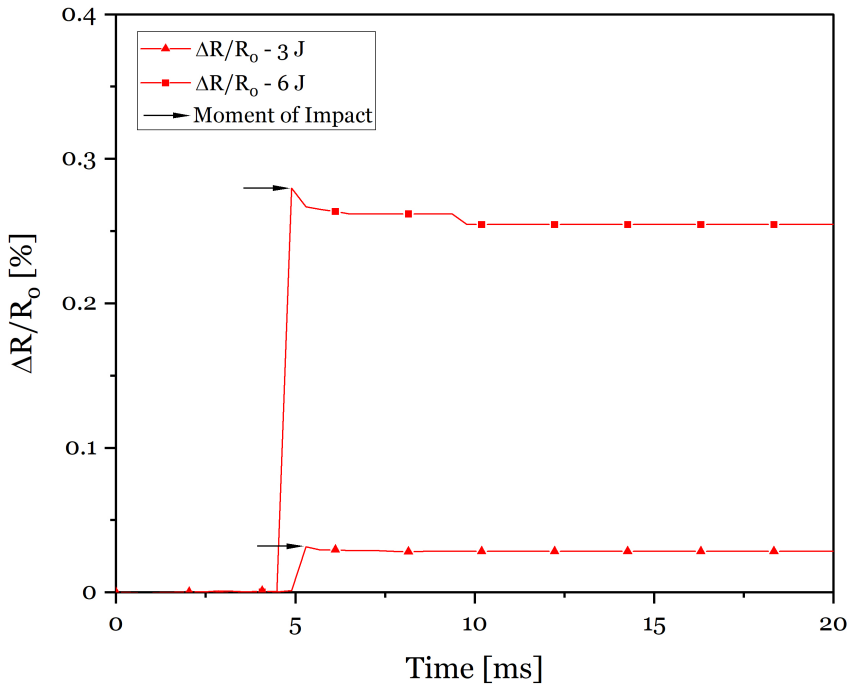

Figure 4.18: Representative change in normalized electrical resistance as a function of time for 3 J and 6 J low-velocity impacts.

The piezoresistive response obtained during the low-velocity impacts is consistent with the data reported from similar tests conducted by Gao *et al.* [106] and Al-Bahrani and Cree [109]. As expected, the peak of $\Delta R/R_0$ increased with increasing the impact energy level. For the 3 J impacts, the mean peak $\Delta R/R_0$ value obtained was 0.027 % $\pm$ 0.001, which is not a particularly significant change in normalized electrical resistance. However, a positive point from this observation is that it reveals that even at barely visible impact energy levels, the self-sensing composite is capable of detecting minor changes in the conductive network. Interestingly, for the 6 J impacts, the mean peak $\Delta R/R_0$ value reached 0.29 % $\pm$ 0.02, which is a very satisfactory result, given that for the same content of MWCNT and with double the impact energy (12 J), the peak $\Delta R/R_0$ value registered by Al-Bahrani and Cree [109] at the moment of impact was around 0.25 %.

Figure 4.19 shows a magnified view of the $\Delta R/R_0$ curves at the moment of impact for both impact energy levels. The analysis of these curves reveals valuable electro-mechanical phenomenons happening at the moment of impact. For both impact energy levels, when the impactor rebounds, part of the formed cracks close due to elastic deformation, and the MWCNTs contact is re-established, resulting in a decrease in the electrical resistance of the self-sensing specimens. After the 3 J impacts, there is a mean recovery in electrical resistance of approximately 11 % due to elastic deformation, whereas for the 6 J specimens that recovery is around 14 %. These results possibly stem from the fact that the 6 J impact causes more cracks in the conductive matrix. Consequently, there is a greater portion of electrical resistance recovery from the closure of those cracks due to elastic deformation.

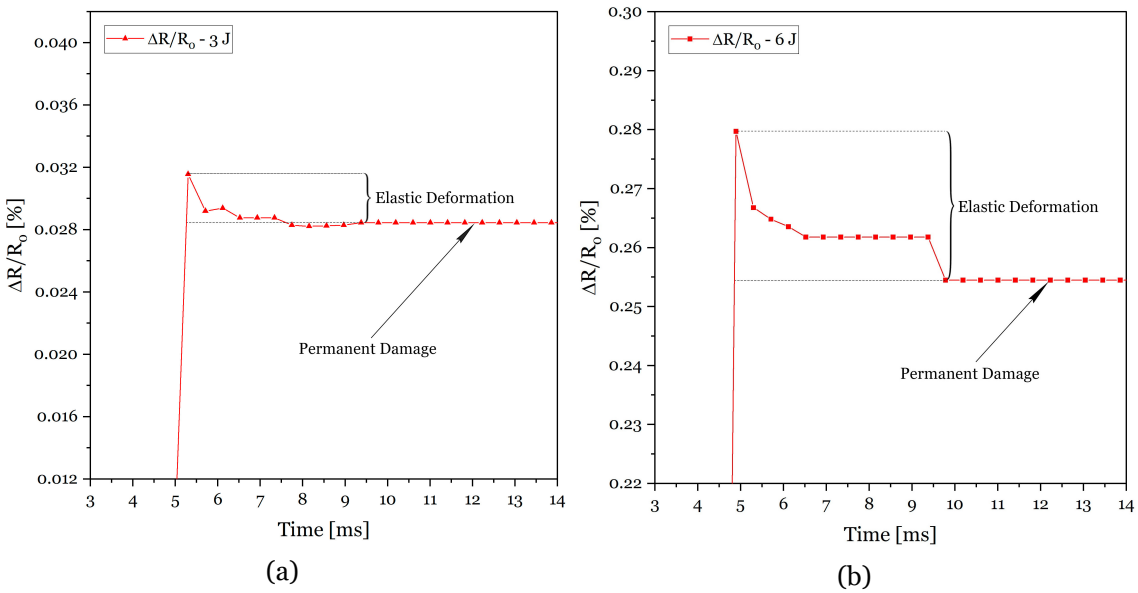

Figure 4.19: Magnified view of the representative change in normalized resistance as a function of time at the moment of impact: (a) 3 J impact; (b) 6 J impact.

Furthermore, another parameter of interest is the assessment of permanent changes in residual electrical resistance after the low-velocity impacts. After a 3 J impact, the mean $\Delta R/R0$ value at which the curve stabilizes is $0.024\ \% \pm 0.007$, whereas, for the 6 J impact, this value is $0.24\ \% \pm 0.02$. These stable points represent a distinct feature in the electrical response and are indicative of the impact's lasting effects on the self-sensing composite's electrical behavior.

As seen from the obtained results, the specimens have shown the self-sensing capabilities to monitor, in real-time, the occurrence of a low-velocity impact event. These findings open up exciting possibilities for potential applications in the aerospace industry. Specifically, the correlation between post-impact stabilization levels and varying energy inputs could be explored for full-scale aerospace components. However, such an endeavor would undoubtedly demand an extensive database and rigorous research. Nevertheless, these processes could be further accelerated and improved with the increasingly advanced computational technologies allied to the exponential growth of machine learning and artificial intelligence. With these tools, the implementation of a more efficient structural health monitoring system for FRP composites, capable of accurately gauging the impact magnitude and internal structural damages, becomes increasingly viable, representing a promising step towards enhancing the reliability and safety of aerospace structures.

Chapter 5

Conclusions and Future Perspectives

5.1 Conclusions

Following the prominence of FRP composites in high-performance applications, particularly in aeronautical and aerospace engineering, it is of paramount importance to identify possible ways to improve the in-service damage response of these materials, particularly when subjected to low-velocity impact events, which are particularly harmful to fiber-reinforced composite structures. Within this framework of thought, this dissertation aimed to develop a multifunctional GFRP composite capable of detecting, in real-time, damages created under low-velocity impact events. Therefore, a comprehensive review of structural health monitoring approaches was perceived and adopted as a jumping-off point, especially focused on the usage of CNTs as piezoresistive sensors for fiber-reinforced composites.

Once the state-of-the-art research task was considered satisfactory to proceed, efforts were dedicated to manufacturing the GFRP composites enhanced with multi-walled carbon nanotubes. A step-by-step approach was implemented, firstly by ascertaining the optimal amount of MWCNTs needed in the epoxy matrix to attain an electrically semiconductive composite, concluding that a concentration of 0.5 wt% of MWCNTs would best serve this purpose. Subsequently, the overall manufacturing process was optimized to guarantee a uniform dispersion of carbon nanotubes within the epoxy matrix.

The assessment of the mechanical properties showcased the effects of integrating multi-walled carbon nanotubes into the epoxy matrix. Notably, the GFRP specimens containing 0.5 wt% of MWCNTS showed improved mechanical performance, exhibiting superior flexural strength (480.81 MPa) and modulus (23.09 GPa). This represented a 3.25 % and 3.36 % increase in flexural strength and modulus, respectively, compared to the control samples. Evaluation of post-impact performance revealed that the MWCNT-enhanced composites had higher impact resistance, which was particularly evident after the 6 J impacts, as the specimens containing 0.5 wt% of MWCNTs demonstrated a significantly smaller reduction in flexural strength (5.4 %) compared to the control specimens (10.4 %). In addition, the MWCNT-enhanced specimens experienced a marginal reduction in failure strain of less than 1 %, whereas the control samples registered a 2.6 % reduction. Overall, the results showed that the incorporation of MWCNTs improves the post-impact flexural properties and the impact damage resistance of the composites.

Experimental findings on the mechanical response to the low-velocity impacts revealed that the composites containing 0.5 wt% of MWCNTs exhibited higher peak forces and lower maximum displacements than the control specimens. For the 3 J impacts, the MWCNT-enhanced composites displayed only a marginal increase in absorbed energy compared to the control specimens, whereas for the 6 J energy level impacts, the disparity in energy absorption became more pronounced, evidencing a 3.5 % increase in absorbed energy compared to the control samples. Moreover, the impact force-time curves showed that the total impact duration for the 3 J energy level was longer than the 6 J impact, with the peak force occurring later in the impact period.

External visual inspections following the 3 J impacts revealed a slight indentation on the impacted surface and a rounded-shaped appearance on the bottom surface of the control samples, while the specimens containing 0.5 wt% of MWCNTs showcased barely visible impact damage. Contrarily, the 6 J impacts caused more substantial damage, including a larger indentation and a four-sided pyramidal fracture on the non-impacted surface, both for the control and the MWCNT-enhanced composites. Observations of the cross-section cuts revealed minimal visible internal damage after the 3 J impacts, while the 6 J impacted specimens displayed a "pine-tree" damage pattern involving shear and bending cracks, fiber breakage, and minor delaminations.

Analysis of the DC electrical conductivity measurements determined that the MWCNT-enhanced had a baseline mean volumetric conductivity of 1.5×10^{-4} S/cm. Afterward, piezoresistive monotonic flexural tests on the MWCNT-enhanced composites unveiled a first glimpse of their ability to respond sensitively to flexural strain. The data proved that adding MWCNTs to the epoxy matrix resulted in consistent changes in electrical resistance, exhibiting linear piezoresistive behavior within the elastic regime. The assessment of the piezoresistive sensitivity revealed a GF value of −0.40 for the non-impacted specimens. Regarding the impacted specimens, the 3 J energy impacts slightly decreased the piezoresistive sensitivity (GF = −0.37), while the 6 J impacts led to a more significant reduction in the gauge factor (GF = −0.30) as a result of the severe internal damages. Notably, the MWCNT-enhanced composites were characterized by a negative piezoresistive response, which was attributed to the Poisson effect.

Additionally, the piezoresistive cyclic flexural loading tests on the MWCNT-enhanced composites revealed that the non-impacted specimens had a consistent electro-mechanical pattern during cyclic loading, demonstrating outstanding piezoresistive stability and repeatability across multiple loading cycles. However, post-impact cyclic flexural tests revealed signs of degradation in the cyclic piezoresistive response, with slight deviations in $\Delta R/R_0$ from the strain curve. Discrepancies between electrical and mechanical responses were visible as the impact energy increased, affecting the self-sensing specimen's long-term performance and durability under cyclic loading. Following the 6 J impacts, the inability of the electrically semi-conductive network to reset was evident, leaving a residual resistance at the end of each cycle.

The culmination of this research underscored the MWCNT-enhanced composite's abilities for real-time detection of low-velocity impact events. The time-dependent behavior of $\Delta R/R_0$ in response to the 3 J and 6 J low-velocity impacts showcased an abrupt increase in electrical resistance at the moment of impact, followed by a non-linear decrease until a certain stabilization level. Notably, the self-sensing composites were capable of detecting minor changes in the MWCNT semi-conductive network, with a mean peak $\Delta R/R_0$ value of 0.027 % and 0.29 % for the 3 J and 6 J impacts, respectively, highlighting their piezoresistive potential for structural health monitoring applications.

In sum, this study successfully developed and characterized a self-sensing GFRP composite enhanced with 0.5 wt% of MWCNTs to act as piezoresistive sensors for real-time damage detection of low-velocity impact events. The validation of self-sensing capabilities positions the developed composite as a multifunctional and cost-effective real-time structural health monitoring solution, offering promising prospects for aerospace and aeronautical applications, where timely and accurate damage detection is paramount.

5.2 Future Perspectives

Based on the extensive research carried out in this dissertation, several opportunities for future investigations arise to further explore the field of structural health monitoring of FRP composites for aeronautical and aerospace applications. To complement this study and create new lines of research for future works, the following topics are suggested:

- Investigate a range of MWCNT concentrations to understand their impact on the piezoresistive behavior and mechanical properties, aiming to identify an optimal concentration for specific applications.
- Explore hybridization with other nanomaterials, such as graphene nanoplatelets or graphite oxide, to assess their synergistic effects on enhancing the composite's self-sensing capabilities and mechanical performance.
- Scale up the impact energy levels to evaluate the material's performance under higher stress conditions, simulating more severe impacts to assess the upper limits of its capabilities.
- Explore alternative manufacturing methods and dispersion techniques for MWCNTs to optimize their uniform distribution within the composite, potentially enhancing mechanical and electrical properties.
- Develop a more refined data acquisition system with shorter acquisition times to capture detailed electrical resistance variations during impact events, providing a comprehensive understanding of the dynamic response.

- Conduct extended cyclic loading tests to assess the self-sensing composite's resilience to fatigue, providing insights into its long-term performance and durability under repeated mechanical stress.
- Integrate the self-sensing composite into the skin of small-scale aircraft components (e.g., wing, stabilizer) to study its mechanical behavior and low-velocity impact response in a realistic aerospace environment.
- Investigate the influence of various contact interfaces on the self-sensing capabilities, exploring different materials and conditions that the composite might encounter during its application.
- Explore the impact of diverse environmental variables, including different temperature ranges representative of aviation conditions, to assess the material's response and stability under various operational environments.
- Investigate the integration of the self-sensing composite with advanced structural health monitoring systems, exploring correlations between electrical responses and traditional structural health indicators.
- Explore the application of machine learning algorithms to analyze the complex datasets generated by the self-sensing composite, aiming for automated detection and characterization of mechanical and electrical responses.

Bibliography

[1] S. Singh, D. Kumar, and C. Prakash, **"Introduction, History, and Origin of Composite Materials**," in *Fabrication and Machining of Advanced Materials and Composites: Opportunities and Challenges*, 1st ed. Boca Raton: CRC Press, 2022, pp. 1–18. ISBN 978-1-00-332737-0 1, 7, 8, 9, 10, 22

[2] H. Abramovich, **"Introduction to composite materials**," in *Stability and Vibrations of Thin Walled Composite Structures*. Woodhead Publishing, 2017, pp. 1–47. ISBN 978-0-08-100410-4 1, 7

[3] H. S. S. Shekar and M. Ramachandra, **"Green Composites: A Review**," *Materials Today: Proceedings*, vol. 5, no. 1, Part 3, pp. 2518–2526, 2018. doi: http://dx.doi.org/10.1016/j.matpr.2017.11.034. 1

[4] V. Rahul, S. Alokita, K. Jayakrishna, V. R. Kar, M. Rajesh, S. Thirumalini, and M. Manikandan, **"Structural health monitoring of aerospace composites**," in *Structural Health Monitoring of Biocomposites, Fibre-Reinforced Composites and Hybrid Composites*, ser. Woodhead Publishing Series in Composites Science and Engineering. Woodhead Publishing, 2019, pp. 33–52. ISBN 978-0-08-102291-7 1, 22

[5] U. S. Government Accountability Office, **"Aviation Safety: Status of FAA's Actions to Oversee the Safety of Composite Airplanes**," 2021. [Online]. Available: https://www.gao.gov/products/gao-11-849 [Accessed: 2023-02-14] 1, 2

[6] **"Aerospace Composites Market, Global Industry Size Forecast**," *MarketsandMarkets*, 2023. [Online]. Available: https://www.marketsandmarkets.com/Market-Reports/aerospace-composites-market-246663558.html [Accessed: 2023-02-15] 2

[7] Victor Giurgiutiu, **"Damage and Failure of Aerospace Composites**," in *Structural Health Monitoring of Aerospace Composites*, 1st ed. Academic Press, 2015, pp. 126–174. ISBN 978-0-12-409605-9 2, 3, 28, 41

[8] D. N. Ball, **"Contributions of CFD to the 787 - and Future Needs**," HLRS High Performance Computing Center: Stuttgart, Germany & The Imperial College: London, United Kingdom, 2008. [Online]. Available: https://www.hpcuserforum.com/presentations/Germany/Boeing%20Ball%20IDC%20pdf.pdf [Accessed: 2023-02-14] 3

[9] Civil Aviation Authority, **"Reliability of Damage Detection in Advanced Composite Aircraft Structures**," 2013. [Online]. Available: https://publicapps.caa.co.uk/modalapplication.aspx?catid=1&pagetype=65&appid=11&mode=detail&id=5407 [Accessed: 2023-02-15] 3

[10] A. Wronkowicz-Katunin, A. Katunin, and K. Dragan, **"Reconstruction of Barely Visible Impact Damage in Composite Structures Based on Non-Destructive Evaluation Results**," *Sensors*, vol. 19, no. 21, p. 4629, 2019. doi: http://dx.doi.org/10.3390/s19214629. 3, 4, 32, 33, 87

[11] H. Zhang, E. Bilotti, and T. Peijs, **"The use of carbon nanotubes for damage sensing and structural health monitoring in laminated composites: A review**," *Nanocomposites*, vol. 1, no. 4, pp. 167–184, 2015. doi: http://dx.doi.org/10.1080/20550324.2015.1113639. 3, 4

[12] G. Wild, L. Pollock, A. K. Abdelwahab, and J. Murray, **"The Need for Aerospace Structural Health Monitoring: A review of aircraft fatigue accidents**," *International Journal of Prognostics and Health Management*, vol. 12, no. 3, 2021. doi: http://dx.doi.org/10.36001/ijphm.2021.v12i3.2368. 3

[13] O. Ahmed, X. Wang, M.-V. Tran, and M.-Z. Ismadi, **"Advancements in fiber-reinforced polymer composite materials damage detection methods: Towards achieving energy-efficient SHM systems**," *Composites Part B: Engineering*, vol. 223, p. 109136, 2021. doi: http://dx.doi.org/10.1016/j.compositesb.2021.109136. 3, 41

[14] H. Rocha, C. Semprimoschnig, and J. P. Nunes, **"Sensors for process and structural health monitoring of aerospace composites: A review**," *Engineering Structures*, vol. 237, p. 112231, Jun. 2021. doi: http://dx.doi.org/10.1016/j.engstruct.2021.112231. 4, 41

[15] P. Hofmann, A. Walch, A. Dinkelmann, S. K. Selvarayan, and G. T. Gresser, **"Woven piezoelectric sensors as part of the textile reinforcement of fiber reinforced plastics**," *Composites Part A: Applied Science and Manufacturing*, vol. 116, pp. 79–86, 2019. doi: http://dx.doi.org/10.1016/j.compositesa.2018.10.019. 4

[16] V. Kostopoulos, A. Masouras, A. Baltopoulos, A. Vavouliotis, G. Sotiriadis, and L. Pambaguian, **"A critical review of nanotechnologies for composite aerospace structures**," *CEAS Space Journal*, vol. 9, no. 1, pp. 35–57, 2017. doi: http://dx.doi.org/10.1007/s12567-016-0123-7. 4

[17] M. Balasubramanian, **"Introduction to Composites**," in *Composite Materials and Processing*, 1st ed. CRC Press, 2013, pp. 1–29. ISBN 978-0-429-06646-7 7

[18] A. Varvani-Farahani, **"Composite Materials: Characterization, Fabrication and Application-Research Challenges and Directions**," *Applied Composite Materials*, vol. 17, no. 2, pp. 63–67, 2010. doi: http://dx.doi.org/10.1007/s10443-009-9107-5. 7

[19] R. R. Nagavally, **"Composite Materials - History, Types, Fabrication Techniques, Advantages, and Applications**," *International Journal of*

Advances in Science Engineering and Technology, vol. 4, no. 3, pp. 87–92, 2016. 8

[20] T.-D. Ngo, **"Introduction to Composite Materials**," in *Composite and Nanocomposite Materials - From Knowledge to Industrial Applications*. IntechOpen, 2020. ISBN 978-1-78985-461-9 8, 12, 13, 16, 17, 19, 20

[21] A. B. Strong, **"Introduction to Composites**," in *Fundamentals of Composites Manufacturing: Materials, Methods and Applications*, 2nd ed. Dearborn, Mich: Society of Manufacturing Engineers, 2008. ISBN 978-0-87263-854-9 8, 14, 20, 21

[22] Victor Giurgiutiu, **"The Future of Composites in Aerospace**," in *Structural Health Monitoring of Aerospace Composites*, 1st ed. Academic Press, 2015, pp. 18–20. ISBN 978-0-12-409605-9 9

[23] S. Singh and S. Singh, **"Intense Classification of Composite Materials**," in *Fabrication and Machining of Advanced Materials and Composites: Opportunities and Challenges*, 1st ed., Subhash Sing and Dinesh Kumar, Eds. Boca Raton: CRC Press, 2022, pp. 19–377. ISBN 978-1-00-332737-0 9, 22

[24] K. K. Chawla, **"Reinforcements**," in *Composite Materials: Science and Engineering*. Springer International Publishing, 2019, pp. 7–74. ISBN 978-3-030-28983-6 11, 15

[25] S. A. Mirdehghan, **"Fibrous polymeric composites**," in *Engineered Polymeric Fibrous Materials*, ser. The Textile Institute Book Series, M. Latifi, Ed. Woodhead Publishing, 2021, pp. 1–58. ISBN 978-0-12-824381-7 11, 12, 13, 14, 15, 16, 17, 18, 43

[26] Marcelo F. S. F. de Moura, Alfredo B. de Morais, and António G. de Magalhães, **"Introdução aos Materiais Compósitos**," in *Materiais Compósitos - Materiais, Fabrico e Comportamento Mecânico*, 2nd ed. Publindústria, 2009. ISBN 978-972-8953-00-3 12, 15, 19, 20

[27] R. Bacon, **"Growth, Structure, and Properties of Graphite Whiskers**," *Journal of Applied Physics*, vol. 31, no. 2, pp. 283–290, Feb. 1960. doi: http://dx.doi.org/10.1063/1.1735559. 13

[28] B. A. Newcomb, **"Processing, structure, and properties of carbon fibers**," *Composites Part A: Applied Science and Manufacturing*, vol. 91, pp. 262–282, 2016. doi: http://dx.doi.org/10.1016/j.compositesa.2016.10.018. 13

[29] **"Carbon Fiber Market**," *Transparency Market Research*, 2022. [Online]. Available: https://www.transparencymarketresearch.com/carbon-fiber-market.html [Accessed: 2023-03-21] 13

[30] TEIJIN, **"Twaron – a versatile high-performance fiber**." [Online]. Available: https://gernitex.com/wp-content/uploads/2017/09/Twaron_DS.pdf [Accessed: 2023-03-29] 15

[31] C. Arvinte, A. V. Sandu, D. D. Burduhos-Nergis, M. A. B. Sava, and C. Bejinariu, **"Technical requirements and materials used in firefighters gloves manufacturing**," *IOP Conference Series: Materials Science and Engineering*, vol. 572, no. 1, p. 012070, 2019. doi: http://dx.doi.org/10.1088/1757-899X/572/1/012070. 15

[32] M. Balasubramanian, **"Dispersed Phase**," in *Composite Materials and Processing*, 1st ed. CRC Press, 2013, pp. 31–96. ISBN 978-0-429-06646-7 16

[33] M. Balasubramanian, **"Matrix Materials**," in *Composite Materials and Processing*, 1st ed. CRC Press, 2013, pp. 97–166. ISBN 978-0-429-06646-7 18, 19, 21

[34] K. K. Chawla, **"Matrix Materials**," in *Composite Materials: Science and Engineering*. Springer International Publishing, 2019, pp. 75–105. ISBN 978-3-030-28983-6 19, 20

[35] M. Balasubramanian, **"Nanocomposites**," in *Composite Materials and Processing*, 1st ed. CRC Press, 2013, pp. 511–593. ISBN 978-0-429-06646-7 22, 23

[36] Jozef Sivek, **"Carbon Allotropes**," *Wikimedia Commons*, 2015. [Online]. Available: https://commons.wikimedia.org/wiki/File:Carbon_allotropes.svg [Accessed: 2023-05-10] 23

[37] J.-V. Lim, S.-T. Bee, L. Tin Sin, C. T. Ratnam, and Z. A. Abdul Hamid, **"A Review on the Synthesis, Properties, and Utilities of Functionalized Carbon Nanoparticles for Polymer Nanocomposites**," *Polymers*, vol. 13, no. 20, p. 3547, 2021. doi: http://dx.doi.org/10.3390/polym13203547. 24, 25, 26

[38] M. Safdari and M. S. Al-Haik, **"A Review on Polymeric Nanocomposites: Effect of Hybridization and Synergy on Electrical Properties**," in *Carbon-Based Polymer Nanocomposites for Environmental and Energy Applications*, A. F. Ismail and P. S. Goh, Eds. Elsevier, 2018, pp. 113–146. ISBN 978-0-12-813574-7 24, 26

[39] P. Cataldi, A. Athanassiou, and I. S. Bayer, **"Graphene Nanoplatelets-Based Advanced Materials and Recent Progress in Sustainable Applications**," *Applied Sciences*, vol. 8, no. 9, p. 1438, 2018. doi: http://dx.doi.org/10.3390/app8091438. 24

[40] R. Aradhana, S. Mohanty, and S. K. Nayak, **"Comparison of mechanical, electrical and thermal properties in graphene oxide and reduced graphene oxide filled epoxy nanocomposite adhesives**," *Polymer*, vol. 141, pp. 109–123, 2018. doi: http://dx.doi.org/10.1016/j.polymer.2018.03.005. 25

[41] H. W. Kroto, J. R. Heath, S. C. O'Brien, R. F. Curl, and R. E. Smalley, **"C60: Buckminsterfullerene**," *Nature*, vol. 318, no. 6042, pp. 162–163, 1985. doi: http://dx.doi.org/10.1038/318162a0. 25

[42] S. Iijima, **"Helical microtubules of graphitic carbon**," *Nature*, vol. 354, no. 6348, pp. 56–58, 1991. doi: http://dx.doi.org/10.1038/354056a0. 25

[43] S. Iijima and T. Ichihashi, **"Single-shell carbon nanotubes of 1-nm diameter**," *Nature*, vol. 363, no. 6430, pp. 603–605, 1993. doi: http://dx.doi.org/10.1038/363603a0. 25

[44] D. S. Bethune, C. H. Kiang, M. S. de Vries, G. Gorman, R. Savoy, J. Vazquez, and R. Beyers, **"Cobalt-catalysed growth of carbon nanotubes with single-atomic-layer walls**," *Nature*, vol. 363, no. 6430, pp. 605–607, 1993. doi: http://dx.doi.org/10.1038/363605a0. 25

[45] J. Li, Z. Zhang, J. Fu, Z. Liang, and K. R. Ramakrishnan, **"Mechanical properties and structural health monitoring performance of carbon nanotube-modified FRP composites: A review**," *Nanotechnology Reviews*, vol. 10, no. 1, pp. 1438–1468, 2021. doi: http://dx.doi.org/10.1515/ntrev-2021-0104. 25, 76, 79

[46] A. Kalamkarov, A. Georgiades, S. Rokkam, V. Veedu, and M. Ghasemi-Nejhad, **"Analytical and numerical techniques to predict carbon nanotubes properties**," *International Journal of Solids and Structures*, vol. 43, no. 22-23, pp. 6832–6854, 2006. doi: http://dx.doi.org/10.1016/j.ijsolstr.2006.02.009. 25, 27

[47] A. Takakura, K. Beppu, T. Nishihara, A. Fukui, T. Kozeki, T. Namazu, Y. Miyauchi, and K. Itami, **"Strength of carbon nanotubes depends on their chemical structures**," *Nature Communications*, vol. 10, no. 1, p. 3040, 2019. doi: http://dx.doi.org/10.1038/s41467-019-10959-7. 25

[48] S. Meguid, X. Xia, and M. Elaskalany, **"Unravelling the sensory capability of MWCNT-reinforced nanocomposites**," *Carbon*, vol. 204, pp. 147–161, 2023. doi: http://dx.doi.org/10.1016/j.carbon.2022.12.037. 25

[49] J. M. Wernik and S. A. Meguid, **"Recent Developments in Multifunctional Nanocomposites Using Carbon Nanotubes**," *Applied Mechanics Reviews*, vol. 63, no. 5, p. 050801, 2010. doi: http://dx.doi.org/10.1115/1.4003503. 26

[50] K. C. Sivaganga and T. Varughese, **"Physical Properties of Carbon Nanotubes**," in *Handbook of Carbon Nanotubes*, J. Abraham, S. Thomas, and N. Kalarikkal, Eds. Cham: Springer International Publishing, 2022, pp. 283–297. ISBN 978-3-030-91346-5 26, 44

[51] S. Liu, V. S. Chevali, Z. Xu, D. Hui, and H. Wang, **"A review of extending performance of epoxy resins using carbon nanomaterials**," *Composites Part B: Engineering*, vol. 136, pp. 197–214, 2018. doi: http://dx.doi.org/10.1016/j.compositesb.2017.08.020. 26

[52] M. Filchakova and V. Saik, **"Multi-walled Carbon Nanotubes Production, Properties & Applications**," *Tuball*, 2021. [Online]. Available: https://tuball.com/articles/multi-walled-carbon-nanotubes [Accessed: 2023-03-01] 27

[53] C. Li, E. T. Thostenson, and T.-W. Chou, **"Sensors and actuators based on carbon nanotubes and their composites: A review**," *Composites Science and Technology*, vol. 68, no. 6, pp. 1227–1249, 2008. doi: http://dx.doi.org/10.1016/j.compscitech.2008.01.006. 27

[54] L. Burtscher, "**Electrical and Mechanical Properties of Carbon Nanotubes**," Ph.D. dissertation, Heriot-Watt University, Edinburgh, Scotland, 2005. [Online]. Available: https://www.researchgate.net/publication/241144604_Electrical_and_mechanical_properties_of_carbon_nanotubes 27

[55] S. Shah, S. Karuppanan, P. Megat-Yusoff, and Z. Sajid, **"Impact resistance and damage tolerance of fiber reinforced composites: A review**," *Composite Structures*, vol. 217, pp. 100–121, 2019. doi: http://dx.doi.org/10.1016/j.compstruct.2019.03.021. 28

[56] D. Kreculj and B. Rasuo, **"Impact damage modeling in laminated composite aircraft structures**," in *Sustainable Composites for Aerospace Applications*, ser. Woodhead Publishing Series in Composites Science and Engineering, M. Jawaid and M. Thariq, Eds. Woodhead Publishing, 2018, pp. 125–153. ISBN 978-0-08-102131-6 28, 30, 32

[57] M. O. W. Richardson and M. J. Wisheart, **"Review of low-velocity impact properties of composite materials**," *Composites Part A: Applied Science and Manufacturing*, vol. 27, no. 12, pp. 1123–1131, 1996. doi: http://dx.doi.org/10.1016/1359-835X(96)00074-7. 28, 33, 34, 87

[58] Jonas A. Zukas, Theodore Nicholas, Hallock F. Swift, Longin B. Greszczuk, and Donald R. Curran, **"Penetration and Perforation of Solids**," in *Impact Dynamics*, 1st ed. John Wiley & Sons, 1982, pp. 155–214. ISBN 978-0-471-08677-2 28

[59] D. Liu and L. E. Malvern, **"Matrix Cracking in Impacted Glass/Epoxy Plates**," *Journal of Composite Materials*, vol. 21, no. 7, pp. 594–609, 1987. doi: http://dx.doi.org/10.1177/002199838702100701. 29, 34

[60] P. O. Sjoblom, J. T. Hartness, and T. M. Cordell, **"On Low-Velocity Impact Testing of Composite Materials**," *Journal of Composite Materials*, vol. 22,

no. 1, pp. 30–52, 1988. doi: http://dx.doi.org/10.1177/002199838802200103. 29, 33

[61] K. N. Shivakumar, W. Elber, and W. Illg, **"Prediction of low-velocity impact damage in thin circular laminates**," *AIAA Journal*, vol. 23, no. 3, pp. 442–449, 1985. doi: http://dx.doi.org/10.2514/3.8933. 29

[62] S. Abrate, **"Impact on Laminated Composite Materials**," *Applied Mechanics Reviews*, vol. 44, no. 4, pp. 155–190, Apr. 1991. doi: http://dx.doi.org/10.1115/1.3119500. 29

[63] W. J. Cantwell and J. Morton, **"The impact resistance of composite materials — a review**," *Composites*, vol. 22, no. 5, pp. 347–362, 1991. doi: http://dx.doi.org/10.1016/0010-4361(91)90549-V. 29

[64] P. Robinson and G. A. O. Davies, **"Impactor mass and specimen geometry effects in low velocity impact of laminated composites**," *International Journal of Impact Engineering*, vol. 12, no. 2, pp. 189–207, 1992. doi: http://dx.doi.org/10.1016/0734-743X(92)90408-L. 29

[65] P. J. Hogg and G. A. Bibo, **"Impact and damage tolerance**," in *Mechanical Testing of Advanced Fibre Composites*, ser. Woodhead Publishing Series in Composites Science and Engineering, J. M. Hodgkinson, Ed. Woodhead Publishing, 2000, pp. 211–247. ISBN 978-1-85573-312-1 29, 30

[66] G. A. O. Davies and R. Olsson, **"Impact on composite structures**," *The Aeronautical Journal*, vol. 108, no. 1089, pp. 541–563, 2004. doi: http://dx.doi.org/10.1017/S0001924000000385. 29, 32, 33, 36, 88

[67] D. Barath, "**Design of a Specimen Fixture for Impact Resistance Testing in an Instron Dynatup 8250 Drop Weight Impact Tester**," Bachelor of Science, California Polytechnic State University, San Luis Obispo, 2013. [Online]. Available: https://digitalcommons.calpoly.edu/aerosp/120 31

[68] Joshua M. Duell, **"Impact Testing of Advanced Composites**," in *Advanced Topics in Characterization of Composites*. Trafford Publishing, 2004. ISBN 1-4120-3639-9 31, 32

[69] N. Takeda, R. L. Sierakowski, and L. E. Malvern, **"Microscopic Observations of Cross Sections of Impacted Composite Laminates**," *Composites Technology and Research*, vol. 4, no. 2, pp. 40–44, 1982. doi: http://dx.doi.org/10.1520/CTR10762J. 33

[70] D. Liu, **"Impact-Induced Delamination—A View of Bending Stiffness Mismatching**," *Journal of Composite Materials*, vol. 22, no. 7, pp. 674–692, Jul. 1988. doi: http://dx.doi.org/10.1177/002199838802200706. 33, 38, 88

[71] H. Y. Choi, R. J. Downs, and F.-K. Chang, **"A New Approach toward Understanding Damage Mechanisms and Mechanics of Laminated Composites Due to Low-Velocity Impact: Part I—Experiments**," *Journal of Composite Materials*, vol. 25, no. 8, pp. 992–1011, 1991. doi: http://dx.doi.org/10.1177/002199839102500803. 34

[72] G. A. O. Davies and P. Robinson, **"Predicting failure by debonding/delamination**," in *AGARD: 74th Structures and Materials Meeting*, Greece, 1992. [Online]. Available: https://www.sto.nato.int/publications/AGARD/AGARD-CP-530/AGARD-CP-530.pdf 34

[73] R. Olsson, **"Low- and medium-velocity impact as a cause of failure in polymer matrix composites**," in *Failure Mechanisms in Polymer Matrix Composites*, ser. Woodhead Publishing Series in Composites Science and Engineering, P. Robinson, E. Greenhalgh, and S. Pinho, Eds. Woodhead Publishing, 2012, pp. 53–78. ISBN 978-1-84569-750-1 34, 35, 36, 88

[74] Y. P. Siow and V. P. W. Shim, **"An Experimental Study of Low Velocity Impact Damage in Woven Fiber Composites**," *Journal of Composite Materials*, vol. 32, no. 12, pp. 1178–1202, 1998. doi: http://dx.doi.org/10.1177/002199839803201203. 34, 37, 88

[75] C. Wang, Z. Chen, V. V. Silberschmidt, and A. Roy, **"Damage accumulation in braided textiles-reinforced composites under repeated impacts : Experimental and numerical studies**," 2018. doi: http://dx.doi.org/10.1016/j.compstruct.2018.07.084. 34

[76] R. Olsson, **"Mass criterion for wave controlled impact response of composite plates**," *Composites Part A: Applied Science and Manufacturing*, vol. 31, no. 8, pp. 879–887, Aug. 2000. doi: http://dx.doi.org/10.1016/S1359-835X(00)00020-8. 35

[77] T. Mitrevski, I. H. Marshall, R. Thomson, R. Jones, and B. O. Whittingham, **"The effect of impactor shape on the impact response of composite laminates**," *Composite Structures*, vol. 67, no. 2, pp. 139–148, 2005. doi: http://dx.doi.org/10.1016/j.compstruct.2004.09.007. 37

[78] M. M. M. Naglis and J. R. M. d'Almeida, **"Avaliação dos modos de falha sob impacto de compósitos de matriz polimérica reforçados por fibras**," *Polímeros*, vol. 8, pp. 54–60, 1998. doi: http://dx.doi.org/10.1590/S0104-14281998000100008. 38

[79] B. Vieille, V. M. Casado, and C. Bouvet, **"About the impact behavior of woven-ply carbon fiber-reinforced thermoplastic- and thermosetting-composites: A comparative study**," *Composite Structures*, vol. 101, pp. 9–21, 2013. doi: http://dx.doi.org/10.1016/j.compstruct.2013.01.025. 38

[80] V. Kostopoulos, A. Baltopoulos, P. Karapappas, A. Vavouliotis, and A. Paipetis, **"Impact and after-impact properties of carbon fibre reinforced composites enhanced with multi-wall carbon nanotubes**," *Composites Science and Technology*, vol. 70, no. 4, pp. 553–563, 2010. doi: http://dx.doi.org/10.1016/j.compscitech.2009.11.023. 39, 82

[81] P. Wang, X. Zhang, G. Lim, H. Neo, A. A. Malcolm, Y. Xiang, G. Lu, and J. Yang, **"Improvement of impact-resistant property of glass fiber-reinforced composites by carbon nanotube-modified epoxy and pre-stretched fiber fabrics**," *Journal of Materials Science*, vol. 50, no. 18, pp. 5978–5992, 2015. doi: http://dx.doi.org/10.1007/s10853-015-9145-3. 39, 82

[82] B. Ashrafi, J. Guan, V. Mirjalili, Y. Zhang, L. Chun, P. Hubert, B. Simard, C. T. Kingston, O. Bourne, and A. Johnston, **"Enhancement of mechanical performance of epoxy/carbon fiber laminate composites using single-walled carbon nanotubes**," *Composites Science and Technology*, vol. 71, no. 13, pp. 1569–1578, Sep. 2011. doi: http://dx.doi.org/10.1016/j.compscitech.2011.06.015. 39

[83] G. Caprino, **"Influence of material thickness on the response of carbon-fabric/epoxy panels to low velocity impact**," *Composites Science and Technology*, vol. 59, no. 15, pp. 2279–2286, 1999. doi: http://dx.doi.org/10.1016/S0266-3538(99)00079-2. 39

[84] J. Zhou, B. Liu, and S. Wang, **"Finite element analysis on impact response and damage mechanism of composite laminates under single and repeated low-velocity impact**," *Aerospace Science and Technology*, vol. 129, p. 107810, 2022. doi: http://dx.doi.org/10.1016/j.ast.2022.107810. 40, 88

[85] A. M. Amaro, P. N. Reis, and M. F. De Moura, **"Residual Strength after Low Velocity Impact in Carbon-Epoxy Laminates**," *Materials Science Forum*, vol. 514–516, pp. 624–628, 2006. doi: http://dx.doi.org/10.4028/www.scientific.net/MSF.514-516.624. 40

[86] E. Sevkat, B. Liaw, F. Delale, and B. B. Raju, **"Effect of repeated impacts on the response of plain-woven hybrid composites**," *Composites Part B: Engineering*, vol. 41, no. 5, pp. 403–413, 2010. doi: http://dx.doi.org/10.1016/j.compositesb.2010.01.001. 40

[87] B. Fiedler, F. Gojny, M. Wichmann, W. Bauhofer, and K. Schulte, **"Can carbon nanotubes be used to sense damage in composites?**" *Annales de Chimie: Science des Materiaux*, vol. 29, no. 6, pp. 81–94, 2004. doi: http://dx.doi.org/10.3166/acsm.29.6.81-94. 41

[88] F. Avilés, A. I. Oliva-Avilés, and M. Cen-Puc, **"Piezoresistivity, Strain, and Damage Self-Sensing of Polymer Composites Filled with Carbon Nanos-**

tructures," *Advanced Engineering Materials*, vol. 20, no. 7, p. 1701159, 2018. doi: http://dx.doi.org/10.1002/adem.201701159. 42, 43, 44, 45, 46, 47, 90

[89] A. Lemartinel, M. Castro, O. Fouché, J.-C. De-Luca, and J.-F. Feller, **"A Review of Nanocarbon-Based Solutions for the Structural Health Monitoring of Composite Parts Used in Renewable Energies**," *Journal of Composites Science*, vol. 6, no. 2, p. 32, 2022. doi: http://dx.doi.org/10.3390/jcs6020032. 42, 44, 47

[90] J. K. W. Sandler, J. E. Kirk, I. A. Kinloch, M. S. P. Shaffer, and A. H. Windle, **"Ultra-low electrical percolation threshold in carbon-nanotube-epoxy composites**," *Polymer*, vol. 44, no. 19, pp. 5893–5899, 2003. doi: http://dx.doi.org/10.1016/S0032-3861(03)00539-1. 42

[91] D. Zhao, Q. Lei, C. Qin, and X. Bai, **"Melt process and performance of multi-walled carbon nanotubes reinforced LDPE composites**," *Pigment & Resin Technology*, vol. 35, no. 6, pp. 341–345, 2006. doi: http://dx.doi.org/10.1108/03699420610711344. 42

[92] W. Bauhofer and J. Z. Kovacs, **"A review and analysis of electrical percolation in carbon nanotube polymer composites**," *Composites Science and Technology*, vol. 69, no. 10, pp. 1486–1498, 2009. doi: http://dx.doi.org/10.1016/j.compscitech.2008.06.018. 43

[93] F. H. Gojny, M. H. G. Wichmann, B. Fiedler, I. A. Kinloch, W. Bauhofer, A. H. Windle, and K. Schulte, **"Evaluation and identification of electrical and thermal conduction mechanisms in carbon nanotube/epoxy composites**," *Polymer*, vol. 47, no. 6, pp. 2036–2045, 2006. doi: http://dx.doi.org/10.1016/j.polymer.2006.01.029. 43

[94] J. B. Bai and A. Allaoui, **"Effect of the length and the aggregate size of MWNTs on the improvement efficiency of the mechanical and electrical properties of nanocomposites—experimental investigation**," *Composites Part A: Applied Science and Manufacturing*, vol. 34, no. 8, pp. 689–694, 2003. doi: http://dx.doi.org/10.1016/S1359-835X(03)00140-4. 43

[95] C. Stampfer, A. Jungen, R. Linderman, D. Obergfell, S. Roth, and C. Hierold, **"Nano-electromechanical displacement sensing based on single-walled carbon nanotubes**," *Nano Letters*, vol. 6, no. 7, pp. 1449–1453, 2006. doi: http://dx.doi.org/10.1021/nl0606527. 44

[96] A. I. Oliva-Avilés, F. Avilés, G. D. Seidel, and V. Sosa, **"On the contribution of carbon nanotube deformation to piezoresistivity of carbon nanotube/polymer composites**," *Composites Part B: Engineering*, vol. 47, pp. 200–206, 2013. doi: http://dx.doi.org/10.1016/j.compositesb.2012.09.091. 44

[97] W. Zhang, J. Suhr, and N. Koratkar, **"Carbon Nanotube/Polycarbonate Composites as Multifunctional Strain Sensors**," *Journal of Nanoscience and Nanotechnology*, vol. 6, no. 4, pp. 960–964, 2006. doi: http://dx.doi.org/10.1166/jnn.2006.171. 44

[98] M. H. G. Wichmann, S. T. Buschhorn, J. Gehrmann, and K. Schulte, **"Piezoresistive response of epoxy composites with carbon nanoparticles under tensile load**," *Physical Review B*, vol. 80, no. 24, p. 245437, 2009. doi: http://dx.doi.org/10.1103/PhysRevB.80.245437. 44, 45

[99] G. Yin, N. Hu, Y. Karube, Y. Liu, Y. Li, and H. Fukunaga, **"A carbon nanotube/polymer strain sensor with linear and anti-symmetric piezoresistivity**," *Journal of Composite Materials*, vol. 45, no. 12, pp. 1315–1323, 2011. doi: http://dx.doi.org/10.1177/0021998310393296. 44

[100] L. Vertuccio, L. Guadagno, G. Spinelli, P. Lamberti, V. Tucci, and S. Russo, **"Piezoresistive properties of resin reinforced with carbon nanotubes for health-monitoring of aircraft primary structures**," *Composites Part B: Engineering*, vol. 107, pp. 192–202, 2016. doi: http://dx.doi.org/10.1016/j.compositesb.2016.09.061. 44, 91

[101] T. Khan, M. Irfan, M. Ali, Y. Dong, S. Ramakrishna, and R. Umer, **"Insights to low electrical percolation thresholds of carbon-based polypropylene nanocomposites**," *Carbon*, vol. 176, pp. 602–631, 2021. doi: http://dx.doi.org/10.1016/j.carbon.2021.01.158. 46

[102] M. Haghgoo, R. Ansari, and M. K. Hassanzadeh-Aghdam, **"Synergic effect of graphene nanoplatelets and carbon nanotubes on the electrical resistivity and percolation threshold of polymer hybrid nanocomposites**," *The European Physical Journal Plus*, vol. 136, no. 7, p. 768, 2021. doi: http://dx.doi.org/10.1140/epjp/s13360-021-01774-5. 46

[103] E. T. Thostenson and T.-W. Chou, **"Real-time *in situ* sensing of damage evolution in advanced fiber composites using carbon nanotube networks**," *Nanotechnology*, vol. 19, no. 21, p. 215713, 2008. doi: http://dx.doi.org/10.1088/0957-4484/19/21/215713. 48, 49, 56

[104] V. Kostopoulos, A. Vavouliotis, P. Karapappas, P. Tsotra, and A. Paipetis, **"Damage Monitoring of Carbon Fiber Reinforced Laminates Using Resistance Measurements. Improving Sensitivity Using Carbon Nanotube Doped Epoxy Matrix System**," *Journal of Intelligent Material Systems and Structures*, vol. 20, no. 9, pp. 1025–1034, 2009. doi: http://dx.doi.org/10.1177/1045389X08099993. 49, 56

[105] M. Monti, M. Natali, R. Petrucci, J. M. Kenny, and L. Torre, **"Impact damage sensing in glass fiber reinforced composites based on carbon nan-**

otubes by electrical resistance measurements," *Journal of Applied Polymer Science*, vol. 122, no. 4, pp. 2829–2836, 2011. doi: http://dx.doi.org/10.1002/app.34412. 50, 56, 70, 89

[106] L. Gao, T.-W. Chou, E. T. Thostenson, Z. Zhang, and M. Coulaud, **"In situ sensing of impact damage in epoxy/glass fiber composites using percolating carbon nanotube networks**," *Carbon*, vol. 49, no. 10, pp. 3382–3385, 2011. doi: http://dx.doi.org/10.1016/j.carbon.2011.04.003. 51, 56, 70, 100

[107] S. Grammatikos and A. Paipetis, **"On the electrical properties of multi scale reinforced composites for damage accumulation monitoring**," *Composites Part B: Engineering*, vol. 43, no. 6, pp. 2687–2696, 2012. doi: http://dx.doi.org/10.1016/j.compositesb.2012.01.077. 52, 56, 61

[108] L. Arronche, V. La Saponara, S. Yesil, and G. Bayram, **"Impact damage sensing of multiscale composites through epoxy matrix containing carbon nanotubes**," *Journal of Applied Polymer Science*, vol. 128, no. 5, pp. 2797–2806, 2013. doi: http://dx.doi.org/10.1002/app.38448. 53, 56, 89

[109] M. Al-Bahrani and A. Cree, **"A simple criterion to evaluate the degree of damage in composite materials after sudden impact loads by exploiting the MWCNTs piezoresistive property**," *Carbon*, vol. 150, pp. 505–517, 2019. doi: http://dx.doi.org/10.1016/j.carbon.2019.05.053. 53, 54, 55, 56, 61, 70, 76, 77, 78, 89, 100

[110] Rebelco, **"Tecidos Técnicos de Vidro 1195P**." [Online]. Available: http://rebelco.pt/tecidosV.html [Accessed: 2023-04-27] 57

[111] Sicomin, **"SR 8100 / SD 882X Infusion System**," 2019. [Online]. Available: https://sicomin.com/datasheets/product-pdf94.pdf [Accessed: 2023-04-27] 57

[112] Nanocyl, **"NC7000™ - Technical Data Sheet**," 2020. [Online]. Available: https://www.nanocyl.com/download/tds-nc7000/ [Accessed: 2023-05-01] 58

[113] MG Chemicals, **"842AR - Super Shield Silver Conductive Paint**," 2021. [Online]. Available: https://mgchemicals.com/products/conductive-paint/conductive-acrylic-paints/silver-conductive-paint/ [Accessed: 2023-05-01] 58

[114] P. Santos, A. Maceiras, and P. N. B. Reis, **"Influence of manufacturing parameters on the mechanical properties of nano-reinforced CFRP by carbon nanofibers**," *IOP Conference Series: Materials Science and Engineering*, vol. 1126, no. 1, p. 012012, 2021. doi: http://dx.doi.org/10.1088/1757-899X/1126/1/012012. 59

[115] X. F. Sánchez-Romate, A. Jiménez-Suárez, M. Campo, A. Ureña, and S. G. Prolongo, **"Electrical Properties and Strain Sensing Mechanisms in Hy-**

brid Graphene Nanoplatelet/Carbon Nanotube Nanocomposites," *Sensors*, vol. 21, no. 16, p. 5530, 2021. doi: http://dx.doi.org/10.3390/s21165530. 62

[116] I. Khalid, **"A Brief Study of Methods to Determine the Electrical Resistivity of Materials**," *Indonesian Journal of Applied Physics*, vol. 13, no. 1, pp. 53–59, 2023. doi: http://dx.doi.org/10.13057/ijap.v13i1.64742. 64

[117] **"Standard Test Methods for Flexural Properties of Unreinforced and Reinforced Plastics and Electrical Insulating Materials**," *ASTM International*, 2017. doi: http://dx.doi.org/10.1520/D0790-17. 66, 67

[118] William D. Callister Jr. and David G. Rethwisch, **"Composites**," in *Materials Science and Engineering: An Introduction*, 10th ed. Wiley, 2018, pp. 567–606. ISBN 978-1-119-40549-8 67, 76

[119] **"Standard Test Method for Measuring the Damage Resistance of a Fiber-Reinforced Polymer Matrix Composite to a Drop-Weight Impact Event**," *ASTM International*, 2015. doi: http://dx.doi.org/10.1520/D7136_D7136M-15. 69

[120] M. M. Ghorbani and R. Taherian, **"Methods of Measuring Electrical Properties of Material**," in *Electrical Conductivity in Polymer-Based Composites*, ser. Plastics Design Library, R. Taherian and A. Kausar, Eds. William Andrew Publishing, 2019, pp. 365–394. ISBN 978-0-12-812541-0 70, 71

[121] K. K. Singh, S. K. Chaudhary, and R. Venugopal, **"Enhancement of flexural strength of glass fiber reinforced polymer laminates using multiwall carbon nanotubes**," *Polymer Engineering & Science*, vol. 59, no. S1, pp. E248–E261, 2019. doi: http://dx.doi.org/10.1002/pen.24929. 76

[122] S. Chaudhary, K. Singh, and R. Venugopal, **"Experimental and numerical analysis of flexural test of unfilled glass fiber reinforced polymer composite laminate**," *Materials Today: Proceedings*, vol. 5, no. 1, pp. 184–192, 2018. doi: http://dx.doi.org/10.1016/j.matpr.2017.11.070. 76

[123] F. Pashmforoush, M. Fotouhi, and M. Ahmadi, **"Damage Characterization of Glass/Epoxy Composite Under Three-Point Bending Test Using Acoustic Emission Technique**," *Journal of Materials Engineering and Performance*, vol. 21, no. 7, pp. 1380–1390, 2012. doi: http://dx.doi.org/10.1007/s11665-011-0013-2. 76

[124] G. Strugala, M. Landowski, M. Zaremba, J. Turowski, and M. Szkodo, **"Impact Resistance of Plain and Twill Fabric in GFRP Measured by Active Thermography**," *Advanced Composites Letters*, vol. 27, no. 5, p. 096369351802700501, 2018. doi: http://dx.doi.org/10.1177/096369351802700501. 78

[125] Z. Y. Zhang and M. O. W. Richardson, **"Low velocity impact induced damage evaluation and its effect on the residual flexural properties of pultruded GRP composites**," *Composite Structures*, vol. 81, no. 2, pp. 195–201, 2007. doi: http://dx.doi.org/10.1016/j.compstruct.2006.08.019. 78

[126] G. A. Schoeppner and S. Abrate, **"Delamination threshold loads for low velocity impact on composite laminates**," *Composites Part A: Applied Science and Manufacturing*, vol. 31, no. 9, pp. 903–915, 2000. doi: http://dx.doi.org/10.1016/S1359-835X(00)00061-0. 82

[127] Y. Yilmaz, F. Ozgul, and I. Agir, **"An experimental study on low velocity impact characteristics of glass fiber reinforced epoxy nanocomposites**," *Sādhanā*, vol. 48, no. 1, p. 29, 2023. doi: http://dx.doi.org/10.1007/s12046-023-02090-7. 83

[128] E. M. Soliman, M. P. Sheyka, and M. R. Taha, **"Low-velocity impact of thin woven carbon fabric composites incorporating multi-walled carbon nanotubes**," *International Journal of Impact Engineering*, vol. 47, pp. 39–47, 2012. doi: http://dx.doi.org/10.1016/j.ijimpeng.2012.03.002. 84

[129] S. Luo, W. Obitayo, and T. Liu, **"SWCNT-thin-film-enabled fiber sensors for lifelong structural health monitoring of polymeric composites - From manufacturing to utilization to failure**," *Carbon*, vol. 76, pp. 321–329, 2014. doi: http://dx.doi.org/10.1016/j.carbon.2014.04.083. 91

[130] J. A. Rodríguez-González, C. Rubio-González, and J. A. Soto-Cajiga, **"Piezoresistive Response of Spray-coated Multiwalled Carbon Nanotube/Glass Fiber/Epoxy Composites under Flexural Loading**," *Fibers and Polymers*, vol. 20, no. 8, pp. 1673–1683, 2019. doi: http://dx.doi.org/10.1007/s12221-019-8711-8. 91

[131] E. T. Thostenson and T.-W. Chou, **"Carbon Nanotube Networks: Sensing of Distributed Strain and Damage for Life Prediction and Self Healing**," *Advanced Materials*, vol. 18, no. 21, pp. 2837–2841, 2006. doi: http://dx.doi.org/10.1002/adma.200600977. 92

[132] Inês Catarina Ferreira Lima, "**Desenvolvimento de materiais funcionais para estruturas compósitas avançadas**," Ph.D. dissertation, Faculdade de Engenharia da Universidade do Porto, 2020. [Online]. Available: https://repositorio-aberto.up.pt/handle/10216/132827 [Accessed: 2023-10-11] 98